Monte-Carlo Simulation of Light Propagation in Turbid Media

Frits. F.M. de Mul

Version 6
May 2022

Frits de Mul was previously
Assoc.Prof. Biomedical Optics at
Physics Department,
University of Twente,
Enschede, the Netherlands.

Abstract.

The physics behind the simulation program developed in our group is explained. The various options for light transport and scattering, reflection and refraction at boundaries, light sources and detection, and output are described. In addition, some special features, like Laser Doppler velocimetry, Photoacoustics and Frequency-modulation scattering, are described.

Contents.

Previous versions of this report were published in:

- De Mul, F.F.M.; Monte-Carlo simulation of Light transport in Turbid Media, Chapter 12 in: Handbook of Coherent Domain Optical Methods, Biomedical Diagnostics, Environment and Material Science, Tuchin, Valery V. (Ed.), 2004, XLII, 1004 p. (2-volume-set), Kluwer Publishers, Hardcover ISBN: 1-4020-7576-6, pages 465-533.
- De Mul, F.F.M.; Monte-Carlo simulation of Light transport in Turbid Media, Chapter 15 in: Handbook of Coherent Domain Optical Methods, Biomedical Diagnostics, Environment and Material Science, Tuchin, Valery V. (Ed.), 2013, Springer Publishers, Hardcover ISBN: 978-1-4614-5176-1, pages 593-661.

1. Introduction.

In the past decades, much effort has been devoted to the elucidation of the optical properties of turbid media, especially tissue, from human and animal origin. This is worthwhile since these properties can reveal data and conclusions about the physiological condition of the tissue. These optical properties are the scattering and absorption characteristics, both as a function of position in the tissue and as a function of time, *e.g.* after administration of drugs, hydrogenation or temperature treatment. In addition, the spectroscopic response of the tissue (*e.g.* Raman-spectroscopy, induced or auto-fluorescence, absorption spectroscopy) can be of interest to obtain useful information.

Typical experiments to extract values for the optical properties of tissue are: measuring the response of the tissue upon a stimulus from the outside. In the optical case, this mostly corresponds with measuring the properties of light (*e.g.* intensity) or of another suitable variable (*e.g.* sound, with photoacoustics) that will emerge from the tissue, as a function of the distance from the point of entrance of the light, or will pass through the tissue and eventually will appear at the backside of the sample.

In the case of "light in – light out" several interesting methods have been developed in addition to simple intensity measurements. Among those are "Frequency-Modulation" of the light, enabling to measure the phase delay upon passage through the sample, or "Optical Coherence Tomography", where single-scattered light is detected interferometrically.

In order to extract the optical properties from the measured data, it is necessary to have suitable analytical models relating those properties with general ideas about the physics of the light transport in tissue. The best models for this purpose rely on the Radiative Transfer Equation (RTE; also known from disciplines as Neutron Physics) and the Diffusion Approximation (DA) derived from it [1,2,3]. The RTE describes the light transport in turbid media in the form of an integro-differential equation of the (place-time-dependent) radiance, arising from well-defined sources and subject to scattering and absorption. The DA takes into account that in tissue most scattering is predominantly in forward direction. Then the light fluence is divided into two contributions: an isotropic term and a term describing the forward contribution. Several authors [4-10] have published sophisticated models for two- and even three-layered samples. For inhomogeneous samples, the models soon become very complex and difficult to apply, and the number of variables to be used in fitting to the experimental data will soon grow beyond manageability.

Therefore, it turns out to be very difficult to produce tractable analytical models of the transport of light in those media, necessary to extract values for the optical properties from experimental data, especially when those media are more complex than homogeneous semi-infinite layers. This is the case with two- or three layered samples, or when deviant structures, like vessels or plates, are present in those layers. Especially in those cases, Monte-Carlo simulations of the light transport will be of help.

In Monte-Carlo simulations, a completely different approach is followed. The light transport in tissue is described in the form of separate photons travelling through the sample. On its way, the photon might be scattered at (or in) particles, by which the direction of the photon is changed, or the photon is absorbed. The scattering phenomenon will be determined by suitable angle-dependent scattering functions. When a boundary between two layers, or between the sample and the surrounding medium, or between an internal structure and the surrounding layer, is encountered, the photon might be reflected or refracted. This is determined by the well-known Fresnel relations. In between these events, the photon will propagate, and the optical mean free path in that part of the sample will determine the length of the

propagation path. The actual length of the contributions to the path, the angles of scattering, the choice between scattering and absorption, and between reflection and refraction, are determined by random number-based decisions.

Some extra features can be applied to the photons. For instance, photons can be thought of as scattering at particles at rest or at moving particles. This effect will cause a Doppler shift in the frequency of the photons, which can be registered. Afterwards from the Doppler shift distribution of all suitably detected photons the Frequency Power distribution can be derived. Several models are present for this velocity shift: unidirectional or random flow, various flow profiles and so on. Another option is to use as the light source not a beam impinging from the outside world, but a photon absorption distribution inside the sample. In this way, fluorescence or Raman scattering can be mimicked.
When recording the path of the photons through the sample, one might deduce the path length distribution, and from that the time-of-flight distribution. The latter can be used to predict the distributions of phase delays and modulation depths encountered when performing frequency-modulation experiments.
Further, the distribution of positions where photons were absorbed can be used as the distribution of sources for calculating the photoacoustic response, to be detected using suitable detector elements (or groups of elements, to take interference effects into account) at the surface of the sample.

With these applications in mind, we developed [11,12] our Monte-Carlo light simulation package.

2. General outline of the program.

We decided to build the package in a modular and self-explaining form, in the sense that all necessary input to run the simulations can be produced within the program itself. In addition, the output – in the form of parameter plots and other visualisations – can be obtained using the same program.

In overview, the program package consists of following parts:

- Calculation of angle-dependent scattering functions for all types of particles;
- Definition of the light source, either a pencil beam or a broad divergent beam or an internal source;
- The sample system, consisting or one or more layers with different contents, with different optical characteristics and velocity profiles; The contents may consist of "objects": (arrays of) cylinders, spheres, cones, rectangular blocks, and mirrors. See Fig .1.
- Definition of the detection system, consisting of a poly-element detection window, and of its numerical aperture;
- Definition of the calculation mode: *e.g.* reflection or transmission, or absorption, or a combination of those.
- The simulation part, in which a preset amount of photons is injected in the sample and followed along their paths, until either detection or absorption;
- The analysing part, in which parameter plots can be produced and statistics can be calculated.
- Extra features, like Laser Doppler flowmetry, Photoacoustics and Frequency modulation.

These parts will be detailed in following sections.

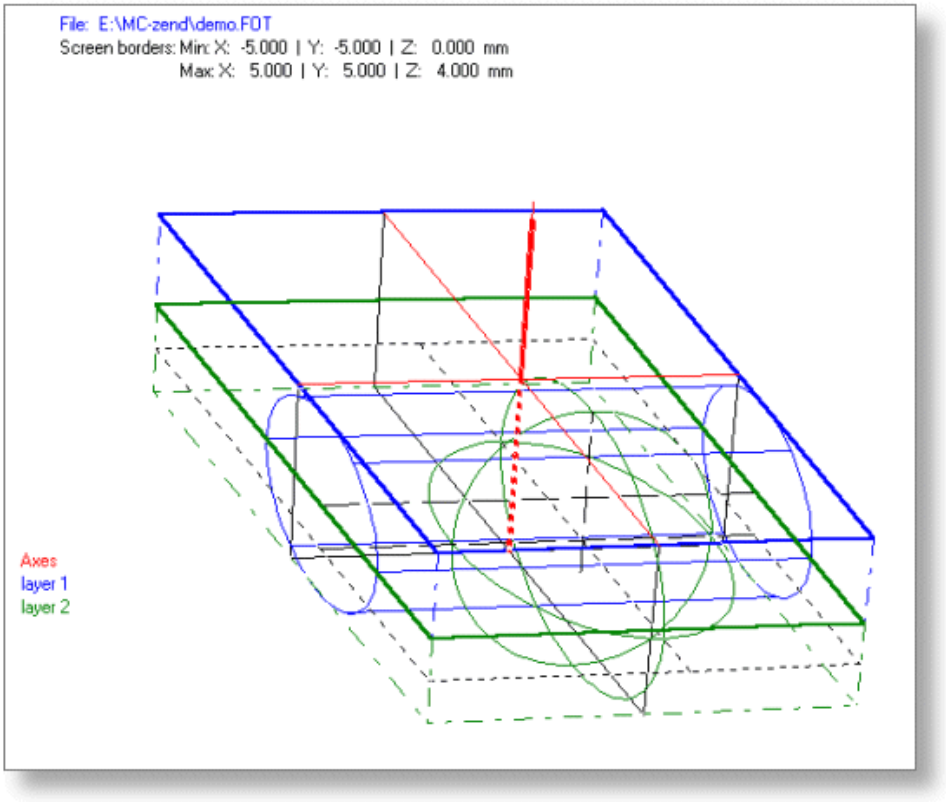

Fig. 1. Structure plot of a two-layer system with a horizontal cylindrical tube and a sphere (see section 2), filled with various concentrations of scattering/absorbing particles. Laser light (here diverging beam) injected around Z-axis..

3. Transport Algorithms.

In order to describe the transport of photons through the sample, one needs algorithms for the various events that the photon may encounter. Those are: scattering or absorption, reflection or refraction at boundaries, and detection. In addition, a mechanism accounting for the destruction of irrelevant photons (*e.g.* photons that have travelled extremely far from the detection window) should be available.

We start with defining the basic optical properties relevant for this problem:

- σ_{sv} : scattering cross section [μm^2] of particle type v ;
- σ_{av} : absorption cross section [μm^2] of particle type v ;
- σ_{tv} : total cross section = $\sigma_{sv} + \sigma_{av}$ [μm^2] of particle type v ;
- a_v : albedo (= $\sigma_{sv} / \sigma_{tv}$) of particle type v ;
- c_{lv} : concentration [particles/mm^{-3}] of particle type v in layer l (or "object" l);
- μ_{sl} : scattering coefficient [mm^{-1}] of layer l (or "object" l) ;
- μ_{al} : absorption coefficient [mm^{-1}] of layer l (or "object" l) ;

All internal structures in a layer (vessels, tubes, blocks, mirrors, spheres, cones…) will further be denoted as "objects".

So the probability f_{lv} to find a particle of type v in layer (or object) l is

$$f_{lv} = \frac{c_{lv}\sigma_{tv}}{\sum_{v} c_{lv}\sigma_{tv}} . \qquad (3.1)$$

There are two basic algorithms for handling non-zero absorption in layers or particles. Frequently the probability of absorption (given by $1 - a_v$) is taken into account as a "weight factor" for the photon. The cumulative effect of applying these subsequent factors at each scattering event will reduce its overall weight in calculating averages of relevant variables (such as intensity) over a set of emerged photons. An example is the work of Wang and Jacques [13]. An advantage is that no photons will be lost by absorption, which can be of importance when the absorption is relatively strong.
Another algorithm does not make use of weight factors, but applies a "sudden death"-method: the photon is considered to be completely absorbed at once, and will thus be removed from the calculation process. This method might be a bit more time consuming, especially when absorption is not very low in a relative sense, but it offers the advantage to study the positions where the photons actually are absorbed. In this way extra features like photoacoustics or fluorescence response can be studied.
In view of this option, we have chosen for the second method.
The general laboratory coordinate system is chosen as shown in Fig. 2.

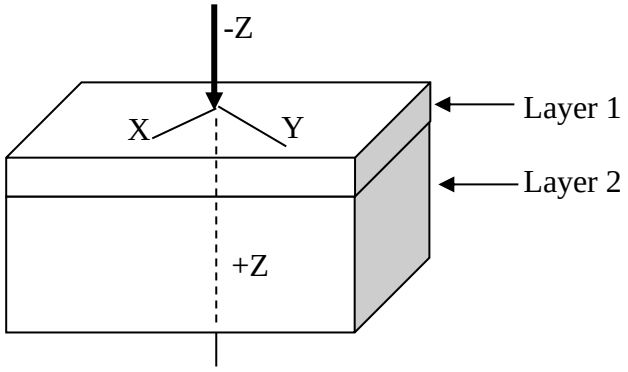

Fig. 2. The laboratory coordinate system. The +Z-axis is chosen as pointing inward. The arrow indicates the default direction of a pencil laser beam.

3.1. Propagation.

Here we will describe the algorithm used for propagation. Also the correction to be made upon crossing an interface (between different layers, or between a layer and a "object", or between a layer or object and the outside world) will be handled.

We may write down the average translation distance for a photon in a layer or object l with scattering particles of varying type, in the case of no absorption by that layer or object itself, as

$$L_l = \frac{1}{\sum_v c_{lv}\sigma_{tv}} \ . \tag{3.2}$$

From this we deduce the expression for calculating the actual path length Δp:

$$\Delta p = -L_l . \ln(1-R) , \tag{3.3}$$

where R is a random number ($0 \le R < 1$) and we have used for the probability f_{sl} to arrive at a path length Δp:

$$f_{sl} = 1 - \exp(-\Delta p / L_l) \ . \tag{3.4}$$

The expression with ln (1-R) is chosen to avoid the singularity in case R should equal 0. However, this path might end prematurely when an boundary at an interface is met. In this case we can geometrically calculate a path fraction f_p , using the distance between the previous event point and the intersection point of the path with the interface, and define the "effective path" Δp_{eff} , by

$$\Delta p_{eff} = f_p . \Delta p . \tag{3.5}$$

In case $f_p < 1$, the path will partially stretch out into the medium at the other side of the interface. When dealing with this part of the path, it should be kept in mind that it has to be corrected in length according to the mean free path for the photons in the two media. See below for a full account.

Now we can define the probability f_{al} for absorption by the medium l (layer or object) before the photon has reached the end of path Δp_{eff}:

$$f_{al} = 1 - \exp(-\mu_{al} . \Delta p_{eff}) . \tag{3.6}$$

This probability will lie between 0 and 1. Now we choose a fresh random number R. There are two possibilities:

- If this R is smaller than f_{al} , then absorption has occurred during path Δp_{eff} .
- It this is not the case, then absorption will occur within the particle at the end of path Δp_{eff} when
  $R < 1 - a_{vl}$, (3.7)
  where R again is a fresh random number. If eq.(3.7) is not fulfilled, then the photon will be scattered.

Since we handle the absorption by the particles in the medium as taking place within the particles themselves, and the absorption by the medium itself separately, we can define the "average translation length" $L_{trans,l}$ for medium l :

$$L_{transl} = \left[\mu_{al} + \sum_{v} c_{lv}\sigma_{sv} \right]^{-1} \quad , \tag{3.8}$$

and the "average absorption length" $L_{abs,l}$ caused by the medium and the scatterers in that medium:

$$L_{abs,l} = \left[\mu_{al} + \sum_{v} c_{lv}\sigma_{av} \right]^{-1} \quad . \tag{3.9}$$

Now we can correct eq. (3.3) and subsequent expressions for absorption, and find for the path with length Δp:

$$\Delta p = -L_{transl}.\ln(1-R) \tag{3.10}$$

In a previous paper [14] we discussed two equivalent algorithms to determine the remaining path length after crossing an interface.
In Fig.3 we present a view of a running simulation in a sample with two layers and two "objects".

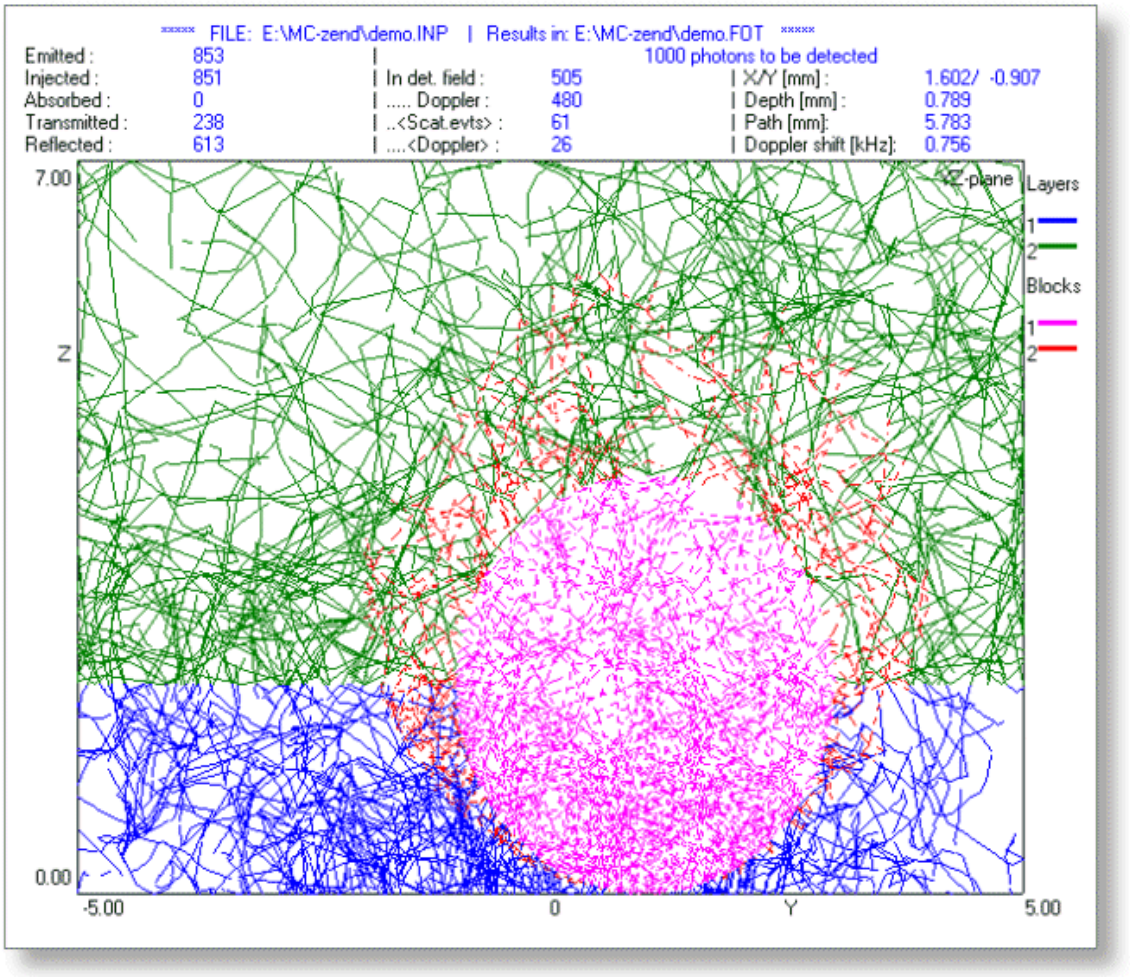

Fig. 3. Running graphics of the simulation process of the structure of fig.1.
View in YZ-plane. Photons entering around pos (0,0,0). The tube (X-direction) and sphere can be seen.

3.2. Scattering.

In case the photon is not absorbed during or at the end of a translation step, the photon will be scattered. We define the angle θ as the polar angle of scattering, with the direction of the previous translation step as the Z-axis of the local coordinate system. For natural (unpolarized) light, the X-axis can be chosen at random in the plane perpendicular to the Z-axis (see Fig.4). For polarized light, the directions of the X- and Y-axes are determined by the polarization state of the incoming photon.

The probability of scattering to the direction given by the angles θ and φ is described by the *scattering function p(θ,φ).* This function is normalized in such a way that the total scattering over the whole 4π solid angle is unity:

$$\int_0^{2\pi} d\varphi \int_0^{\pi} d\theta . p(\theta,\varphi)\sin\theta = 1 \qquad (3.11)$$

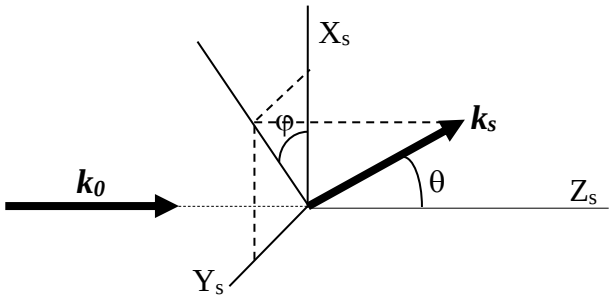

Fig.4. Basic scattering geometry in the "scattering system" (subscript s). The incoming and scattered wavevectors are denoted by $\mathbf{k}_0$ *and* $\mathbf{k}_s$ *respectively.* $|\mathbf{k}| = 2\pi/\lambda$, *with* $\lambda = \lambda_{vacuum}/n$ *(n = refractive index of the medium).*

For the scattering function, several models are available: Dipole- or Rayleigh-scattering, Rayleigh-Gans scattering. Mie scattering, isotropic or peaked-forward scattering. These scattering functions have been described in many textbooks. We refer here to the standard books of Van de Hulst.[15] They will be dealt with in detail in section 4.

The standard method of determining the scattering angles θ and φ is as follows:

- The azimuthal angle φ is given by :

$$\varphi = R.2\pi \qquad (3.12)$$

- For the polar angle θ a normalised cumulative function $C(\theta,\varphi)$ ("Look-up table") is constructed:

$$C(\theta,\varphi) = \frac{C'(\theta,\varphi)}{C'(\pi,\varphi)} \quad \text{with} \quad C'(\theta,\varphi) = \int_0^{\theta} p(\theta',\varphi).\sin\theta'.d\theta', \qquad (3.13)$$

and the angle θ is obtained by taking a fresh random number R and determining the angle for which

$$C(\theta,\varphi) = R \quad . \qquad (3.14)$$

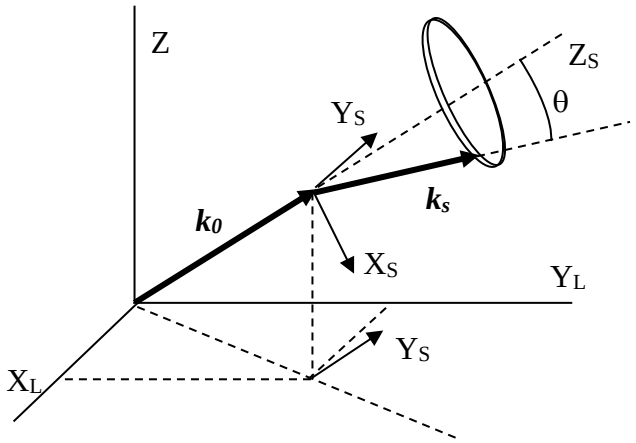

Fig. 5. Relation between the laboratory frame (subscript L) and the local scattering frame (subscript S). The circle indicates the set of possible vector directions for fixed θ and random φ.

The determination of θ can be done by interpolation in the "Look-up table", or by constructing the inverse cumulative function, *e.g.* using a polynomial approximation. However, as we will see in section 4, most relevant scattering functions decrease sharply for small angles, and then a simple polynomial approximation will not suffice. Since these small angles will occur frequently, an interpolation procedure will be more accurate. (In the program, we have adopted this option).

In case polarization effects have to be taken into account, the choice of the angles θ and φ is coupled to the polarization state of the photon. We will deal with polarization in subsection 3.7.

In order to connect the local "scattering coordinate frame" with the "laboratory coordinate frame", we use Fig. 5.

The connection between the S-system and the L-system is constructed in three steps:

$$(1)\ \boldsymbol{z}_S = \frac{\boldsymbol{k}_0}{|\boldsymbol{k}_0|} \quad ; \quad (2)\ \boldsymbol{y}_S = \frac{\boldsymbol{z}_L \times \boldsymbol{z}_S}{|\boldsymbol{z}_L \times \boldsymbol{z}_S|} \quad ; \quad (3)\ \boldsymbol{x}_S = \frac{\boldsymbol{y}_S \times \boldsymbol{z}_S}{|\boldsymbol{y}_S \times \boldsymbol{z}_S|} \tag{3.15}$$

This means that

$$\boldsymbol{k}_S = |\boldsymbol{k}_S| \left[\boldsymbol{x}_S \cos\varphi.\sin\theta + \boldsymbol{y}_S \sin\varphi.\sin\theta + \boldsymbol{z}_S \cos\theta \right]. \tag{3.16}$$

The length of $\boldsymbol{k}_s$ is determined by the local wavelength, as $2\pi/\lambda_{local}$. With this, the scattered wavevector is fixed in the laboratory frame.

In the program the unit vector, along the scattered wave vector, and expressed in the laboratory frame vectors, is updated at each event in which the photon direction is changed.

3.3. Layers and Objects; Boundaries.

Since the program allows for insertion of special structures, like tubes, spheres, mirrors and cones in the layer system, we have to deal with boundaries at flat surfaces (like those between layers) and at curved surfaces.
This subsection contains:

(a) Flat surfaces perpendicular to the Z-axis.
(b) Curved surfaces, or flat surfaces not perpendicular to the Z-axis.

(c) An oblique cylinder.
(d) Cylinders parallel to the surface.
(e) Cylinders parallel to the Z-axis, perpendicular to the surface.
(f) Spheres and Droplets.
(g) Rectangular blocks.
(h) Cones.
(i) Mirrors.
(j) Torusses.
(k) Lenses.
(l) Pupils (diaphragms).
(m) Entrance in an object.

(a) Flat surfaces perpendicular to the Z-axis.

In this situation, the calculation of reflection or refraction angles is relatively simple: according to Snell's Law:

$$\frac{\sin\theta_2}{\sin\theta_1} = \frac{n_1}{n_2}, \tag{3.17}$$

where θ and n denote the angles with the surface normal and the refractive indices in the two media 1 and 2 respectively. See Fig. 6.

The fraction of reflected light is given by the Fresnel relations:

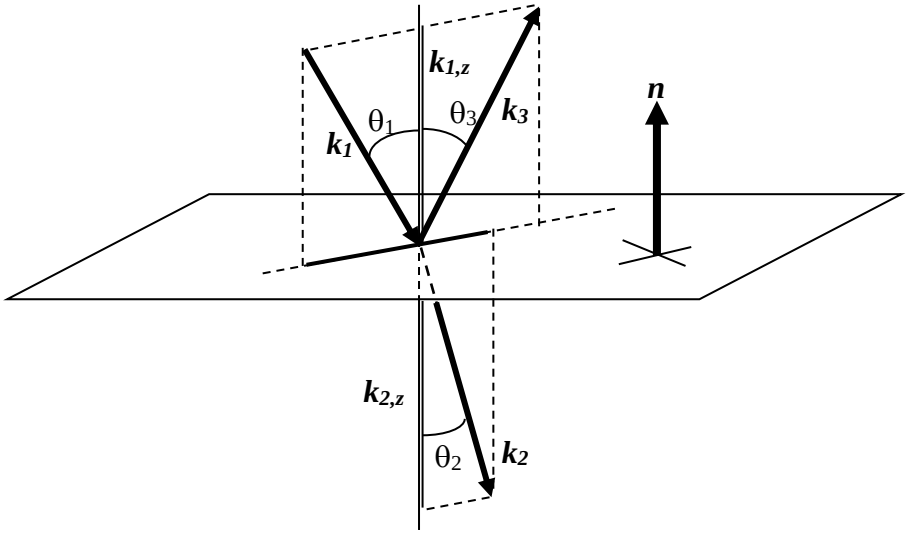

Fig. 6. Reflection or refraction at interfaces. Here the ***k****-vectors denote unit vectors, and* ***n*** *is the unit vector perpendicular to the surface.* $\theta_3 = \theta_1$.

$$\begin{aligned} R_F(\theta_1) &= \left(\frac{n_1 - n_2}{n_1 + n_2}\right)^2 \quad \textit{if} \quad \theta = 0 \\ &= \tfrac{1}{2}\left[\frac{\sin^2(\theta_1 - \theta_2)}{\sin^2(\theta_1 + \theta_2)} + \frac{\tan^2(\theta_1 - \theta_2)}{\tan^2(\theta_1 + \theta_2)}\right] \quad \textit{if} \quad 0 < \theta_1 < \theta_c \\ &= 1 \quad \textit{if} \quad \theta_1 > \theta_c; \quad \textit{with} \quad \theta_c = \arcsin(n_2 / n_1) \end{aligned} \tag{3.18}$$

Reflection takes place if a fresh random number $R < R_F(\theta_1)$, and refraction otherwise.

New unit vectors are calculated according to (see fig. 4):

$$\begin{aligned} &\boldsymbol{k}_{1,z} = \cos\theta_1\,(-\boldsymbol{n})\,; && \boldsymbol{k}_{1,\perp} = \boldsymbol{k}_1 - \boldsymbol{k}_{1,z}\,; \\ &\boldsymbol{k}_{2,z} = \cos\theta_2\,(-\boldsymbol{n})\,; && \boldsymbol{k}_{2,\perp} = (n_1/n_2)\,\boldsymbol{k}_{1,\perp}\,; \\ &\boldsymbol{k}_{3,z} = -\,\boldsymbol{k}_{1,z}\,; && \boldsymbol{k}_{3,\perp} = \boldsymbol{k}_{1,\perp}. \end{aligned} \qquad (3.19)$$

Here the symbol $\perp$ stands for the vector component parallel to the surface.

(b) <u>Curved surfaces, or flat surfaces not perpendicular to the Z-axis.</u>

For the general case of interfaces with a curved surface, at first a new coordinate frame is constructed

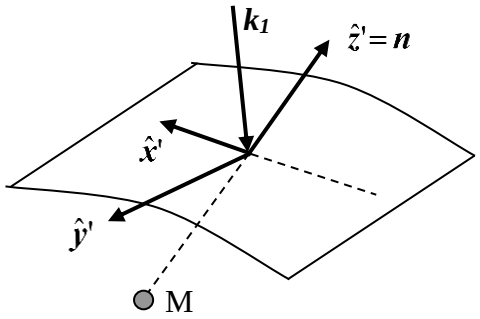

*Fig. 7. Coordinate frame at curved surfaces. Vectors **x'** and **y'** are directed along the surface. M is the centre point (or the point where the normal vector **n** intersects the symmetry axis) of the structure (tube, sphere, etc…).*

as follows (see Figs. 6 and 7):

$$\begin{aligned} &\hat{\boldsymbol{z}}' = \boldsymbol{n} \\ &\hat{\boldsymbol{y}}' = (\boldsymbol{k}_1 \times \boldsymbol{n}) / |\boldsymbol{k}_1 \times \boldsymbol{n}| \\ &\hat{\boldsymbol{x}}' = \hat{\boldsymbol{y}}' \times \hat{\boldsymbol{z}}' \end{aligned} \qquad (3.20)$$

Then the new vectors for refraction and reflection are found to be

$$\begin{aligned} &\boldsymbol{k}_2 = k_{1,x}\hat{\boldsymbol{x}}' - k_{1,z}\hat{\boldsymbol{z}}' \quad ; \quad \boldsymbol{k}_3 = k_{2,x}\hat{\boldsymbol{x}}' + k_{2,z}\hat{\boldsymbol{z}}' \\ &\text{with} \quad k_{1,z} = -k_1.\sin\theta_1 \quad ; \quad k_{1,z} = -k_1.\cos\theta_1 \quad ; \\ &\qquad k_{2,x} = -k_1\sin\theta_2 \quad ; \quad k_{2,z} = \sqrt{k_1^{\,2} - k_{2,x}} \quad ; \end{aligned} \qquad (3.21)$$

and θ_1 and θ_2 are given by Snell's relation (eq.(3.17)).

We will now deal with the geometry of how to determine the intersection points and normal vectors with special cases of curved surfaces.

(c) <u>An oblique cylinder.</u>

See Fig. 8. The point *O'* represents a point on the symmetry axis. Vector ***b*** is the direction vector (unit vector) and vector ***r*** points to the surface points.

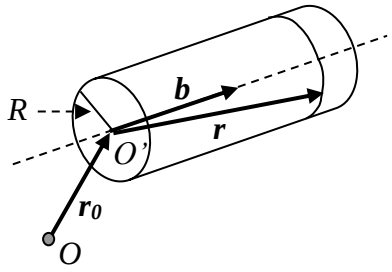

Fig. 8. Vectors for an oblique cylinder. R is the radius and ***b*** *is the direction vector.* ***r*** *directs to a point at the surface.*

The general equation for such a cylinder is

$$\left| \boldsymbol{r} - (\boldsymbol{r} \bullet \boldsymbol{b})\, \boldsymbol{b} \right| = R\,, \tag{3.22a}$$

which in fact is a quadratic equation in the coordinates of the cylinder wall points:

$$\left(x^2 + y^2 + z^2\right) - \left(xb_x + yb_y + zb_z\right)^2 = R^2\,. \tag{3.22b}$$

The vector expression between the absolute bars represents the direction of the normal vector on the surface at point ***r.***
Let vectors $\boldsymbol{p_0}$ **,** $\boldsymbol{p}$ and $\boldsymbol{\Delta p}$ denote the "old" , "new" position of the photon, $\boldsymbol{\Delta p} = \boldsymbol{p} - \boldsymbol{p_0}$ the path length vector, as determined in section 3.1., respectively, and $\boldsymbol{p_0'}$ and $\boldsymbol{p'}$ the same vectors in the internal frame of the cylinder ($\boldsymbol{p_0'} = \boldsymbol{p_0} - \boldsymbol{r_0}$ and $\boldsymbol{p'} = \boldsymbol{p} - \boldsymbol{r_0}$). Then the crossing point $\boldsymbol{p_S}$ with the interface is given by insertion of

$$\boldsymbol{p}' = \boldsymbol{p_0}' + \lambda . \boldsymbol{\Delta p} \tag{3.23}$$

as the vector $\boldsymbol{r}$ into eq. (3.22). Of the two resulting values of λ only those between 0 and 1 are acceptable. The smallest of those λ-value(s) determines the intersection point $\boldsymbol{p_S}$.
In the following, we will use those primed vectors to indicate positions relative to the internal origin point of the object (tube, sphere, cone….).

(d) <u>Cylinders parallel to the surface.</u>

As an example, we will discuss here the case of a straight cylinder parallel to the Y-axis. Insertion of eq. (3.23) into eq. (3.22) leads to

$$\left[(\Delta x)^2 + (\Delta z)^2\right]\lambda^2 + 2\left[p_0{}'_{,x}.\Delta x + p_0{}'_{,z}.\Delta z\right]\lambda + \left[(p_0{}'_{,x})^2 + (p_0{}'_{,z})^2\right] = R^2\,, \tag{3.24}$$

where Δx, Δy and Δz are the components of $\boldsymbol{\Delta p}$**.**
In general this equation will have two λ-roots, with in order to be valid intersection points should be real numbers between 0 and 1. Let us denote these with λ_m and λ_M, with $\lambda_m < \lambda_M$. The λ-value for the intersection point will be equal to λ_m if $0 < \lambda_m < 1$ and $\boldsymbol{p_0}$ is outside the cylinder, and to λ_M if $0 < \lambda_M < 1$ and $\boldsymbol{p_0}$ is inside the cylinder (in that case $\lambda_m < 0$) respectively. See Fig. 9 for a clarification.

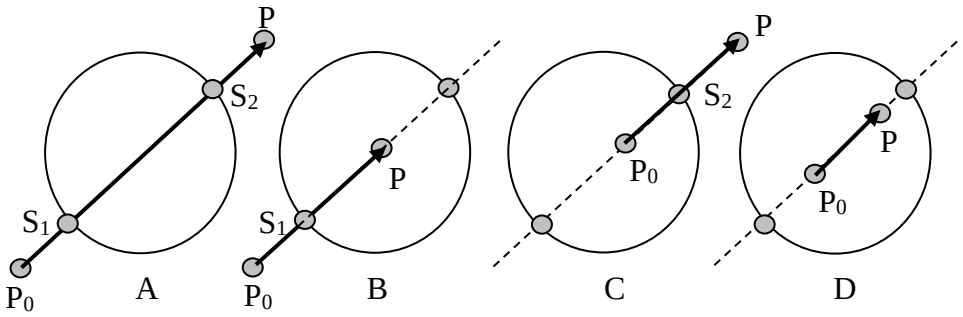

Fig. 9. Intersection points with a cylinder. P_0 and P are the begin- and ends of the path. In case A the intersection point is S_1 (at $\lambda=\lambda_m<\lambda_M$), B: S_1 (at $\lambda=\lambda_m<\lambda_M$), C: S_2 (at $\lambda=\lambda_M$; $\lambda_m<0$), D: no intersection ($\lambda_m<0$ and $\lambda_M>1$).

The direction of the normal vector $\boldsymbol{n_S}$ on the cylinder surface at the intersection point is given by

$$\boldsymbol{n}_S \,//\, \left(p_{S,x} - r_{0,x}, 0, p_{S,z} - r_{0,z}\right) . \tag{3.25}$$

Similar expressions can be formulated for cylinders parallel to the X-axis. In the program both X- and Y-cylinders have infinite length. For cylinders parallel to the Z-axis one also has to take into account that those cylinders may have cover lids and bottom at an interface between layers or with the surface. We will deal with that shortly.

Now we will discuss the option of more than one cylinder, in the form of linear arrays of those cylinders. This means that the program can handle an infinite number of cylinders, arranged next to each other, with constant spacing distance, as is shown in Fig. 10.

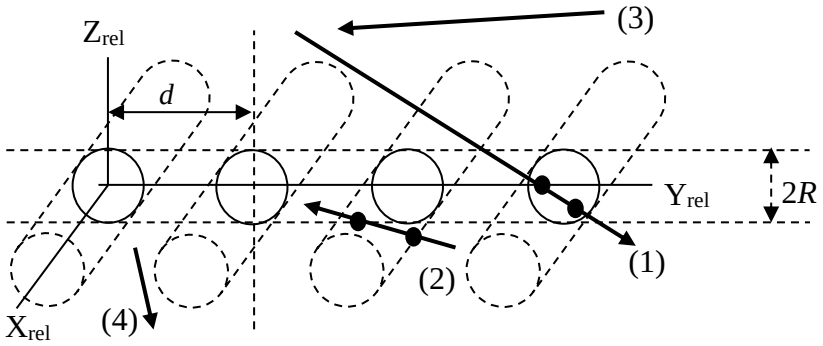

Fig. 10. An array of cylinders parallel to the X-axis. The dots • indicate intersection points. With the subscript "rel" we denote relative coordinates with respect to the generating cylinder of the set. R = radius; d = repetition distance. For paths (1)…(4): see text.

We denote the position vectors $\boldsymbol{p_0'}$ and $\boldsymbol{p'}$ with respect to the internal frame of the generating cylinder (located at the origin of the "rel"-frame). The repetition distance is *d* and the radius is *R*. The generating cylinder has tube number $t_n = 0$; the adjacent tubes have numbers $t_n = +1, +2 \ldots$ and $-1, -2\ldots$ for tubes at the right and left sides respectively.
For the determination of intersections points we take following reasoning:

- Will the path contain points with $-R < z_{rel} < +R$? In that case

$$\left(p_0{}'_{,z} - R\right)\frac{dp_y}{dp_z} < 0 \quad or \quad \left(p_0{}'_{,z} + R\right)\frac{dp_y}{dp_z} < 0 \qquad , \tag{3.26}$$

and the path will cross one of the planes $z_{rel} = \pm R$, like path (1) or (2) in Fig. 8. If not, no intersection will take place (*e.g.* path (3) or (4) in Fig. 8).

- If eq. (3.26) holds, does the path start inside the volume with boundaries $z_{rel} = \pm R$, or:

$$\left| p_0{}'_{,z} \right| < R \; ? \qquad (3.27)$$

- If eq. (3.27) holds, does the path start inside one of the tubes? If so, following expression must hold:

$$\left| \boldsymbol{p}_0' - t_n \; d \; \hat{\boldsymbol{y}}_{\boldsymbol{rel}} \right| < R \qquad \text{with} \quad t_n = round\left(\frac{p_0{}'_{,y}}{d} \right) \quad . \qquad (3.28)$$

The operator "round" takes that integer value which is nearest to the argument between the brackets. Now we can solve the analogous eq. (3.24) for cylinders parallel to the X-axis:

$$\left[(\Delta y)^2 + (\Delta z)^2 \right] \lambda^2 + 2\left[p_0{}''_{,y} . \Delta y + p_0{}''_{,z} . \Delta z \right] \lambda + \left[(p_0{}''_{,y})^2 + (p_0{}''_{,z})^2 \right] = R^2 , \qquad (3.29)$$

with $\boldsymbol{p_0''} = \boldsymbol{p_0'} - t_n \, d \; \hat{\boldsymbol{y}}_{\boldsymbol{rel}}$.

- In case eq. (3.28) does not hold, then the path starts outside all tubes. In that case we solve eq.(3.29) while taking for t_n the value

$$t_n = trunc\left(\frac{p_0{}'_{,y}}{d} \right), \qquad (3.30)$$

where the operator "trunc" removes the fraction from its argument. However, since according to eq. (3.27) the starting point is inside the volume where $z_{rel} < \pm R$, the only tubes that can be intersected are those with tube numbers t_n and t_n+1, we have to solve eq.(3.29) for those two tubes only.
- However, in case eq.(3.27) does not hold, the path will start outside the volume where $z_{rel} < \pm R$. Then first the intersection point with the nearest of the two planes $z_{rel} = \pm R$ is calculated, and from there the procedure is followed as in the case of a valid eq.(3.27).
- Finally, the intersection point is corrected for the coordinate shifts due to the tube number being ≠ 0 and the relative position of the generating tube (at tube number $t_n = 0$).

(e). <u>Cylinders parallel to the Z-axis.</u>

In the case of cylinders parallel to the Z-axis, the program offers the opportunity to insert two-dimensional arrays of cylinders, with equal repetition distance for the X- and Y-pitch. In addition, the cylinders do not have infinite length, as was the case for cylinders parallel to the surface, but will have a coverlid and a bottom lid. This will enlarge the intersection possibilities to be considered. See Fig. 11.

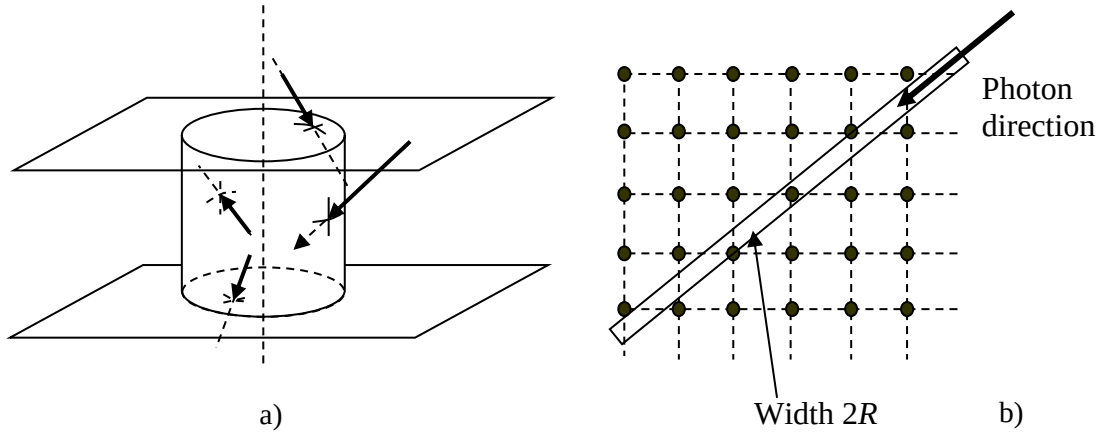

a) b)

Fig. 11. Cylinders parallel to the Z-axis. a) Several possibilities for intersections. b) Two-dimensional array of cylinders; the dots indicate the symmetry axes, pointing into the plane of drawing. The photon will intersect with the nearest cylinder that is positioned within 2R distance of the photon propagation vector.

Now we have to define two tube numbers, one for X-tubes and one for Y-tubes: t_{nx} and t_{ny}. In this case, the reasoning is as follows:

- Is the start position of the path in between the planes of the top and bottom lids of the tubes? If not, the nearest intersection, if any, will occur at the top or bottom lid of one of the tubes. See below.
- Is the start position of the path inside one of the tubes? This is equivalent with:

$$\left| \boldsymbol{p}_0' - t_{ny}\, d\, \hat{\boldsymbol{y}}_{\boldsymbol{rel}} \right| < R \qquad with \qquad t_{ny} = round\left(\frac{p_0'_{,y}}{d} \right) \quad , \tag{3.31}$$

  and simultaneously a similar question for the X-coordinate.
- If so, we can calculate the intersection points with the curved wall and with the two lids of that tube, and take that intersection point (if any) that is reached first. For the curved wall we use a similar expression as eq.(3.29):

$$\left[(\Delta x)^2 + (\Delta y)^2 \right] \lambda^2 + 2\left[p_0''_{,x}.\Delta x + p_0''_{,y}.\Delta y \right] \lambda + \left[(p_0''_{,x})^2 + (p_0''_{,y})^2 \right] = R^2 , \tag{3.32a}$$

$$\boldsymbol{p_0''} = \boldsymbol{p_0'} - t_{nx}\, d\, \hat{\boldsymbol{x}}_{\boldsymbol{rel}} - t_{ny}\, d\, \hat{\boldsymbol{y}}_{\boldsymbol{rel}} . \tag{3.32b}$$

  In case an intersection with the curved wall exists, we check whether an intersection with one of the lids will occur earlier in the path. For the lids we first calculate the intersection points of the (relative) photon vector with the planes $z = z_{top}$ and $z = z_{bottom}$, given by

$$x_S = p_0''_{,x} + \frac{\Delta x}{\Delta z}.(z_{top} - p_0''_{,z}) \quad ; \quad y_S = p_0''_{,y} + \frac{\Delta y}{\Delta z}.(z_{top} - p_0''_{,z}) \quad , \tag{3.33}$$

  (and similarly for the bottom lid) and check whether these points will lye on the lid of one of the tubes, *i.e.* have a distance to the axis of the nearest tube that is smaller than *R*. This procedure is also followed when a photon is approaching a layer with Z-tubes from another layer.
- If eq.(3.31) is not valid for one of the X or Y coordinates, the photon starts outside any tube. Now the firstly encountered tube, with axis within 2*R* distance from the propagation vector of the photon, has to be determined. The tube number of the nearest tube will depend on the sign of $s_x = \Delta x / |\Delta x|$ and $s_y = \Delta y / |\Delta y|$, as is the number sequence of tubes to investigate for the existence of intersection points (going to higher or lower numbers). Following the photon path $\boldsymbol{\Delta p}$ the subsequent tubes most adjacent to the path are interrogated about intersection points by solving a similar equation as eq.(3.32), until that equation has an acceptable solution (between 0 and 1) or the path has been completed (*i.e.* no intersection found). This procedure is illustrated in Fig. 12.

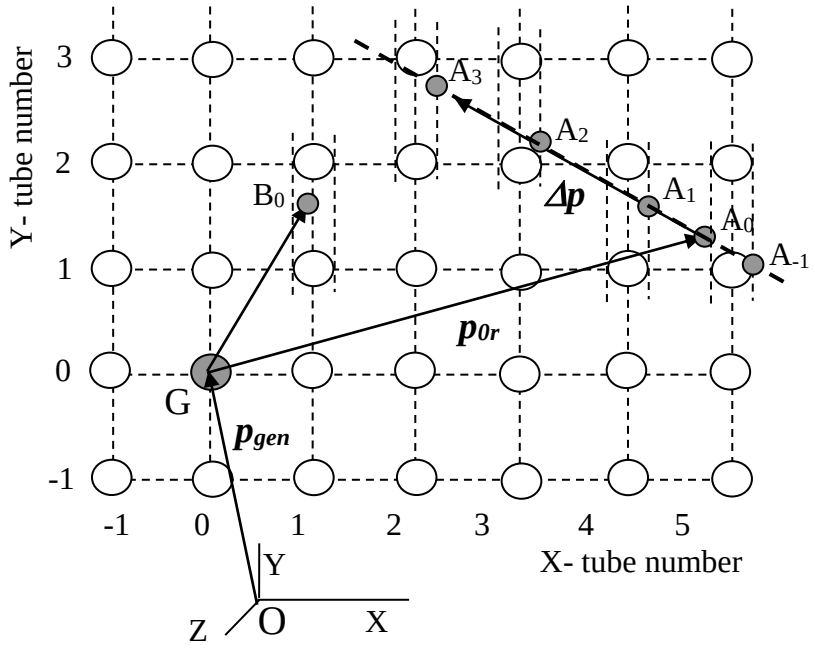

Fig. 12. The procedure for intersection points with Z-tubes. O is the origin of the layer system. G is the generating tube (position $\boldsymbol{p}_{gen}$*). A_0 is the starting point (at* $\boldsymbol{p}_{0r}$*) of the actual photon path* $\Delta\boldsymbol{p}$*. Subsequently the existence of intersections is investigated with adjacent tubes. This is done by shifting point A_0 to A_{-1}, A_1, …A_3…respectively, and solving a similar equation as eq. (3.32) for both adjacent tubes along the Y-axis. In this case points A_1 and A_2 will not lead to intersection points, and A_{-1} and A_3 would have led to intersection points, but outside vector* $\Delta\boldsymbol{p}$ *($\lambda<0$ and $\lambda>1$ respectively). In case the starting point lies within a distance R from the axis (point B_0), that point is not shifted to B_{-1} (analogous to A_{-1}).*

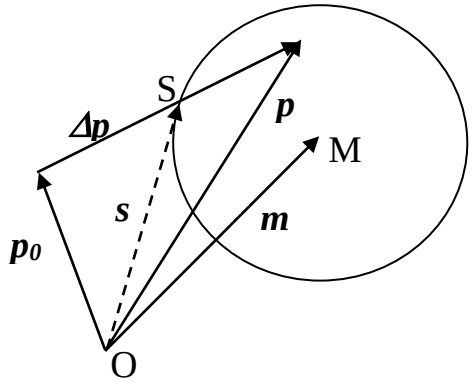

Fig. 13. Determination of the intersection point S with a sphere. $\boldsymbol{p}_0$**,** $\boldsymbol{p}$ *and* $\Delta\boldsymbol{p}$ *are the photon vectors,* $\boldsymbol{m}$ *is the centre point vector and* $\boldsymbol{s}$ *points at the (first encountered) intersection point.*

(f).<u>Spheres and droplets</u>.

As with tubes parallel to the Z-axis, one might define sets of identical spheres arranged in a plane perpendicular to the Z-axis, with equidistant spacing. For those spheres, a similar procedure as for Z-tubes can be followed. Eq. (3.32) is replaced by (see Fig.13)

$$|\boldsymbol{p}-\boldsymbol{p}_0|^2\lambda^2+2(\boldsymbol{p}_0-\boldsymbol{m})\bullet(\boldsymbol{p}-\boldsymbol{p}_0)\lambda+|\boldsymbol{p}_0-\boldsymbol{m}|^2=R^2 \qquad (3.34)$$

which can be written as:

$$\left[(\Delta x)^2+(\Delta y)^2+(\Delta z)^2\right]\lambda^2+2\left[p_0{}''_{,x}.\Delta x+p_0{}''_{,y}.\Delta y+p_0{}''_{,z}.\Delta z\right]\lambda+ \left[(p_0{}''_{,x})^2+(p_0{}''_{,y})^2+(p_0{}''_{,z})^2\right]=R^2 \tag{3.35}$$

with $\boldsymbol{p_0''}$ defined as above (see eq.(3.32)). With these equations the intersection point S can be calculated (if present). For calculating refraction and reflection, one needs the normal vector $\boldsymbol{n_S}$ and the angle of incidence θ_i of $\boldsymbol{\Delta p}$ with $\boldsymbol{n_S}$ at the sphere surface:

$$\cos\theta_i=\frac{\boldsymbol{\Delta p}\bullet\boldsymbol{n}_S}{\left|\boldsymbol{\Delta p}\bullet\boldsymbol{n}_S\right|} \quad ; \quad \boldsymbol{n}_S \,//\, \boldsymbol{s}-\boldsymbol{m}\,. \tag{3.36}$$

The direction of the normal vector depends on the way the surface is crossed, with the photon arriving from the inside or outside. The other axes ($\boldsymbol{l_S}$ and $\boldsymbol{m_S}$) of the coordinate system at point S can be found using

$$\boldsymbol{n_S}\times\Delta\boldsymbol{p}=\boldsymbol{m}_S \quad ; \quad \boldsymbol{n}_S\times\boldsymbol{m_S}=\boldsymbol{l_S}\,, \tag{3.37}$$

with $\boldsymbol{m}_S$ perpendicular to the plane of reflection or refraction and $\boldsymbol{l}_S$ lying in that plane, along the sphere surface.

In the program we have options for:
- A single sphere at a fixed position,
- That sphere, but repeated in a horizontal (XY-) plane,
- Randomly distributed spheres in a cylindrical volume
- One droplet sphere, temporarily generated in front of the photon.

In the program an option is included for distribution of the radii around an average value, with standard deviation.

Droplet spheres.

The above text can be used for spheres with fixed positions. However, in practice that may cost a lot of calculation time, since after each photon transport event one has to investigate whether the photon in the next transport step will hit one (or more) of all of those spheres.
Therefore, we included an option for a temporary sphere, that can be positioned in front of the photon. Using the pathlength of the photon in the surrounding medium, and the distance of the sphere from the actual position of the photon (at the latest transport event) we calculate the probability the photon will "hit" that sphere. If so, the same scattering/reflection/refraction procedure as for a fixed sphere (see above) is used.

To calculate the position of the "temporary" droplet sphere, we use the mean free path of the droplets in their medium, mfp_d, given by

$$mfp_d = c_d.\sigma_d\,, \tag{3.37a}$$

with c_d is the concentration of droplets [1/mm^3] and σ_d is the geometrical cross section (= $\pi\, r^2$: r = radius). The distance of the actual photon position to the droplet (the "virtual"sphere) is then given by

$$\tau_d = -mfp_d\,.\ln(1\text{-}R) \tag{3.37b}$$

with R a random number (0 <= R < 1). The photon will reach the droplet if its path length, given in eq. (3.10) using μ_m (the attenuation coefficient of the surrounding medium), is larger than τ_d , provided no hits with other objects will occur before reaching the droplet.

However, there is a catch. The photon will hit the sphere somewhere at its surface, not necessarily at a spot on the line between the original photon position and the center point of the sphere. The probability to find the "hit"spot under a certain azimuthal angle of the sphere, as seen from its center point, will be $1/(2\pi)$, and the polar angle will be given by a probability proportional to a, where a is the radius of the projection of the "polar" circle around the center axis. See Fig. 13a.

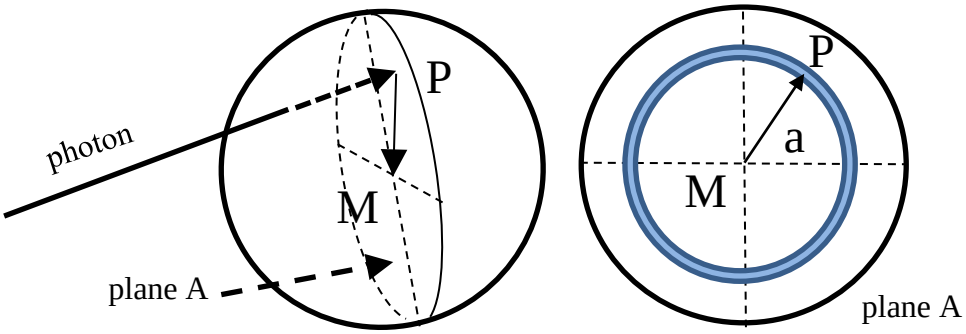

Fig. 13a. The photon will hit plane A (perpendicular to the photon direction vector) in point P, given by radius a (a<=r, the sphere radius)). The center point of the sphere M can be found from P.

Center point M must be positioned somehere on a circle around P. Thus M can be found from P using a random number $R * 2.\pi$,(0<=R<1) for the azimuthal angle, and another random number R for $a = \sqrt{R}.r$. The square root is necessary to account for the circumference of the circle (the probalility of a "hit" at radius a ($0 < a <= r$) will be proportional to the circumference $2\pi a$).
We construct two vectors $\boldsymbol{q_1}$ and $\boldsymbol{q_2}$ in plane A, perpendicular to each other and to the photon direction $\boldsymbol{\Delta p}$, using the scalar and vector products for these three vectors, and normalize the length of $\boldsymbol{q_1}$ and $\boldsymbol{q_2}$ to unity. Then M is found using

$$\boldsymbol{M} = \boldsymbol{P} + a.\cos(\beta).\,\boldsymbol{q_1} + a.\sin(\beta).\,\boldsymbol{q_2} \qquad (3.37c)$$

with β is the angle between vector $\boldsymbol{MP}$ and one of $\boldsymbol{q_1}$ and $\boldsymbol{q_2}$. We thus changed the positioning of P with respect to M, into M with respect to P. And now we may proceed as with a "normal" (i.e. fixed sphere; see above).

(g). <u>Rectangular blocks.</u>

Rectangular blocks, as used in the program, always have their side planes parallel to the laboratory coordinate axes. The position and dimensions are defined using maximum and minimum values for the coordinates of the side planes, *e.g.* x_{max} and x_{min}, and similarly for y and z. All six sides have to be interrogated for the presence of intersection points. For instance, for the block side at $z = z_{max}$, we calculate a ratio $f_{z,max}$ as

$$f_{z,\max} = \frac{z_{\max} - p_{0,z}}{\Delta z} \qquad (3.38)$$

and similarly for all other sides. The smallest value of those six *f*-values, provided between 0 and 1, will determine the side where the first intersection will take place. If no such *f*-value can be found, no intersection point is present.

(h). Cones.

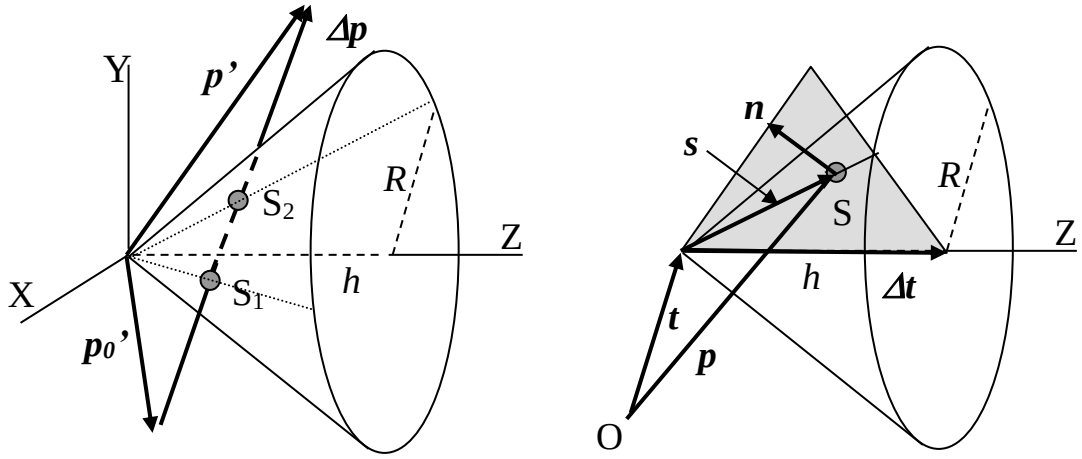

Fig. 14. Intersection with a cone (example: directed along the +Z-axis). The cone is characterized by its direction vector (along the axis) and its opening angle, or its radius R at height h. Right: construction of the normal vector.

The equation for cones is:

$$(x-x_O)^2+(y-y_O)^2-\alpha(z-z_O)^2=0 \quad ; \quad \alpha=(R/h)^2, \tag{3.38}$$

for a cone directed along the Z-axis, as shown in Fig.14. The relevant intersection points are given by

$$(p_0{}'_{,x}+\lambda.\Delta x)^2+(p_0{}'_{,y}+\lambda.\Delta y)^2-\alpha(p_0{}'_{,z}+\lambda.\Delta z)^2=0. \tag{3.39}$$

The smallest value of λ, if between 0 and 1, determines the valid intersection point S, provided the z-component of S is smaller than *h*. However, eq.(3.38) also describes the other half of the cone, and therefore, for the intersection point to be accepted, this point should lie between top and bottom of the cone, which defines an additional condition for point S to exist.
For reflection and refraction, we have to construct the normal vector ***n*** on the surface in point S:

$$\boldsymbol{s}=\boldsymbol{p}-\boldsymbol{t} \quad ; \quad \boldsymbol{v}=(\Delta\boldsymbol{t}\times\boldsymbol{s})\times\boldsymbol{s} \quad ; \quad \boldsymbol{n}=\boldsymbol{v}/|\boldsymbol{v}| \quad , \tag{3.40}$$

with ***t*** and ***Δt*** as the position and direction vectors of the cone, and ***v*** as a vector in S parallel to the cone surface and perpendicular to the plane spanned by ***Δt*** and ***s***. The direction of ***n*** depends on the way the surface is crossed: arriving from the inside or outside. The determination of the angle of incidence is similar to the case of tubes and spheres.

With cones, also an intersection with the bottom is possible. In the coordinate frame of Fig. 12, we have two conditions to be fulfilled:

$$\begin{aligned} &p_0{}'_{,z}+\lambda.\Delta z=h \qquad \text{with} \quad 0<\lambda<1, \\ &(p_0{}'_{,x}+\lambda.\Delta x)^2+(p_0{}'_{,y}+\lambda.\Delta y)^2\le R^2 \end{aligned} \tag{3.41}$$

In all cases the smallest of the λ-values of all possible intersections, if between 0 and 1, should be taken for the intersection point.
In the program the available cones are those with the axis parallel to the ±X, ±Y or ±Z-axis.

(i).Mirrors.

The normal equation of a mirror plane is given, using the normal vector $\boldsymbol{a}$ = (a_1,a_2,a_3), by

$$a_1.x + a_2.y + a_3.z + d = 0, \qquad (3.42)$$

where *d* is a constant. Vector a should point to the half plane where the starting point of the photon path is situated.
We can calculate the vector $\boldsymbol{p}_S$ to the intersection point S by insertion of the photon path ($\boldsymbol{p}_S = \boldsymbol{p}_0 + \lambda.\boldsymbol{\Delta p}$) into eq.(3.42), which will render the λ-value corresponding to S. The direction vector $\boldsymbol{l}$ after reflection is given by

$$\boldsymbol{l} \,//\, \boldsymbol{\Delta p} - 2(\boldsymbol{\Delta p} \bullet \boldsymbol{a}).\boldsymbol{a} \quad ; \quad |\boldsymbol{l}| = (1-\lambda).|\boldsymbol{\Delta p}|. \qquad (3.43)$$

(j).Torusses

We describe a HALF-TORUS. This makes it feasible to combine torusses to a chain, apart from using two half-torusses to produce a closed full-circle torus.
In fig.14a. the situation is depicted.

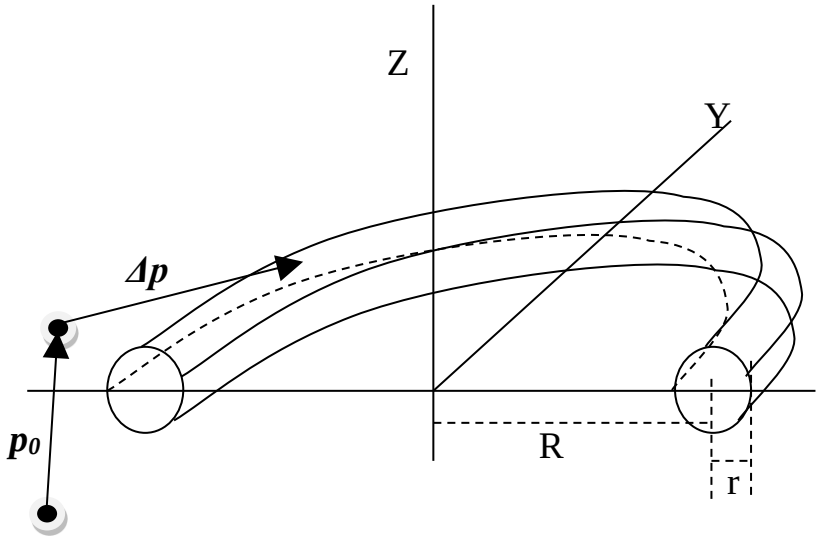

Fig. 14a. A half-torus, symmetry-axis is Z-axis (perpendicular to surface of layer system). Inner and outer radius: r and R respectively.

The general equation of a torus with symmetry-axis parallel to the Z-as, is (apart from the limitation to a half-torus, at pos. Y-values):

$$F \equiv (\sqrt{x^2 + y^2} - R^2)^2 + z^2 - r^2 \qquad (3.44a)$$

where R and r are the outer and inner radius respectively, and with F > 0, = 0, < 0 for points outside, on the wall or inside the torus respectively.
This leads to a 4th-degree equation:

$$(x^2 + y^2 + z^2 + R^2 - r^2)^2 = (2R)^2(x^2 + y^2) \quad . \tag{3.44b}$$

In principle there are 0, 2 or 4 intersections with the photon path, given by

$$\boldsymbol{p} = \boldsymbol{p_0} + \boldsymbol{\lambda}.\Delta\boldsymbol{p} \tag{3.44c}$$

with $0 < \lambda < 1$, provided $|\Delta\mathbf{p}|$ is large enough. Intersections are found by inserting (3.A3) into (3.A2), e.g. $p_x = p_{0x} + \lambda.\Delta p_x$ for x, etc. This produces a 4th degree equation in λ. We need the solution (if present) with the smallest value for λ, provided $0 < \lambda \leq 1$.
Literature provides general solution methods for 4th degree equations. However, we took another approach, using iterations to reach the nearest intersection point, if present. The steps are:

1. Set $\lambda_0 = 0$ and calculate F_0.
2. Define $d\lambda = 1/N$, with N = large enough to make the corresponding $|\Delta p|$ much smaller than the smallest dimension of the torus (normally the inner radius r).
3. Calculate F_i at $\lambda_i = \lambda_0 + i.d\lambda$, with i = 1..$N$.
4. If $F_i * F_{i-1} < 0$, an intersection point is crossed between λ_{i-1} and λ_i. In that case:
    a. Set $\lambda_0 = \lambda_{i-1}$ and reduce $d\lambda$ systematically: $d\lambda_{new} = d\lambda_{old}/2$.
    b. Set $N = 2$.
    c. go repeatedly to step 3 and repeat this procedure until $d\lambda$ becomes small enough (e.g. < 1 µm).
5. If $F_i * F_{i-1} < 0$ is not met for any i = 1..N, then there will be no intersection point.

In case the initial $d\lambda$ is not small enough, there will be a chance that two closeby intersection points will be missed.
The initial process in step 1 can be accelerated by precalculating the approximate entrance point of the photon path into the torus.

(k) Lenses

Lenses can be thought of as consisting of two partial surfaces of two spheres. We consider lenses with symmetry axis parallel to the Z-axis, pointing inward into the layer system. There are 4 possible situations (see Fig. 14b):
We use the convention of positive and negative radii when the centre point of the curvature lays behind and in front of the lens respectively.
The radius r_S and the Z-coordinate z_S of the circles of the points of intersection (x_S, y_S, z_S) (if present) of the two surfaces can be found from:

$$r_S^2 = R_1^2 - (z_S - Z_1)^2 = R_2^2 - (z_S - Z_2)^2 \;; \quad r_S^2 = x_S^2 + y_S^2 \tag{3.44d}$$

The Z-coordinates z_{d1} and z_{d2} at diameter d are given by:

$$(d/2)^2 = R_1^2 - (z_{d1} - Z_1)^2 \text{ and } (d/2)^2 = R_2^2 - (z_{d2} - Z_2)^2 \tag{344e}$$

We will limit the physical diameter of each lens surface to the value of its spherical diameter.
In situation D the physical diameter of the lens will determine d of the lens as a whole. In situations A, B, and C the diameter has a physical maximum at the intersection points of the two lens parts. Then $z_{d1} = z_{d2}$.
Intersections of the photon vector (see (3.44c)) with the front and backside are similar to those with a sphere surface. See subsection (f).

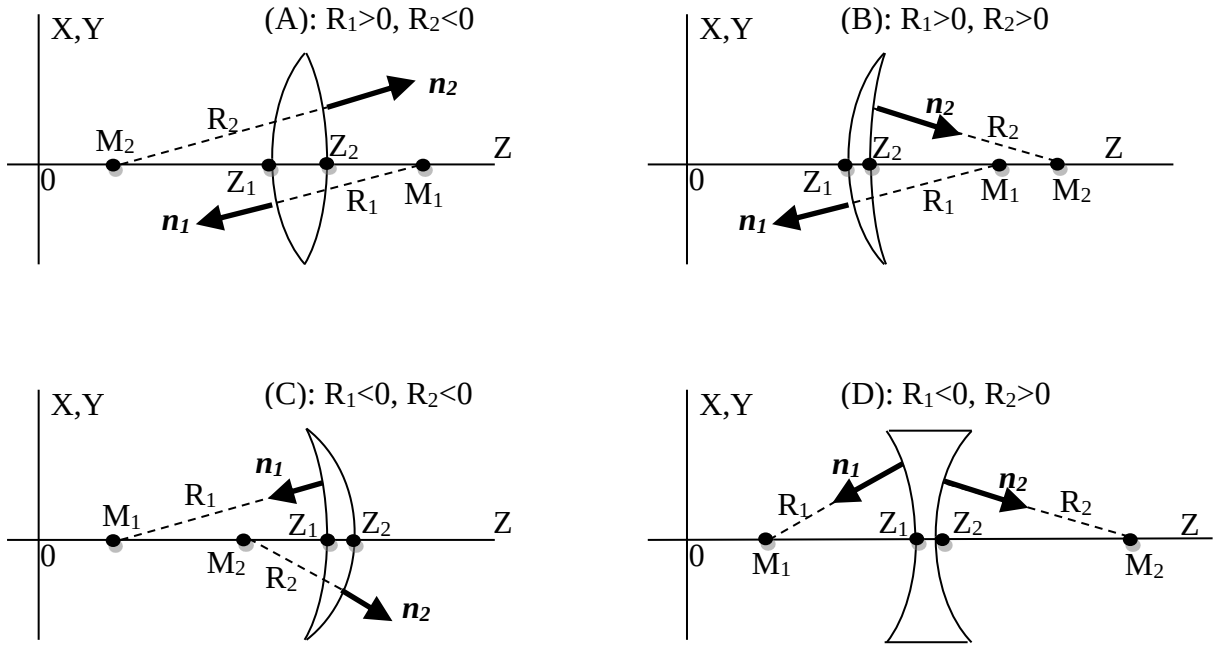

Fig.14b. Lenses: four possible situations. Also indicated: normal vector at the surface; always pointing outward for incoming photons (inward for uitgoing photons).

Intersections with the side wall of the lens (in situation D, and in A, B, and C when the diameter is smaller than the maximum diameter) are given by eqns. (3.22a) and (3.32a). Solving (3.32a) will produce zero or two intersection points (separate or coinciding), given by λ_1 and λ_2. We need the solution with the smallest value of λ, which will bring an intersection if

$$(0 < \lambda \leq 1) \wedge (z_s \geq z_{d1}) \wedge (z_s \leq z_{d2}). \qquad (3.44f)$$

However, since generally lens walls are not used for photon transport, it is advisable to discard these photon paths during the simulation.

In Fig. 14b. also the normal vectors to the lens surfaces are indicated, for photons incident from outside the lens. The vector coordinates are given by the normalized vector difference of the position of the actual point of entrance into the lens and that of the centre of the curvature (M_1 and M_2 respectively). It should be noted that for photons travelling inside the lens object, the direction of these normal vectors has to be inverted.

The effective focal length f of the lens is calculated using the "Lens Makers Formula":

$$\frac{1}{f} = (n-1)\left[\frac{1}{R_1} - \frac{1}{R_2} + \frac{(n-1).d}{nR_1R_2}\right]. \qquad (3.44g)$$

where n is the refractive index with respect to the surrounding medium, and d is the lens thickness at the symmetry axis point: $d = Z_2 - Z_1$.

(l). Pupils (Diaphragms)

Pupils are defined as circular openings in a absorbing screen, with the symmetry axis parallel to the Z-axis, thus perpendicular to the surface of the layer system.
Photons will pass provided their Z-position when passing the opening isd smaller than the radius or the opening.

(m). <u>Entrance in an object.</u>

When a photon enters a new layer, it is possible that it immediately will enter a "object" in that layer rather than first the material of the layer itself. An example is the entrance in a layer where a single Z-tube or a set of those tubes is present. This has to be checked separately. Therefore, the photon, after reaching that interface, is temporarily propagated further along its path over a very small distance, to ensure that it is placed inside. The next step is to check whether the following condition *C* is true (with $\boldsymbol{p_c}$ as the temporary position vector, $\boldsymbol{p_c}$**'** as that vector relative to the object or to the generating object in case of an array, and *d* as the repetition distance (if present)) :

- Rectangular block:
  $C = (p_{cx} > x_{\min}) \wedge (p_{cx} < x_{\max}) \wedge (p_{cy} > y_{\min}) \wedge (p_{cy} < y_{\max}) \wedge (p_{cz} > z_{\min}) \wedge (p_{cz} < z_{\max}),$
- Cylindrical tube(s) parallel to the X-axis : (3.44h)
  $C = \left[(p_c{}'_{,y} - q_y)^2 + (p_c{}'_{,z})^2 < R^2 \right]$ with
  $q_y = 0$ if $d = 0$; otherwise $q_y = round(p_c{}'_{,y} / d).d$ (3.44i)
- Cylindrical tube(s) parallel to the Y-axis :
  $C = \left[(p_c{}'_{,x} - q_x)^2 + (p_c{}'_{,z})^2 < R^2 \right]$ with
  $q_x = 0$ if $d = 0$; otherwise $q_x = round(p_c{}'_{,x} / d).d$ (3.44j)
- Cylindrical tube(s) parallel to the Z-axis :
  $C = \left[(p_c{}'_{,x} - q_x)^2 + (p_c{}'_{,y} - q_y)^2 < R^2 \right] \wedge \left[p_{c,z} > z_{top} \right] \wedge \left[p_{c,z} < z_{bottom} \right],$ (3.44k)
  with z_{top} and z_{bottom} as the z-coordinates of the top and bottom lids of the tube(s),
- Spheres :
  $C = \left[(p_c{}'_{,x} - q_x)^2 + (p_c{}'_{,y} - q_y)^2 + (p_c{}'_{,z})^2 < R^2 \right],$ (3.44l)
- Cones (*e.g.* with symmetry axis (bottom → top) pointing to +Z-axis) :
  $C = (p_c{}'_{,z} > 0) \wedge (h > 0) \wedge (0 < p_c{}'_{,z} / h < 1) \wedge \left[(p_c{}'_{,x})^2 + (p_c{}'_{,y})^2 < (p_c{}'_{,z}.R / h)^2 \right],$
  and analogously for the five other directions, (3.44m)
- Oblique cylinders (using $\boldsymbol{b}$ as the directional unit vector along the symmetry axis):
  $C = \left[(p_c{}'_{,x})^2 + (p_c{}'_{,y})^2 + (p_c{}'_{,z})^2 - (\boldsymbol{p_c}' \bullet \boldsymbol{b})^2 < R^2 \right] \wedge \left[p_{c,z} > z_{top} \right] \wedge \left[p_{c,z} < z_{bottom} \right].$ (3.44n)
- Mirrors (with $\boldsymbol{b}$ as the normal vector on the mirror surface) :
  $C = (\boldsymbol{p}' \bullet \boldsymbol{b} = 0)$ (3.44o)
- (Half-) Torus, with *R* and *r* being the outer and inner radii, and with its plane perpendicular to the Y-axis:
  $C = \left[\sqrt{(p_c{}'_{,x})^2 + (p_c{}'_{,z})^2} - R \right]^2 + (p_c{}'_{,y})^2 - r^2 < 0$ (3.44p)
- Lenses with symmetry axis parallel to the Z-axis (see subsection (l)): with $r^2 = (p_c{}'_{,x})^2 + (p_c{}'_{,y})^2$:
  $C = [r < d/2] \wedge$ (3.44q)
  $[\{(R_1 > 0) \wedge (R_2 < 0) \wedge (p_c{}'_{,z} \geq Z_1 + |R_1| - \sqrt{(R_1{}^2 - r^2)}) \wedge (p_c{}'_{,z} \geq Z_2 - |R_2| + \sqrt{(R_2{}^2 - r^2)})\} \vee$
  $\{(R_1 > 0) \wedge (R_2 > 0) \wedge (p_c{}'_{,z} \geq Z_1 + |R_1| - \sqrt{(R_1{}^2 - r^2)}) \wedge (p_c{}'_{,z} \geq Z_2 + |R_2| - \sqrt{(R_2{}^2 - r^2)})\} \vee$
  $\{(R_1 < 0) \wedge (R_2 < 0) \wedge (p_c{}'_{,z} \geq Z_1 - |R_1| + \sqrt{(R_1{}^2 - r^2)}) \wedge (p_c{}'_{,z} \geq Z_2 - |R_2| + \sqrt{(R_2{}^2 - r^2)})\} \vee$
  $\{(R_1 < 0) \wedge (R_2 > 0) \wedge (p_c{}'_{,z} \geq Z_1 - |R_1| + \sqrt{(R_1{}^2 - r^2)}) \wedge (p_c{}'_{,z} \geq Z_2 + |R_2| - \sqrt{(R_2{}^2 - r^2)})\}\ ]$

3.4. Absorption.

Normally the position of the photon, together with its directional angles, is stored upon reflection or transmission. However, when in absorption mode, the position of absorption will be stored, together with the directional angles of the previous (last) photon path. These angles are stored using the normal convention for the polar angle θ and azimuthal angle φ:

$$\Delta \boldsymbol{p} = |\Delta \boldsymbol{p}| \,.\, (\sin\theta.\cos\varphi, \sin\theta.\sin\varphi, \cos\theta), \tag{3.45}$$

with θ = 0, if the direction is pointing along the +Z-axis, inside the sample, and φ in the XY-plane, as the angle with the X-axis.

3.5. Polarisation.

(1). Polarisation in scattering events.

To handle polarisation effects in scattering events we use Van de Hulst 's scattering matrix [15], with $\boldsymbol{E_0}$ and $\boldsymbol{E}$ as the incoming and scattered electric field vectors:

$$\begin{pmatrix} E_l \\ E_r \end{pmatrix} = \frac{\exp(-ikr - i\omega t)}{i.4\pi\varepsilon_m kr} \begin{pmatrix} S_2 & S_3 \\ S_4 & S_1 \end{pmatrix} \begin{pmatrix} E_{l0} \\ E_{r0} \end{pmatrix} \tag{3.46}$$

where the subscript *l* and *r* denote parallel and perpendicular polarisation respectively. In the following we will limit ourselves to spherical particles, where S_3 and S_4 are = 0. The other parameters S_1 and S_2 are functions of the polar scattering angle θ. The factor $(4\pi\varepsilon_m)$ can be inserted in the *S*-functions as well. Note that Van de Hulst uses Gaussian units instead of SI-units, which means that he does not take the factor $(4\pi\varepsilon_m)$ into account.
The Stokes vector $\boldsymbol{S^T} = (I,Q,U,V)$ can be constructed from this matrix:

$$\begin{aligned} I &= E_l E_l^* + E_r E_r^* \\ Q &= E_l E_l^* - E_r E_r^* \\ U &= E_l E_r^* + E_r E_l^* \\ V &= i(E_l E_r^* - E_r E_l^*). \end{aligned} \tag{3.47}$$

With

$$\begin{aligned} E_l &= a_l \exp(-ik_z - i\omega t - i\varepsilon_l) \\ E_r &= a_r \exp(-ik_z - i\omega t - i\varepsilon_r) \end{aligned}, \tag{3.48}$$

it follows:

$$\begin{aligned} I &= a_l^2 + a_r^2 \qquad & U &= 2a_l a_r.\cos\delta \qquad & \delta &= \varepsilon_l - \varepsilon_r \\ Q &= a_l^2 - a_r^2 \qquad & V &= 2a_l a_r.\sin\delta \end{aligned} \tag{3.49}$$

For normal (non-birefringent) materials $\varepsilon_l = \varepsilon_r$. The degree of polarisation is defined as

$$\Phi_P = \frac{1}{I}\sqrt{Q^2 + U^2 + V^2} \tag{3.50}$$

Transformation of the Stokes vector upon scattering (for spherical particles) is given by

$$\boldsymbol{S^T_n} = \overline{\overline{\boldsymbol{F}}} \,.\, \boldsymbol{S^T} \tag{3.51}$$

with
$$\overline{\overline{\boldsymbol{F}}} = \begin{pmatrix} \frac{1}{2}(M_2 + M_1) & \frac{1}{2}(M_2 - M_1) & 0 & 0 \\ \frac{1}{2}(M_2 - M_1) & \frac{1}{2}(M_2 + M_1) & 0 & 0 \\ 0 & 0 & S_{21} & -D_{21} \\ 0 & 0 & D_{21} & S_{21} \end{pmatrix} \tag{3.52}$$

and

$$\begin{aligned} M_k &= S_k S_k^* = |S_k|^2 \; ; k = 1,2 \\ S_{21} &= \tfrac{1}{2}(S_1 S_2^* + S_2 S_1^*) \\ D_{21} &= \tfrac{1}{2} i (S_1 S_2^* - S_2 S_1^*) \end{aligned} \tag{3.53}$$

and so we arrive at the Mueller matrix $\overline{\overline{\boldsymbol{M}}}$ replacing $\overline{\overline{\boldsymbol{F}}}$:

$$\overline{\overline{\boldsymbol{M}}} = \begin{pmatrix} m_{11} & m_{12} & 0 & 0 \\ m_{12} & m_{11} & 0 & 0 \\ 0 & 0 & m_{33} & m_{34} \\ 0 & 0 & -m_{34} & m_{44} \end{pmatrix} \tag{3.54}$$

where the parameters m_{11} … m_{44} depend on the particular scattering function and the scattering angles θ and φ. We will deal with those parameters in the next section.

Transformation of the Stokes vector upon scattering has to be preceded by a rotation from the actual coordinate system (given by the unit vectors $\boldsymbol{e_l}$, $\boldsymbol{e_r}$, $\boldsymbol{e_p}$, with directions parallel and perpendicular to the actual polarisation direction, and parallel to the direction of propagation respectively) to that in the scattering plane ($\boldsymbol{e_l'}$, $\boldsymbol{e_r'}$, $\boldsymbol{e_p'}$, with $\boldsymbol{e_p' = e_p}$). This rotation is determined by the rotation matrix $\overline{\overline{\boldsymbol{R}}}$:

$$\overline{\overline{\boldsymbol{R}}} = \begin{pmatrix} 1 & 0 & 0 & 0 \\ 0 & \cos 2\varphi & -\sin 2\varphi & 0 \\ 0 & \sin 2\varphi & \cos 2\varphi & 0 \\ 0 & 0 & 0 & 1 \end{pmatrix}, \tag{3.55}$$

with φ as the azimuthal scattering angle (see Fig.15).

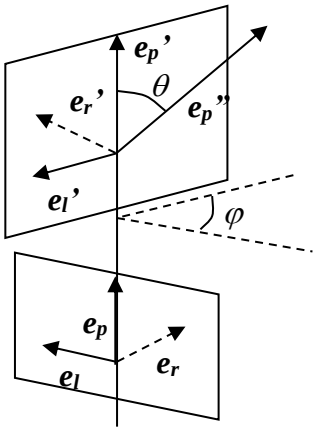

Fig. 15.. Coordinate frames of subsequent scattering events. The propagation vector $\boldsymbol{e_p}$ *is first transformed into* $\boldsymbol{e_p}$**'** *(by rotation over* φ*) and then to* $\boldsymbol{e_p}$**"** *(by rotation over* θ*). The vectors* $\boldsymbol{e_l}$ **,** $\boldsymbol{e_r}$ *and* $\boldsymbol{e_l}$**'** **,** $\boldsymbol{e_r}$**'** *are frame vectors parallel and perpendicular to the scattering planes.*

Subsequent multiplication with the Mueller matrix produces the new Stokes vector in the coordinate frame (**e_l", e_r", e_p"**) connected to the new propagation direction **e_p"** (with **e_p"** • **e_p'** = cos θ):

$$e_r"=\begin{pmatrix}\cos\varphi\\ \sin\varphi\\ 0\end{pmatrix} \quad ; \quad e_l"=\begin{pmatrix}-\cos\theta.\sin\varphi\\ \cos\theta.\cos\varphi\\ \sin\theta.\end{pmatrix} \quad ; \quad e_p"=\begin{pmatrix}\sin\theta.\sin\varphi\\ -\sin\theta.\cos\varphi\\ \cos\theta.\end{pmatrix} \quad . \qquad (3.60)$$

Subsequent scattering events (θ_i,φ_i, with i=*1...n*) will result in

$$\boldsymbol{S}^T{}_{result} = \left[\prod_{i=1}^{n} \overline{\overline{\boldsymbol{M}}}(\theta_i)\overline{\overline{\boldsymbol{R}}}(\varphi_i)\right].\boldsymbol{S}^T{}_0\,, \qquad (3.61)$$

and this determines the polarisation state of the emerging photon. Here the vector $\boldsymbol{S^T_0}$ is the Stokes vector of the incoming photon, given by eq.(3.47) after determination of the parallel and perpendicular directions corresponding to $E_{//}$ and $E_{\perp}$.

In the non-polarised case (natural light), the scattering angles can be determined using two subsequent random numbers. In the polarised state that is not the case any more. When determining an angle φ using a random number, the angle θ is determined by the joint probability:

$$p(\theta,\varphi) = m_{11}(\theta) + m_{12}(\theta).\,(Q.\cos 2\varphi + U.\sin 2\varphi\,) / I\,. \qquad (3.62)$$

Yao and Wang's approach [16] calculates θ with m_{11} (as in fact is done with natural light) and subsequently φ with eq.(3.62).
Several authors have dealt with polarization of light in turbid media.[16-21].

(2). Polarisation at interfaces.

Changing of polarisation direction may also occur at interfaces, where reflection or refraction takes place. With α_1, α_2 and α_3 as the angles of the electric vector $\boldsymbol{E}$ with the plane of incidence (formed by the incident propagation direction and the normal on the surface at the point of intersection) for the

incident (1), refracted (2) and reflected (3) vector respectively (see Fig.4), and *A* as the field amplitude it can be shown (see *e.g.* Born and Wolf [22]) that

$$A_{1,l} = A_1.\cos\alpha_1 \quad ; \quad A_{1,r} = A_1.\sin\alpha_1 \tag{3.63}$$

where α_1 can be derived from the components of the incident Stokes vector using

$$A_{1,l} = \tfrac{1}{2}(I+Q) \quad ; \quad A_{1,r} = \tfrac{1}{2}(I-Q) \tag{3.64}$$

Now we calculate the amplitudes of the reflected and transmitted (refracted) wave

$$\begin{aligned} A_{3,l} &= \frac{\tan(\theta_1-\theta_2)}{\tan(\theta_1+\theta_2)}A_{1,l} \quad ; \quad A_{3,r} = -\frac{\sin(\theta_1-\theta_2)}{\sin(\theta_1+\theta_2)}A_{1,r} \qquad \text{with} \quad \frac{\sin\theta_1}{\sin\theta_2} = \frac{n_2}{n_1} \\ A_{2,l} &= \frac{2\sin\theta_2.\cos\theta_1}{\sin(\theta_1+\theta_2).\cos(\theta_1-\theta_2)}A_{1,l} \quad ; \quad A_{2,r} = \frac{2\sin\theta_2.\cos\theta_1}{\sin(\theta_1+\theta_2)}A_{1,r} \\ \tan\alpha_3 &= -\frac{\cos(\theta_1-\theta_2)}{\cos(\theta_1+\theta_2)}\tan\alpha_1 \quad ; \quad \tan\alpha_2 = \cos(\theta_1-\theta_2).\tan\alpha_1 \end{aligned} \tag{3.65}$$

From these we can derive the corresponding Stokes vector coefficients and Mueller matrices $\overline{\overline{\boldsymbol{M}}}_R$ and $\overline{\overline{\boldsymbol{M}}}_T$, where the subscripts R and T stand for reflection and transmission (refraction). However, to construct the new Stokes vector it is easier by using the amplitudes directly.

To find out whether reflection or refraction (transmission) will take place, we have to look at the reflectivity *R* and transmittivity *T* of the energy instead of those of the amplitude:

$$\begin{aligned} R &= \frac{\left|A_{3,l}\right|^2}{\left|A_{1,l}\right|^2}\cos^2\alpha_1 + \frac{\left|A_{3,r}\right|^2}{\left|A_{1,r}\right|^2}\sin^2\alpha_1 \quad ; \\ T &= \frac{n_2\cos\theta_2}{n_1\cos\theta_1}\left[\frac{\left|A_{2,l}\right|^2}{\left|A_{1,l}\right|^2}\cos^2\alpha_1 + \frac{\left|A_{2,r}\right|^2}{\left|A_{1,r}\right|^2}\sin^2\alpha_1\right] \end{aligned} \tag{3.66}$$

where we can verify that

$$R + T = 1 \tag{3.67}$$

The procedure for handling reflection and refraction at interfaces is as follows:

- Rotate the coordinate frame of the incoming photon to the coordinates of the plane of reflection, using a rotation matrix as in eq. (3.55);
- Determine whether reflection or refraction will take place, using eq.(3.67) and a fresh random number R_N. Reflection will take place if $R_N \le R$, and refraction otherwise.
- Construct the new coordinate frame for the photon and the new Stokes vector, using eq.(3.65).

4. Scattering Functions.

Now we introduce various scattering functions that are frequently used in light scattering simulations. In most cases, we will follow the treatment of Van de Hulst[15] and of Ishimaru[2,3]. Further references can be found there.

Various scattering functions are available, depending upon the size of the scattering particles. A rough description is given in the table, in which the **approximate** region of applicability is presented as a function of the size of the scattering particles, measured in terms of the wavelength λ.

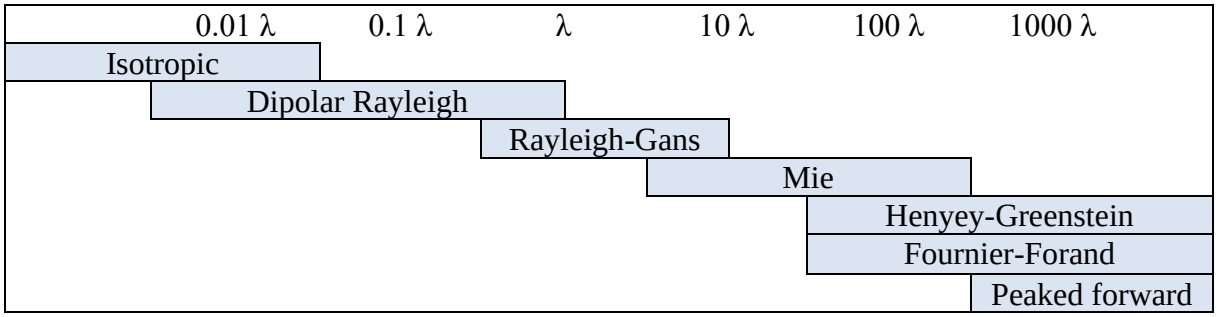

Of these, "Henyey-Greenstein" (sec.4.5), "Gegenbauer" (sec.4.6), "Peaked forward" (4.7) and "Fournier-Forand" (sec. 4.8) only give angular dependent functions, while the other four (sec.4.1-4.4) describe absolute scattering cross sections with angular dependences.

In matters of light scattering by particles two parameters are important: the aspect ratio x and the relative refractive index n_{rel}. The aspect ratio is given by

$$x = \frac{2\pi a}{\lambda_{med}} = ka \quad ; \quad \lambda_{med} = \frac{\lambda_{vac}}{n_{med}}, \tag{4.1}$$

where a denotes the radius of the particle, λ the wavelength of the light and k the modulus of the wavevector. The subscripts *med* and *vac* denote "medium" and "vacuum" respectively. The relative index n_{rel} is the index of the particles with respect to the surrounding medium.

We start with very small particles (small compared to the wavelength: $x<<1$), giving rise to "dipolar" or "Rayleigh" scattering. When gradually increasing the radius we encounter "Rayleigh-Gans" or "Debije"-scattering and finally scattering by large particles ($x>>1$). Generally valid expressions were developed by Mie ("Mie"-scattering). Finally we have expressions of a more phenomenological nature, like "Henyey-Greenstein"-scattering or "peaked-forward"-scattering.

We will use the *geometrical* and *scattering cross sections* σ_g and σ_s [m^2], being the real and the apparent shadow of the particle, and the efficiency factor $Q_{sca} = \sigma_s / \sigma_g$, with $\sigma_g = \pi a^2$.

The ultimate way of treating scattering in numerical simulation is to use the *scattering coefficient* μ_s (in m^{-1}), defined as

$$\mu_s = n_s \sigma_s , \tag{4.2}$$

with n_s as the particle concentration (in m^{-3}). The scattering coefficient is a measure for the average number of scattering events per unit of length. Normally in tissue the scattering is predominantly in forward direction, which means that randomisation of the photon direction only will occur after a

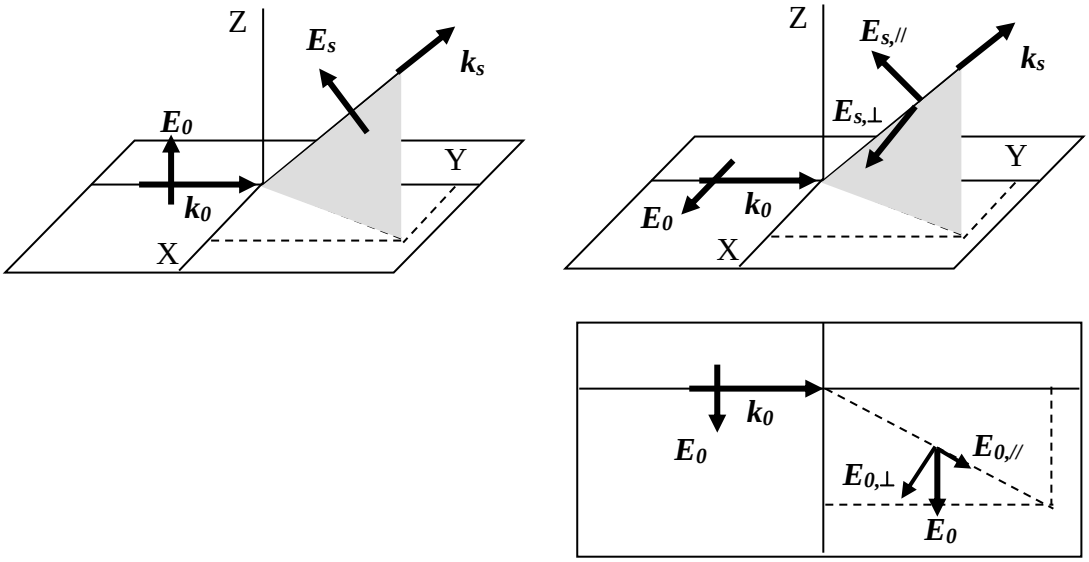

Fig. 16. The meaning of the double vectorial product in determining the direction of scattering and polarization, for two cases: polarisation perpendicular to the XY-plane (left) and parallel to that plane (right). Here ε is taken as a scalar.

relatively large number of scattering events. Therefore, in those cases it is worth while to use the *reduced scattering coefficient μ_s'*, defined as

$$\mu_s' = \mu_s(1-g)\,, \tag{4.3}$$

where *g* stands for the averaged cosine of the polar scattering angles during those events. This value will be 1 for perfectly forward scattering and 0 for isotropic scattering. For tissue $g \approx$ 0.8-0.9 and for blood $g \approx$ 0.95-0.99.

Standard electromagnetic theory for light scattered by dipoles leads to the expression:

$$\boldsymbol{E}_s(\boldsymbol{R},t) = -\frac{1}{4\pi\varepsilon_0 R}\iiint_V d^3\boldsymbol{r} \quad \boldsymbol{k}_s \times \boldsymbol{k}_s \times \left[\overline{\overline{\boldsymbol{\varepsilon}}}(\boldsymbol{r},t') \bullet \boldsymbol{E}_0(\boldsymbol{r},t')\right] \tag{4.4}$$

with $\boldsymbol{E_s}$ and $\boldsymbol{E_0}$ as the scattered and the incoming electric field respectively; $\boldsymbol{R}$ is the vector from the scatttering volume *V* to the point of detection, $\boldsymbol{k_s}$ is the scattered wave vector in that direction, and $\overline{\overline{\boldsymbol{\varepsilon}}}$ is the dielectric tensor (which frequently reduces to a scalar). The time *t'* is the reduced time, given by

$$t' = t - \frac{|\boldsymbol{R}-\boldsymbol{r}|}{c} \tag{4.5}$$

with *c* as the light velocity in the media. In eq. (4.4) the dimensions of the scattering volume *V* are assumed to be small compared to *R*. The significance of the double vector product is illustrated in Fig. 16. For a derivation: see www.demul.net/frits, scroll to "Montcarl" and see the youtube-movies .
The Fournier-Forand scattering function was derived for use with (ocean) water including particles.

4.1. Dipolar (Rayleigh).

With dipolar scattering, the particles are assumed to be so small that light scattered from different oscillating electrical dipoles in the particles will not lead to phase differences upon arrival at the point of detection. Using standard electromagnetic dipole radiation theory, or a standard Green's functions approach, we may derive for the radiative term $\boldsymbol{E}_{rad}$ of the scattered electric field strength (Fig. 17):

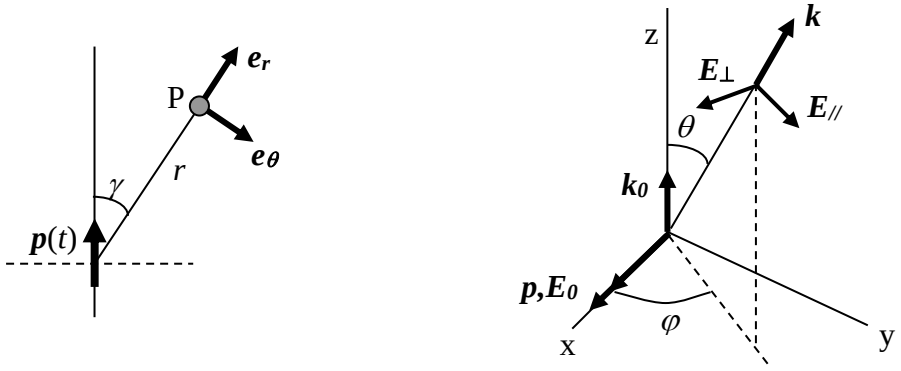

Fig. 17. a) Electric dipole, radiating towards detection point P at distance r and with polar scattering angle γ. The vectors $\boldsymbol{e}_r$ and $\boldsymbol{e}_\theta$ are unit vectors. Due to symmetry, the azimuthal angle does not play a role.
b) The scattering event, with conventional polar and azimuthal angles θ and φ. The incoming light propagates along the Z-axis. $\boldsymbol{E}_{//}$ and $\boldsymbol{E}_\perp$ are the field components parallel and perpendicular to the scattering plane, formed by $\boldsymbol{k}_0$ and $\boldsymbol{k}$.

$$\boldsymbol{E}_{rad} = -\frac{p_m k^2}{4\pi\varepsilon r}\sin\gamma.\exp(i\omega t').\boldsymbol{e}_\theta \quad ; \quad t' = t - \frac{r}{c}, \tag{4.6}$$

where p_m is the amplitude of the oscillating dipole $\boldsymbol{p}(t) = \boldsymbol{p}_m \exp(i\omega t)$, with ω as the frequency ($\omega = c / k$, with c the local light velocity). The parameter t' accounts for the time retardation upon arrival at detection, which generally could be the origin of phase differences. For clarity: Van de Hulst uses Gaussian rather than S.I.-units, which means that the factor $(4\pi\varepsilon_m)$ is set to unity.

Frequently $\boldsymbol{p}_m$ can be considered as being related to the incoming electric field $\boldsymbol{E}_0$, through the polarisability tensor $\overline{\overline{\alpha}}$ of the particle. In a number of cases this tensor reduces to a mere constant α, with

$$\alpha = 4\pi\varepsilon_m\alpha_H \quad ; \quad \alpha_H = a^3(\varepsilon_p - \varepsilon_m)\, f_p \quad ; \quad f_p = \frac{3\varepsilon_m}{\varepsilon_p + 2\varepsilon_m}. \tag{4.7}$$

where ε_p and ε_m are the dielectric constants of the particle and the medium, α_H is the polarisability as used by Van de Hulst (assuming $4\pi\varepsilon_m$ = unity) and f_p denotes the correction for the internal enhancement of the incoming field (see standard EM text books). Note the dependence on the particle volume, through a^3.
We find for the two electric field components:

$$\begin{aligned} |E_{//}| &= \frac{\alpha k^2}{4\pi\varepsilon_m r}\cos\theta.|E_{0,//}| = \frac{\alpha k^2}{4\pi\varepsilon_m r}\cos\theta.\cos\varphi.|E_0| = \frac{\alpha k^2}{4\pi\varepsilon_m r}\cos\theta.|E_{0,//}| \\ |E_\perp| &= \frac{\alpha k^2}{4\pi\varepsilon_m r}|E_{0,\perp}| = \frac{\alpha k^2}{4\pi\varepsilon_m r}\sin\varphi.|E_0| = \frac{\alpha k^2}{4\pi\varepsilon_m r}.|E_{0,\perp}| \end{aligned} \tag{4.8}$$

The intensities $I_{//}$ and $I_\perp$ are proportional to the squares of the field strengths ($I = \frac{1}{2}c\varepsilon_m E^2$), thus

$$I_{//} = \frac{\alpha^2 k^4}{(4\pi\varepsilon_m)^2 r^2} \cos^2\theta.\cos^2\varphi.\, I_0$$
$$I_{\perp} = \frac{\alpha^2 k^4}{(4\pi\varepsilon_m)^2 r^2} \sin^2\varphi.\, I_0 \qquad (4.9)$$

Due to the dependence on α^2 and k^4, the intensities are proportional to a^6 and $1/\lambda^4$.
The components of Van de Hulst's scattering matrix, eq. (3.46), will read

$$S_2(\theta) = \alpha k^3 \cos\theta \quad ; \quad S_1(\theta) = \alpha k^3 \quad ; \quad S_3 = S_4 = 0\ . \qquad (4.10)$$

This means that the component perpendicular to the scattering plane shows uniform scattering, but the parallel component has a cosine behaviour: when viewing the scattering particle along a direction parallel to the polarisation, no scattering will be observed.
For natural light the total intensity will be proportional to $\frac{1}{2}(S_1^2+S_2^2)$, and thus

$$I_{nat}(\theta) = \frac{\alpha^2 k^4 I_0}{(4\pi\varepsilon_m)^2 r^2} \frac{1+\cos^2\theta}{2}. \qquad (4.11)$$

Spatial integration of eq.(4.7) over θ and φ leads to the total scattered intensity I_{tot} (now expressed in W/sr instead of W/m^2):

$$I_{tot} = \frac{8\pi}{3} \frac{\alpha^2 k^4 I_0}{(4\pi\varepsilon_m)^2}. \qquad (4.12)$$

The scattering cross section σ_s is defined with (using Ω as the scattering solid angle and $F(\Omega)$ as the angle-dependent scattering function, but normalised to unity upon Ω-integration over 4π):

$$I(\Omega) = \sigma_s.F(\Omega).I_0, \qquad (4.13)$$

with $I(\Omega)$ expressed in W/sr and I_0 in W/m^2. This leads to

$$\sigma_s = \frac{8\pi}{3} \frac{\alpha^2 k^4}{(4\pi\varepsilon_m)^2} = \frac{8\pi}{3} \alpha_H{}^2 k^4 \qquad . \qquad (4.14)$$

The ratio Q_{sca} is given by

$$Q_{sca} = \frac{\sigma_s}{\sigma_g} = \frac{8}{3} a^4 (\varepsilon_p - \varepsilon_m)^2 \left(\frac{3\varepsilon_m}{\varepsilon_p + 2\varepsilon_m}\right)^2 k^4 \approx \frac{8}{3} x^4 \left(\frac{m^2-1}{m^2+2}\right)^2 \qquad (4.15)$$

where m^2 is the relative refractive index of the particles in the surrounding medium: $m^2 = \varepsilon_p/\varepsilon_m$.

4.2. Rayleigh-Gans

When particles grow larger, the phase differences of scattered waves arriving at the detection point from different source points in the scattering medium, cannot be neglected any more.
Here we will follow Van de Hulst, using the approximation $|\varepsilon_p-\varepsilon_m| << \varepsilon_m$. Also the value of $x|\varepsilon_p-\varepsilon_m|/\varepsilon_m$ should be << 1. With these assumptions we may write for a volume element dV:

$$d\alpha_H = \frac{m^2-1}{4\pi}dV \approx \frac{m-1}{2\pi}dV \tag{4.16}$$

with m is the relative refractive index of the particles in the medium: $m^2 = \varepsilon_p / \varepsilon_m$. The non-zero components of the scattering matrix will read:

$$S_2 = 4\pi\varepsilon_m \frac{m-1}{2\pi}V.R(\theta,\varphi) \quad ; \quad S_1 = 4\pi\varepsilon_m \frac{m-1}{2\pi}V.R(\theta,\varphi).\cos\theta\,, \tag{4.17}$$

with $R(\theta.\varphi)$ obtained by integration over the volume V using a phase-dependent factor $i\delta$:

$$R(\theta,\varphi) = \frac{1}{V}\iiint \exp(i\delta).dV\,. \tag{4.18}$$

The phase-difference δ is given by $\boldsymbol{k}\bullet(\boldsymbol{r}\text{-}\boldsymbol{r}_O)$, where $\boldsymbol{r}$ and $\boldsymbol{r}_O$ are the position vectors from the scattering volume element under consideration and the origin in the sample. The scattering cross section will be (for natural incoming light):

$$\sigma_s = \frac{1+\cos^2\theta}{2}k^4V^2\frac{(m-1)^2}{(2\pi)^2}\left|R(\theta,\varphi)\right|^2. \tag{4.19}$$

For special particles the function $R(\theta,\varphi)$ can be expressed analytically:

$$R(\theta,\varphi) = \sqrt{\frac{9\pi}{2u^3}}J_{3/2}(u) = \frac{3}{u^2}(\sin u - u\cos u) \quad \text{with} \quad u = 2x.\sin\tfrac{1}{2}\theta \tag{4.20}$$

The factor Q_{sca} for spherical particles is given by:

$$Q_{sca} = \frac{32}{27}(m-1)^2x^4 \quad (x<<1) \quad \text{and} \quad Q_{sca} = 2(m-1)^2x^2 \quad (x>>1) \tag{4.21}$$

For other shapes, see Van de Hulst.

4.3. Mie.

In principle, the rigorous scattering theory, as developed by Mie (see ref. in [15]), presents analytical expressions for all kind of particles. It departs from the Maxwell equations and solves the scalar part of the wave equation, taking boundary conditions into account. This leads to complicated expressions for the components of Van de Hulst's scattering matrix, which are only tractable when treated numerically. In the Montcarl-program we use a procedure developed by Zijp and Ten Bosch[23], which renders S_2 and S_1. Again, for natural light the total intensity will be proportional to $\frac{1}{2}(S_1^2+S_2^2)$. See Fig. 18 for an example.

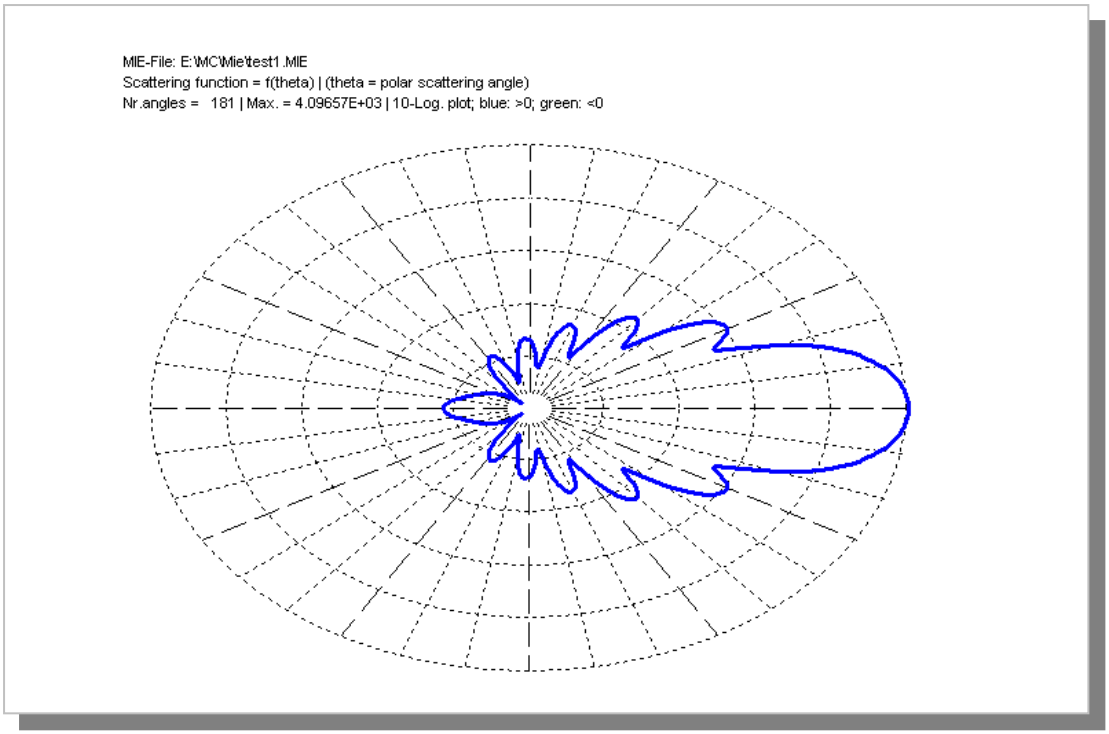

Fig. 18. Example of a MIE-file. Scattering function according to the Mie-formalism.

4.4. Henyey-Greenstein.

The Henyey-Greenstein scattering function[24] p_{HG} originates from the astronomical field, to calculate the scattering by cosmic particle clouds. Since it can be written in a closed analytical form, it can be used as a fast replacement for the Mie-functions. The function reads:

$$p_{HG}(\theta,\varphi) = \frac{1}{4\pi}\,\frac{1-g^2}{(1+g^2-2g.\cos\theta)^{3/2}}\,, \qquad (4.22)$$

where g is the averaged cosine of the polar angle θ of the scattering events This function is normalised to unity upon integration over 4π solid angle. See Fig 18a. for a (linear) plot of the function p as a function of the polar angle θ, with g as the parameter. For isotropic scattering $g = 0$ and for extreme forward scattering g approaches unity. Therefore g is called the *anisotropy factor*.

A drawback of this expression is that the function only describes the angle-dependent behaviour of the scattering. The calculation of the scattering cross section has to be done by other means. One option is to insert the total scattering cross section as obtained by Mie-scattering (or another approach, if applicable) as a separate factor in the Henyey-Greenstein expression.

4.5. Gegenbauer.

The Gegenbauer scattering function ("Gegenbauer kernel") uses two parameters: α, called the *shape factor*, and g, the *anisotropy factor*. The phase function is given by (using $\mu = \cos\theta$; the polar scattering angle) :

$$p_{GK}(\mu) = \frac{\alpha.g}{\pi} \frac{(1-g^2)^{2\alpha}}{[(1+g)^{2\alpha}-(1-g)^{2\alpha}][1+g^2-2g.\mu]^{1+\alpha}} \qquad (4.22a)$$

The factor α should be chosen as $\alpha > -1/2$. If $\alpha = 0$, $p_{GK} \rightarrow \infty$. If $\alpha = ½$, $p_{GK} = p_{HG}$. In Fig .18a the HG- and GK-functions are plotted for varying values of the parameters.

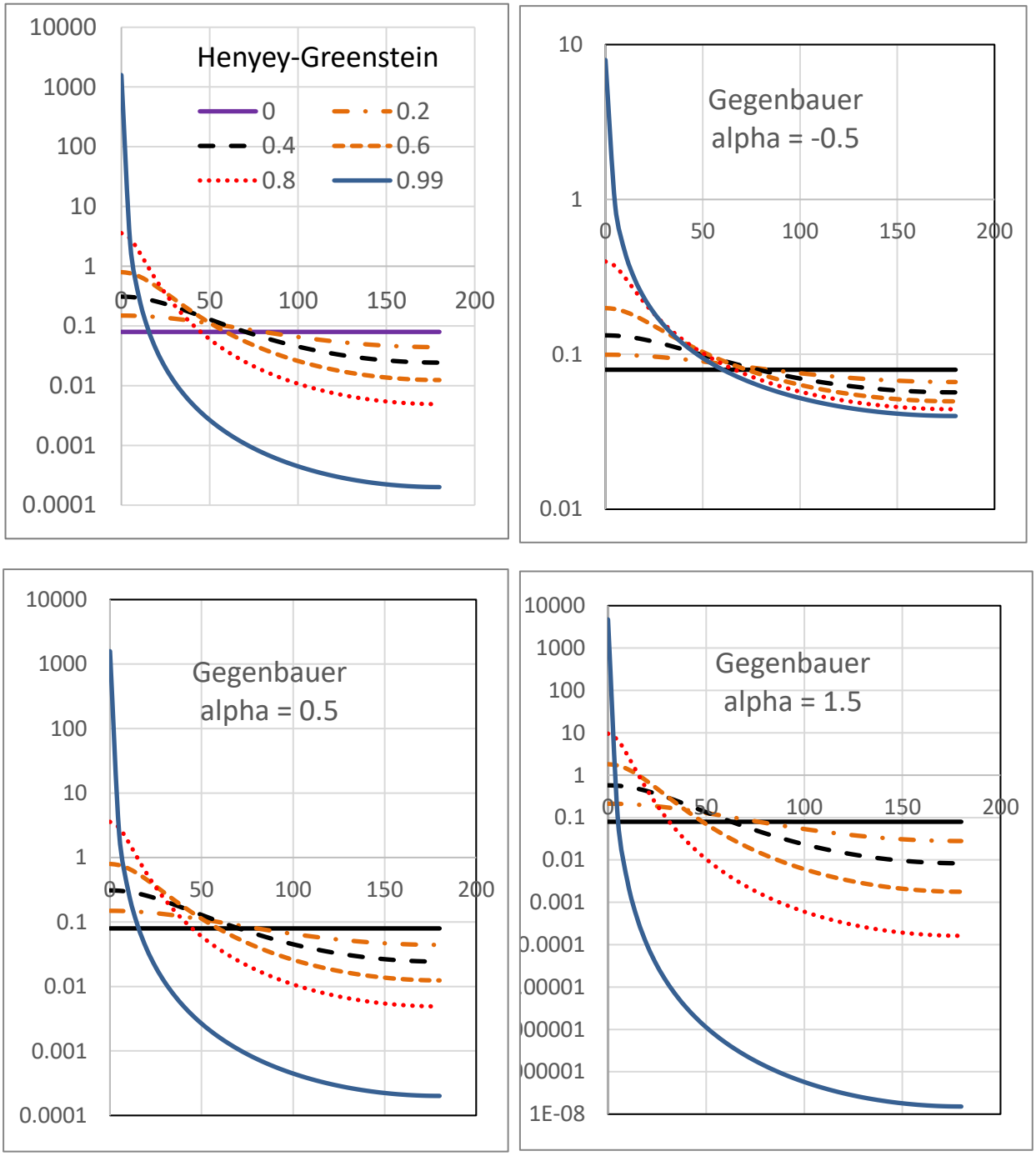

Fig 18a. Henyey-Greenstein and Gegenbauer phase functions p as a function of the polar angle θ, with g as the parameter. Note the logarithmic scales.

4.6. Isotropic.

Isotropic scattering can be described using the (normalised) function

$$p_{iso}(\theta,\varphi) = \frac{1}{4\pi}. \qquad (4.23)$$

The normalised cumulative function $C(\theta)$ will read

$$C(\theta) = \tfrac{1}{2}(1 - \cos\theta). \qquad (4.24)$$

and thus θ can be found from $\theta = \arccos(1 - 2R_N)$, with R_N as a fresh random number $(0<R_N<1)$. The value of g will be zero.

4.7. Peaked forward.

A peaked-forward scattering function is completely artificial. It can be useful for special applications. A possible functional form (not normalised) is

$$p_{PF} = \exp(-\theta^2/\theta_0^{\,2}). \qquad (4.25)$$

4.8. Fournier-Forand

Fournier and Forand derived[31,32] an approximate form for the phase function of scattering by water with particles, e.g. ocean water:

$$p_{FF}(\theta) = \frac{1}{4\pi(1-\delta)^2\delta^\nu}\left[\nu(1-\delta) - (1-\delta^\nu) + \{\delta(1-\delta^\nu\} - \nu(1-\delta)\}.\sin^{-2}\left(\frac{\theta}{2}\right)\right] + \frac{1-\delta_\pi^\nu}{16\pi(\delta_\pi-1)\delta_\pi^\nu}(3\cos^2\theta - 1)$$

with $\nu = \tfrac{1}{2}(3-\mu)$, $\delta = 4\sin^2\left(\frac{\theta}{2}\right) / [3(n-1)^2]$ and $\delta_\pi = \delta(\pi)$ at $\theta = \pi$ (4.26)

and n is the refractive index of the particles. They derived this expression using an anomalous diffraction approximation to Mie-scattering, with the particle density with size greater than r proportional to $r^{-\mu}$. Then $-\mu$ is the slope of the log-log-plot of the density versus r. μ must be larger than 3. Frequently used values for μ are around μ=4. This means that $\nu \approx -\tfrac{1}{2}$.

However, due to the $\sin^2$-function in the denominator, for $\theta \to 0$: $p_{FF} \to \infty$, which might hamper the calculation of the look-up table (cumulative inverse function). Therefore we adopt the approximation: $p_{FF}(0) = 10^{-10}$ rad. Its contribution to the look-up table (eq. (3.13)) will be = 0, due to the $\sin(\theta)$ weighting factor.

Therefore, it is advised to calculate the angular distribution with small angular spacings at low angles.

5. Light Sources.

For the injection of photons, one can imagine various mechanisms. Most general is the pencil beam, entering from the top. However, other beam profiles can be used as well. Here we offer a broad spectrum of those profiles.

5.1. Pencil beams.

Pencil beams are the simplest way to inject photons into the sample. The only programmatic requisite is to define the point of injection at the sample surface. With those beams, one still has to take care for a proper handling of the transport through the upper interface of the sample with the air, to take reflection losses into account.
Pencil beams can be tilted in two directions, which can be described using the tilting polar and azimuthal angles θ and φ. See section 5.2.

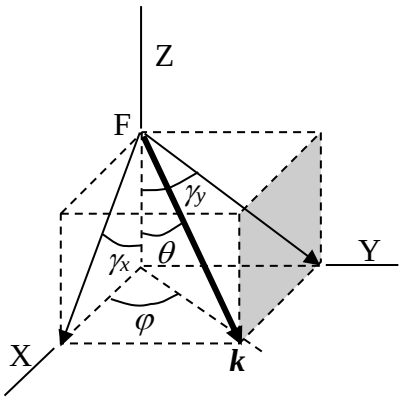

Fig. 19. Entrance of the beam. The surface of the sample is the XY-plane. F is the focus, and θ and φ are tilting angles of the symmetry axis of the beam.

5.2. Broad beams.

Broad beams come in two forms: divergent beams and parallel beams. For divergent beams we have adopted following procedure (see Fig. 19):

We define the divergence angles of the beam projection on the XZ- and YZ-planes respectively, as α_x and α_y, and the tilting angles of the symmetry axis of the beam with the Z-axis and the X-axis in the XY-plane, as θ and φ respectively. Then we may write (k is the length of $\boldsymbol{k}$):

$$k_x = k\ \sin\theta\ \cos\varphi; \quad k_y = k\ \sin\theta\ \sin\varphi; \quad k_z = k\ \cos\theta \tag{5.1}$$

and for the tilting angles:

$$\tan\gamma_x = \frac{k_x}{k_z} = \tan\theta.\cos\varphi \quad ; \quad \tan\gamma_y = \frac{k_y}{k_z} = \tan\theta.\sin\varphi\,. \tag{5.2}$$

With adaptation for divergence:

$$\gamma_x' = \gamma_x + \alpha_x = \arctan(\tan\theta . \cos\varphi) + \alpha_x \ ,$$
$$\gamma_y' = \gamma_y + \alpha_x = \arctan(\tan\theta . \sin\varphi) + \alpha_y \ . \qquad (5.3)$$

The new direction vector ***k'*** will be given by

$$k'_x = \tan\gamma_x' . k'_z \quad ; \quad k'_y = \tan\gamma_y' . k'_z \quad ; \quad |k'| = k \ . \qquad (5.4)$$

This approach offers the opportunity to define divergent beams with different opening angles in X- and Y-directions, and with different profiles (Gaussian or uniform).
For parallel beams an ideal thin positive lens with focal point in F (see Fig. 19) is thought to be positioned horizontally on the surface.

5.3. Ring-shaped beams.

Here we only apply ring-shaped beams with uniform filling, which means that the light intensity will be equal at all point in the ring. Then the amount of photons passing through a ring at distance *r* from the centre and with width *dr* will be proportional to *r.dr*. To define the actual distance of the photon we need to construct the cumulative function *C*(*r*):

$$C(r) = \int_{R_1}^{r} c.r'.dr' \ , \qquad (5.5)$$

where *c* is a proportionality constant and $R_1 \le r \le R_2$ (R_1 and R_2 being the inner and outer ring radii), and normalize $C(R_2)$ to unity. This results in the cumulative function *C*(*r*) :

$$C(r) = \frac{r^2 - R_1^{\,2}}{R_2^{\,2} - R_1^{\,2}} . \qquad (5.6)$$

By equalling this function to a fresh random number between 0 and 1, the value of *r* is set. Subsequently the φ-value is chosen randomly between 0 and 2π.

The ring-shaped beam can be combined with divergence and tilting as mentioned before.

5.4. Isotropic injection.

We can adopt several models for isotropic injection. The simplest model is:

$$I(\theta) = c \quad ; \quad c = \text{constant} \qquad (5.7)$$

Then we can construct the normalised cumulative function

$$C(\theta) = \frac{C'(\theta)}{C'(\pi)} = \tfrac{1}{2}(1 - \cos\theta) \quad \text{with} \quad C'(\theta) = \int_0^{\theta} I(\theta').\sin\theta'.d\theta' . \qquad (5.8)$$

and by equalling this function to a fresh random number R_N, the value of θ can be derived, as θ = arccos $(1\text{-}2R_N)$. Again, the value of φ is obtained from a random number between 0 and 2π.

Another model uses isotropic radiances. See Fig. 20.

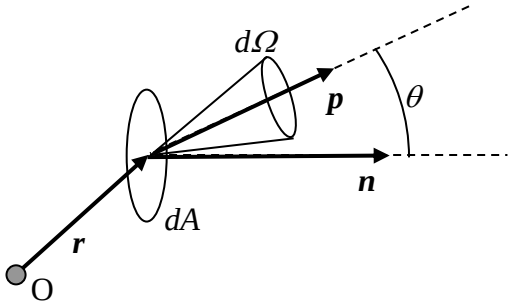

Fig. 20. Radiance and power are supposed to be emitted through area dA in direction ***p*** *in solid angle dΩ.*

Using the radiance $L(\boldsymbol{p},\boldsymbol{r})$, expressed in $W.m^{-2}sr^{-1}$, we find for the emitted power contribution and the flux vector $\boldsymbol{F}$:

$$dP = L(\boldsymbol{p},\boldsymbol{r}).\cos\theta.dA.d\Omega$$
$$\boldsymbol{F}(\boldsymbol{r}) = \int_{\Omega} \boldsymbol{p}.L(\boldsymbol{p},\boldsymbol{r}).d\Omega \qquad (5.9)$$

In the case of isotropic radiance, $L(\boldsymbol{p},\boldsymbol{r})$ will be a function of $\boldsymbol{r}$ only, and thus

$$\boldsymbol{F}(\boldsymbol{r}) = L(\boldsymbol{r}).\int_{\Omega} \boldsymbol{p}.d\Omega\,, \qquad (5.10)$$

and for the component along the normal vector (Z-component):

$$F_z(\boldsymbol{r}) = L(\boldsymbol{r})\int_{\Omega} \cos\theta.d\Omega = \pi.L(\boldsymbol{r}) \qquad (5.11)$$

The other components will render zero, because of a zero result of the φ-integration of the function sin φ and cos φ over 2π. And so, using a constant value L_0 for $L(\boldsymbol{r})$, we find for the normalised cumulative function:

$$C(\theta) = \frac{C'(\theta)}{C'(\pi)} = \sin^2\theta \quad \text{with} \quad C'(\theta) = \int_0^{\theta} L_0.\cos\theta'.\sin\theta'.d\theta' \,. \qquad (5.12)$$

By equalling a fresh random number (between 0 and 1) to $C(\theta)$, we find the corresponding value for θ (between 0 and π).

5.5. Internal point sources.

For internal point sources, we may follow the same lines as with pencil beams or broad, divergent beams, if wanted combined with a tilting angle. In this way, we are able to construct a layered sample with internal structures like spheres and cylinders, and to direct a beam either from the side or upwards, from the backside of the sample. It is also possible to combine this option with the option of internal detection, as will be described below.

5.6. Distributed sources.

Distributed sources will originate from points in a certain well-defined volume within the sample. These points will emit in random directions, and the light will not have a beam-like character. This type of photon source will be encountered, for instance when calculating Raman or fluorescence scattering from within a scattering and absorbing volume. In those cases the calculations will consist of two steps:

- Absorption of light with wavelength λ_1 at relevant positions inside the medium,
- Scattering to the surface of the sample, using photons originating from the absorption positions of the previous step, but now with wavelength λ_2 .

For fluorescence and Raman-Stokes emission λ_1 should be smaller than λ_2 . This means that in general the optical characteristics of the sample and its internal structure will be different in the two steps.

Due to the absorption step that precedes the fluorescence or Raman emission the direction of emission of the photon will be at random. Then the procedure of isotropic scattering can be used, see section 4.5. This means that the polar angle θ can be found from $\cos\theta = 1 - 2R_N$, where R_N is a fresh random number. Now $\cos\theta$ is identical to the Z-component of the direction unit vector, and from that the other components can be found, using a random number between 0 and 2π to find φ.

The polarisation direction will be randomised as well, which will randomise the components of the Stokes vector. The Stokes vector $\boldsymbol{S}^T_0$ **,** which starts the polarisation procedure in eq.(3.61), will now be defined on a local coordinate frame, with its Z-axis along the propagation vector of the photon and its X- and Y-axes perpendicular to that direction and to each other. Then the two components $E_{//}$ and $E_{\perp}$ might be chosen at random, as long as they satisfy $E_{//}^2 \cos^2\theta + E_{\perp}^2 \sin^2\theta = E_0^2$, where θ is the angle of the electric vector in the XY-plane with the X-axis.

6. Detection.

Normally the detection of emerging photons will take place at the surface, either at the top or at the bottom of the sample. We will denote these external detection options as "reflection" and "transmission" respectively.
Another way of detection is to make use of "internal" detectors. Here the photons are supposed to end their path at a certain position inside the sample.

A general property for both options is the presence of a limited Numerical Aperture (*NA*), with $NA = \sin\theta_D$, where θ_D is the (half) opening angle of the detection cone. *NA* ranges from 0 (pure pencil beam) to 1 (all incoming angles accepted). Its value can be set in the program.

The program stores the place of detection of the photon (*x*,*y*,*z*-coordinates) and the direction angles (θ and φ) with respect to the external laboratory coordinate frame. It also stores the number of scattering events and the percentage of Doppler scattering events. It also stores the resulting Doppler frequency and the path length, either geometrical or optical. The latter is corrected for wavelength changes due to changes in the refractive index, by multiplication of the local contribution to the path with the refractive index of the local medium.

6.1. External detection.

In the case of external detection, either reflection or transmission, the photon is assumed to be detected if

- It passed the detection plane in the proper direction. This implies that the photon indeed has crossed the final interface between the sample and the medium where the detector is. This is to be decided using the proper Fresnel relations (see above),
- It passed that plane within the borders of the "detection window". This window can be chosen rectangular, circular or ring-shaped.

Contrary to what is mentioned above, with external detection the program does not store the *z*-coordinate of detection, but the average depth of all scattering events along the path, or (as desired) the maximum depth along the path.

6.2. Internal detection.

With internal detection two options are present, one at the interface between two layers, and one at the internal interface of a structure (or "object"), like a sphere or cylinder.

- The first option is handled in the same way as with external detection, using "reflection" and "transmission" to denote the interface crossing direction necessary for detection.
- The second option is more complicated. This is elucidated in Fig. 21, where the situation is sketched for a sphere, as an example. A cylinder can be described analogously.

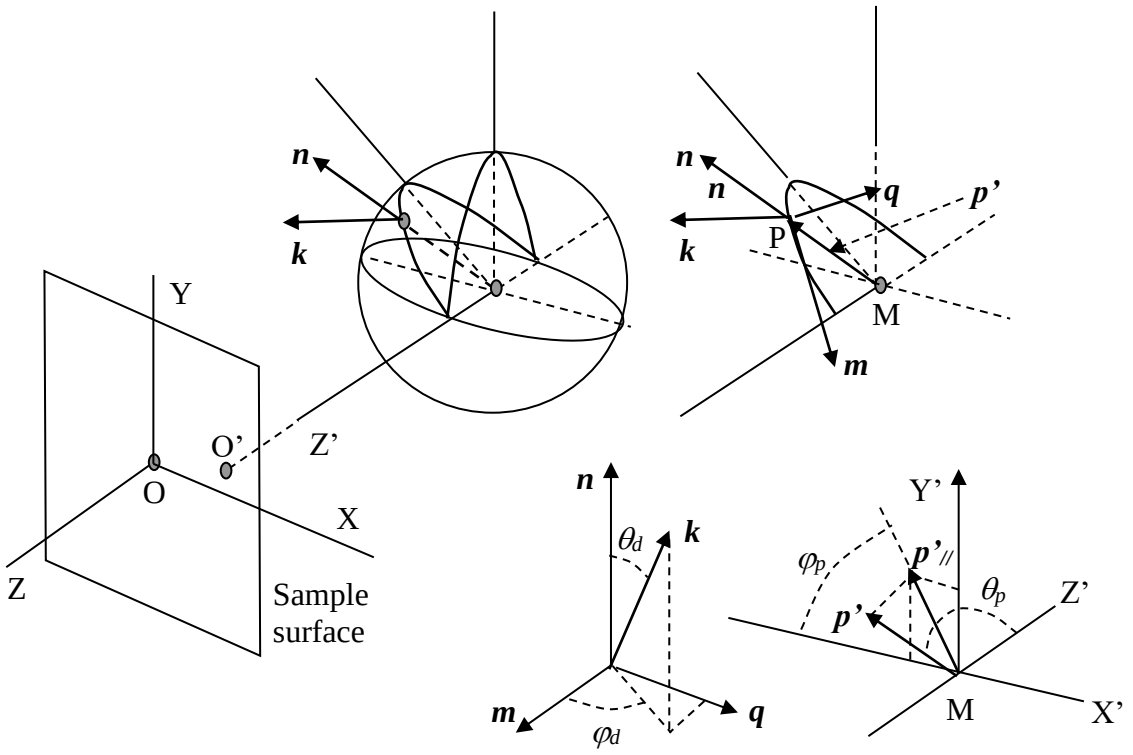

*Fig.21. Internal detection at the inside of a spherical surface. The vectors **p'**, **k** and **n** denote the position vector (relative to the origin of the sphere), the direction vector and the normal on the surface respectively. The vectors **n, m** and **q** represent the local coordinate frame at the detection point P, with **m** in the plane spanned by **n** and the Z'-axis, and **q** // **n** × **m**. All vectors except **p'** are here considered to be unit vectors. The subscripts p and d denote "position" and "direction" respectively.*

With the definitions as in Fig.21 the calculation of the position and direction angles proceeds as follows:

(1). $\boldsymbol{q} = \boldsymbol{n} \times \boldsymbol{e}_z$,
(2). $\boldsymbol{m} = \boldsymbol{q} \times \boldsymbol{n}$,
(3). $\theta_d = \arccos(\boldsymbol{n} \bullet \boldsymbol{k})$, (6.1)
(4). $\boldsymbol{k}_{//} = \boldsymbol{k} - \boldsymbol{n} . \cos\theta_d = \boldsymbol{k} - \boldsymbol{n}.(\boldsymbol{n} \bullet \boldsymbol{k})$,
(5). $\varphi_d = (1/|\boldsymbol{k}_{//}|).\ \arccos(\boldsymbol{m} \bullet \boldsymbol{k}_{//})$,
(6). $\boldsymbol{p'} = \boldsymbol{p} - \boldsymbol{r}_M = R\ .\ \boldsymbol{n}$,
(7). $\theta_p = \arccos(\boldsymbol{p'} \bullet \boldsymbol{e}_z)$,
(8). $\boldsymbol{p'}_{//} = \boldsymbol{p} - \boldsymbol{e}_z . \cos\theta_p$,
(9). $\varphi_p = (1/|\boldsymbol{p'}_{//}|).\ \arccos(\boldsymbol{p'}_{//} \bullet \boldsymbol{e}_x)$.

Expressing **k** from the (X',Y',Z')-frame into the (X,Y,Z)-frame is as follows (Fig.22):

$$\begin{aligned}
&\boldsymbol{k} = \sin\theta'.\cos\varphi'.\boldsymbol{e}_x' + \sin\theta'.\sin\varphi'.\boldsymbol{e}_y' + \cos\theta'.\boldsymbol{e}_z', \\
&\boldsymbol{e}_x' = \cos\theta_0.\cos\varphi_0.\boldsymbol{e}_x + \cos\theta_0.\sin\varphi_0.\boldsymbol{e}_y - \sin\theta_0.\boldsymbol{e}_z \qquad (6.2)\\
&\boldsymbol{e}_y' = -\sin\varphi_0.\boldsymbol{e}_x + \cos\varphi_0.\boldsymbol{e}_y \\
&\boldsymbol{e}_z' = \sin\theta_0.\cos\varphi_0.\boldsymbol{e}_x + \sin\theta_0.\sin\varphi_0.\boldsymbol{e}_y + \cos\theta_0.\boldsymbol{e}_z
\end{aligned}$$

The program offers the options to record internally detected photons in "reflection" mode (*i.e.* with direction angles $\theta > \pi/2$) or in "transmission" mode ($\theta < \pi/2$). It also allows calculating

the direction angles at the point of detection in both coordinate frames (laboratory frame and local frame). See Fig.23.

6.3. Sampling of photons.

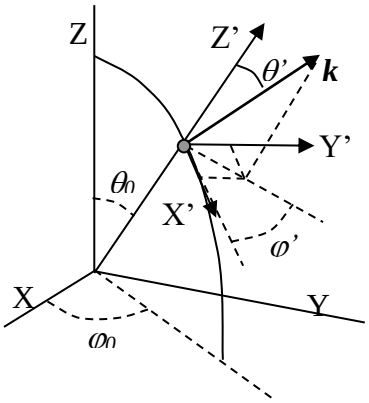

Fig.22. Expressing **k** *from the (X',Y',Z')-frame into the (X,Y,Z)-frame.*

For the sampling of photons some options for the maximum number of photons can be set:

- Emitted photons,
- Injected photons,
- Detected photons.

In all cases we consider photons to be detected only when arriving at the plane of detection within the detection window (rectangular, circular or ring-shaped). The difference between the options "emitted" and "injected" is due to the chance of reflection of the incoming beam at the surface of the sample and will be determined by the Fresnel relations.

Besides the recording of all properly detected photons, there exists also the option of recording the position of the photons during their paths, thus performing time-of-flight tracking. This can be done at a number of presettable time points, and the photons are stored in files similar to the files with detected photons.

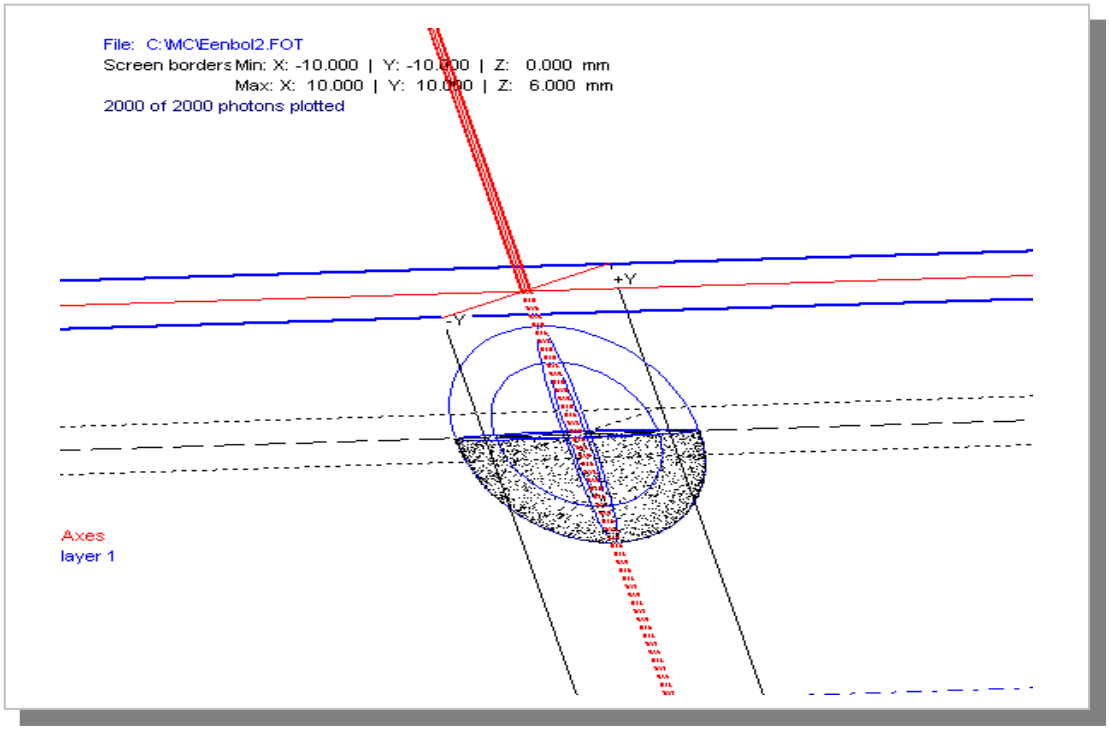

Fig. 23. Internal detection at the inside of a sphere. Settings: detection of photons arriving at the transmission side of the sphere only.

6.4. Photon path tracking

The tracking of the path of the photon, *i.e.* recording the coordinates of the scattering events and of the intersections with interfaces, can easily result in enormous files. Consider a typical case of scattering in tissue, with a scattering coefficient μ_s of about 10-20 mm^{-1} and a *g*-factor (average of the cosines of the polar scattering angles) of about 0.80 – 0.90. Then in each mm of the path about $1/\mu_s \approx 10$ scattering events will take place. However, due to the large *g*-factor the scattering will be predominantly in forward direction and it will only be after about $1/\mu_s' \approx 1$ mm that the direction of the photon can be considered as randomised. When detecting "reflected" photons, the path length of the photons will depend on the distance *d* between the point of injection of the light in the sample and the point of detection. For homogeneous samples the average depth in the middle of that distance is about ½*d*, and the average smoothed path length for perpendicular entrance and exit will be ½π*d*. However, the actual paths are very irregular and the actual path lengths can range from about that value to tens or hundreds times as large. This means that in most cases the number of scattering events will be very large. As an example, for a thick homogeneous medium with $\mu_s' = 1$ mm^{-1} and without absorption the average path length will be about 6*d*, which for $d = 2$ mm means about 120 scattering events, thus per photon at least 120 x 3 x 4 bytes = 1440 bytes. A typical simulation needs at least 10^4 photons, and thus in total 1440 Mbytes. Therefore, in those case it is better to register only part of the events, namely those at intervals of $1/\mu_s' = 1$ mm, which will decrease the storage space to 144 Mbytes per simulation.
Therefore, the program offers the options of recording the paths at intervals of $1/\mu_s$ or $1/\mu_s'$.

Photons originating from a pencil beam and emerging at equal distances *d* from the point of injection but at different positions on that ring are equivalent. However, visualisation of those tracks will end up in an un-untwinable bunch. Therefore, to clarify viewing we may rotate the whole paths around the axis

of the pencil beam to such an orientation as if the photons all emerged at the same position on the ring, *e.g.* the crossing point with the X-axis. This particular rotation is given by

$$\begin{pmatrix} x' \\ y' \\ z' \end{pmatrix} = \begin{pmatrix} \cos\varphi & \sin\varphi & 0 \\ -\sin\varphi & \cos\varphi & 0 \\ 0 & 0 & 1 \end{pmatrix} \begin{pmatrix} x \\ y \\ z \end{pmatrix} \tag{6.3}$$

See Fig. 24 for an example of the path tracking method.

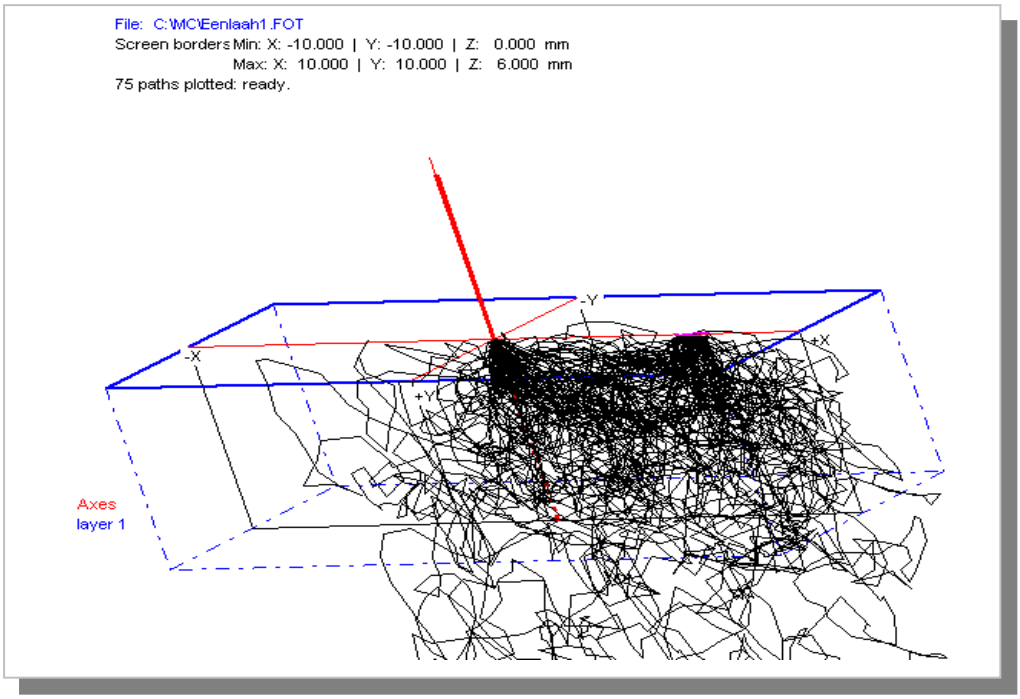

Fig. 24. Photon path tracking: Photon "bananas" arising by scattering from beam entrance point to exit area (between 5 and 6 mm). For clarity, all photon paths were rotated afterwards as if the photons had emerged on the +X-axis.

7. Special Features.

We now will describe some special features that are incorporated in the program. Laser-Doppler Flowmetry is the oldest feature, built in from the beginning of the development of the program, and meant to support measurements of Laser-Doppler Perfusion Flowmetry in tissue. Photoacoustics has been added to simulate the acoustic response to pulsed light. Frequency modulation is a modality adding extra information using path length-dependent phase delay information.

7.1. Laser-Doppler velocimetry

(1). Introduction
Laser-Doppler Flowmetry (LDF) makes use of the Doppler effect encountered with scattering of photons in particles when those particles are moving. In Fig. 25 the principles are shown. Using the definitions of the variables given in that figure, the Doppler frequency is given by

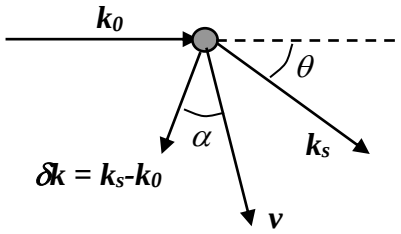

Fig. 25. Principles of Laser-Doppler Flowmetry. The particle has a velocity $\boldsymbol{v}$*. Vectors* $\boldsymbol{k_0}$ *and* $\boldsymbol{k_s}$ *denote the incoming and scattered light wave vectors, and* $\delta\boldsymbol{k}$ *is the difference vector.*

$$\omega_D = (\boldsymbol{k}_s - \boldsymbol{k}_0) \bullet \boldsymbol{v} \tag{7.1}$$

and with

$$|\delta\boldsymbol{k}| = 2k.\sin\tfrac{1}{2}\theta\,, \tag{7.2}$$

we find

$$f_D = \frac{kv}{\pi}\sin\tfrac{1}{2}\theta.\cos\alpha \quad . \tag{7.3}$$

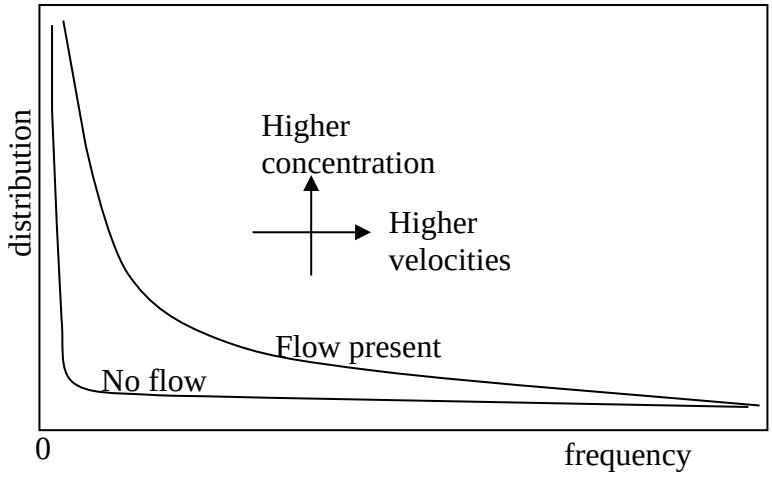

Fig. 26. A typical Doppler frequency spectrum as measured with LDF tissue perfusion (positive frequencies shown).

When applied to tissue, frequently the angles θ and α might be considered randomised. This is due to three reasons:

- Preceding scattering by non-moving particles might cause the direction of the photons to be randomised upon encountering moving particles;
- Most important moving particles are blood cells in capillaries. Due to the (more or less) random orientation of the capillaries the velocities will have random directions;
- Travelling from injection point to detection point, in general the photons will encounter many Doppler scattering effects, with random velocities and orientations.

All three effects will broaden the Doppler frequency distribution, which ideally would consist of one single peak, to a smooth distribution as in Fig. 26. This means that it is not possible to measure the local velocity, but we only may extract information about the averaged velocity over the measuring volume. The averaging concerns the three effects mentioned above.

There are two options to record these LDF-spectra: homodyne and heterodyne, depending on the relative amount of non-shifted light impinging on the detector. The first is the mutual electronic mixing of the Doppler-shifted signals, and the second is the mixing of those signals including mixing with non-shifted light, which can be overwhelmingly present. The resulting frequency and power spectra (which is the autocorrelation function of the frequency spectrum) will look as sketched in Fig.27.

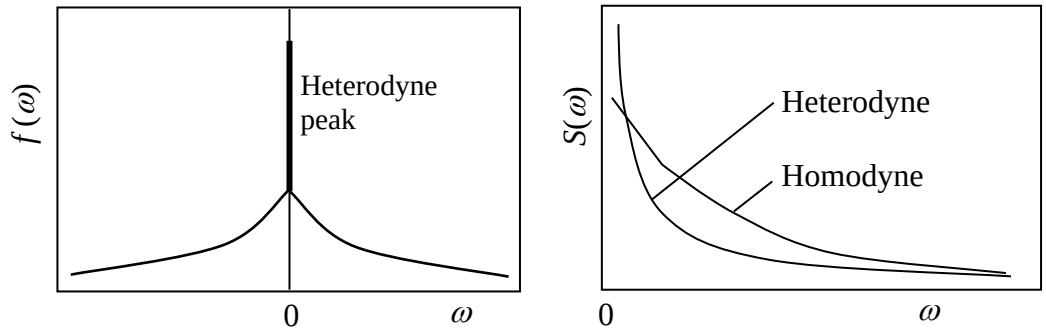

Fig.27. Homodyne and heterodyne frequency spectra $f(\omega)$ and power spectra $S(\omega)$. Normally the heterodyne peak is much higher than the signals at non-zero frequencies.

To characterize the frequency spectra use is made of moments of the power spectrum, defined as

$$M_n = \int_0^\infty \omega^n . S(\omega) . d\omega \,. \qquad (7.4a)$$

and the reduced moments

$$M_n' = \frac{M_n}{M_0} . \qquad (7.4b)$$

The zeroth moment is the area under the power spectrum itself, and can be considered as proportional to the concentration of moving particles in the measuring volume. Bonner and Nossal **[ref]** showed that the first moment M_1 is proportional to the averaged flow, while the ratio of the reduced moment $M_1' = M_1 / M_0$ will be proportional to the averaged velocity. Analogously, the reduced moment $M_2' = M_2 / M_0^{\,2}$ will be proportional to the average of the velocity-squared.
All three moments may be calculated within the package.

(2). Construction of the Doppler power spectrum.
For the construction[11] of the Doppler power spectrum from the frequency distribution all photons detected within the detection window will be sorted into a discrete frequency distribution $N(\omega_i)$. Suppose we recorded a_i photons in the i-th spectral interval (width $\Delta\omega = 2\pi\Delta f$). This number is proportional to $I(f_i).\Delta f$, where I is the intensity, which is proportional to $|E^2|$, E being the electric field amplitude.

$$E(t) = \sum_{j=0}^{N} \sqrt{a_j}\, \exp\left[i(j\Delta\omega.t + \phi_j)\right], \tag{7.5}$$

where N+1 is the number of intervals, and ϕ_j is the phase of the jth component. Since in the experiment we assume all photons to arrive at the same time, coherence between photons in the same frequency interval cannot be excluded. Therefore, ideally $\Delta\omega$ should be so small that the only values for a_j would be 0 and 1. However, to be able to work with tractable summations, a_j is to be read as the probability of the photon to arrive in that interval.
A square-law detector will at time $n.\Delta t$ measure a current I proportional to E^*E :

$$i(n\Delta t) = c\sum_{v=0}^{N}\sum_{w=0}^{N} \beta_{vw}\sqrt{a_v a_w}\, \exp\{\, i\left[(w-v)\Delta\omega.n\Delta t + \phi_w - \phi_v\right]\} \quad + \text{cc.}, \tag{7.6}$$

where c is a proportionality constant, cc stands for "complex conjugate" (to ensure that i is real) and β is a constant related to the degree of coherence of the signals in the frequency intervals (β=1 for perfect coherence, but β<1 when the detector area is larger than a single coherence area). Assuming that β is not frequency dependent, one can write

$$I(n\Delta t) = c\beta\sum_{v=0}^{N}\sum_{w=0}^{N} \sqrt{a_v a_w}\, \exp\{\, i\left[(w-v)\Delta\omega.n\Delta t + \phi_w - \phi_v\right]\} \quad + \text{cc.} \tag{7.7}$$

Now we rename $v = p$, and define $k = w - v$ and the factor f_{pk} as

$$f_{pk} = c\beta\sqrt{a_p a_{p+k}}\, \exp\left[i\left(\phi_{p+k} - \phi_p\right)\right] \tag{7.8}$$

and find

$$I(n\Delta t) = \sum_{p=0}^{N}\sum_{k=0}^{N-p} f_{pk}\, \exp(i\Delta\omega.n\Delta t) \quad + \text{cc.} \tag{7.9}$$

The Fourier transform $S(t)$ of the power spectrum $S(\omega)$, defined as

$$S(t) = < i^*(0).i(t) >, \tag{7.10}$$

can be written as

$$S(m\Delta t) = \frac{\Delta t}{N-m+1}\sum_{n=0}^{N-m} I(n\Delta t)\; I((n+m)\Delta t), \tag{7.11}$$

with $\Delta\omega = 2\pi/[(N+1).\Delta t]$. We construct the power spectrum $S(j\Delta\omega)$ using

$$S(j\Delta\omega) = \sum_{m=0}^{N} S(m\Delta t)\, \exp(-ij\Delta\omega.\Delta t), \tag{7.12}$$

and find

$$S(j\Delta\omega) = \sum_{m=0}^{N}\sum_{n=0}^{N-m}\sum_{p=0}^{N}\sum_{k=0}^{N-p}\sum_{p'=0}^{N}\sum_{k'=0}^{N-p} \frac{\Delta t}{N-m+1} \times \tag{7.13}$$

$$\left[\begin{array}{l} f_{pk}.f_{p'k'}.\exp\{i\Delta\omega\Delta t\left[kn + k'(n+m) - mj\right]\} + f_{pk}{}^*.f_{p'k'}{}^*.\exp\{-i\Delta\omega\Delta t\left[kn + k'(n+m) + mj\right]\} + \\ f_{pk}.f_{p'k'}{}^*.\exp\{i\Delta\omega\Delta t\left[kn - k'(n+m) - mj\right]\} + f_{pk}{}^*.f_{p'k'}.\exp\{-i\Delta\omega\Delta t\left[kn - k'(n+m) + mj\right]\} \end{array}\right]$$

Now, in the limit of $N \to \infty$, the phase factors will average out, except when their exponentials equal zero. Since the sum $n + m$ appears in each exponential, in order to have the exponential equal zero for each combination of n and m the variables n and m must not be present in the exponentials. This is possible in the last term only, under the condition that $k = k' = j$:

$$S(j\Delta\omega)=\sum_{m=0}^{N}\sum_{n=0}^{N-m}\sum_{p=0}^{N}\sum_{k=0}^{N-p}\sum_{p'=0}^{N}\sum_{k'=0}^{N-p'}\frac{\Delta t}{N-m+1}\; f_{pk}{}^{*}\cdot f_{p'k'}\;\delta(k-k')\,\delta(k-j) \qquad (7.14)$$

Since $0 \le k \le N$ - p , with $k = j$, it follows that $N - p \ge j$ or $p \le N - j$. Then

$$S(j\Delta\omega)=\sum_{m=0}^{N}\sum_{n=0}^{N-m}\sum_{p=0}^{N-j}\sum_{p'=0}^{N-j}\frac{\Delta t}{N-m+1}\; f_{pj}{}^{*}\cdot f_{p'j}=\sum_{p=0}^{N-j}\sum_{p'=0}^{N-j}2\pi\frac{f_{pj}{}^{*}\cdot f_{p'j}}{\Delta\omega}\,, \qquad (7.15)$$

and

$$S(j\Delta\omega)=2\pi\frac{c^2\beta^2}{\Delta\omega}\sum_{p=0}^{N-j}\sum_{p'=0}^{N-j}\sqrt{a_p a_{p'} a_{p+j} a_{p'+j}}\;\exp\left[i\left(\phi_p-\phi_{p'}+\phi_{p'+j}-\phi_{p+j}\right)\right]. \qquad (7.16)$$

Now, suppose that all photons arrive at the detector with equal phases. Then the exponential in eq.(7.16) becomes zero, and

$$S(j\Delta\omega)=2\pi\frac{c^2\beta^2}{\Delta\omega}\left[\sum_{p=0}^{N-j}\sqrt{a_p a_{p'}}\right]^2. \qquad (7.17)$$

However, in general the photons will have different phases due to their different path lengths. The measured power will be the expectation value of eq. (7.16) averaged over all phases. Thus for the term in eq. (7.16) with p and p', the expectation value will be zero unless $p = p'$. This leads to

$$S(j\Delta\omega)=2\pi\frac{c^2\beta^2}{\Delta\omega}\sum_{p=0}^{N-j}\sqrt{a_p a_{p+j} a_p a_{p+j}}=2\pi\frac{c^2\beta^2}{\Delta\omega}\sum_{p=0}^{N-j}a_p a_{p+j}\,. \qquad (7.18)$$

This is the general expression for the calculation of the power spectrum from the simulated frequency distribution.

In the case of heterodyne detection, where one of the spectral components (normally that at zero frequency, set $p = 0$ for that frequency) is much more intense than all others, eqns. (7.17) and (7.18) will lead to the same result:

$$S(j\Delta\omega)_{het}=2\pi\frac{c^2\beta^2}{\Delta\omega}a_0 a_j\,. \qquad (7.19)$$

(3). Implementation of velocity profiles.

For the velocity profiles of the scattering particles following options are available:

- Velocity direction along X-, Y- or Z-axis, or (in case of oblique objects) along the object axis.
- Velocity direction randomised for each scattering event, with all particles equal velocities. The direction is determined with a similar procedure as with isotropic injection of light (see section 5.4).
- Profiles can be uniform (equal velocity for all particles), or parabolic (in tubes and rectangular objects only), or they can have a Gaussian distribution.
  With the parabolic distribution the actual velocity is calculated according to

$$v=2v_0\left(1-\frac{r^2}{R^2}\right), \qquad (7.20)$$

  with v_0 as the average velocity value over the profile, r as the position of the particle with respect to the symmetry axis of the tube or object, or the mid plane of the layer when relevant, and R as the radius of the tube, or the distance between the adjacent interfaces .
  The Gaussian profile is handled using a cumulative function for the Gaussian profile. Here the standard deviation is expressed in a percentage of v_0 , being the maximum velocity in the profile. The actual value of the velocity is determined by equalling a fresh random number to that cumulative function.

7.2. Photoacoustics.

With photoacoustics (PA) short light pulses are injected in the sample. At positions where absorbing particles are present, part of the light will be absorbed. Due to the short duration of the pulse, the particle will heat up adiabatically. Normally this would result in volume dilatation, but since the surrounding medium is not heated, this dilatation will be prevented and a pressure shock wave will result. Some authors have investigated this mechanism. A review and some new theoretical aspects can be found in Hoelen's thesis and papers [25-28].
Typical values for the duration (FWHM) of the light pulses and the amount of energy to be injected are: 15 ns and 1 mJ/cm^2. With this values a safety factor of 20 from the European maxima for human tissue irradiation with this type of light pulses is maintained. Using a sound velocity of 1500 m/s this corresponds to a distance of 22.5 μm.
The PA-response of a spherical source on a short laser pulse is given by:

$$P(r,t) = C\frac{v^2}{r}\left(t-\frac{r}{v}\right)\exp\left\{-\left[\frac{v}{r_0}\left(t-\frac{r}{v}\right)\right]^2\right\}, \qquad (7.21)$$

with r as the distance from PA-source to the detector, r_0 as the source radius, t as the time after the pulse and v as the acoustic velocity. Since for the calculations in this program we only have to deal with relative values, we have incorporated variables describing the dilatation, the heat capacity and the heat conduction of the source, and the laser pulse energy in the constant C.
This function is a bipolar function, as in Fig.28.

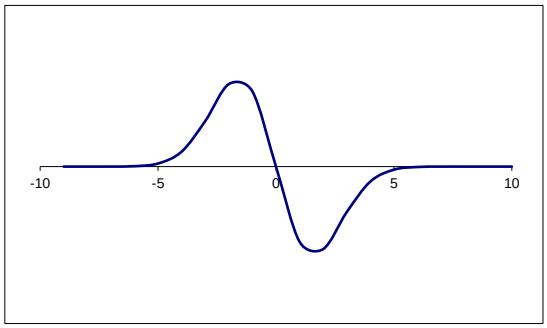

Fig. 28. Bipolar PA-pulse response: function P = x. exp ($-x^2/x_0$), *with –10 < x < 10 and* $x_0 = 5$.

We suppose that the sample can be subdivided into many 3D-voxels, which may serve as elementary PA-sources, provided light absorbing material is present. The voxels are supposed to be cubical, with sides *da*. It can be shown that the peak-peak time, *i.e.* the time τ_{pp} between the positive and negative peak of the bipolar pulse, is given by

$$\tau_{pp}^{\ 2} = (2\sigma)^2 = (2\sigma_l)^2 + (2\sigma_s)^2 = 2\tau_e^{\ 2} \qquad (7.22)$$

where σ_l is the standard deviation of the laser pulse, σ_s is that of the source voxel, σ is that of the bipolar pulse and τ_e is the effective pulse length.. The value of σ_l is given by *FWHM* / [2 √(2.ln2)], with *FWHM* as the full width at half maximum of the (Gaussian) laser pulse. For a cubical voxel, σ_s is given by $\sigma_s = da/(2\sqrt{2}.v)$, with $da/\sqrt{2}$ as the effective diameter of the heat source element.

The expression for the pressure given by eq.(7.21) has to be adapted for ultrasound attenuation during the time-of-flight to the detector. This will result in the corrected pressure pulse $P'(r,t)$:

$$P(r,t) = C\frac{v^2}{r}\left(t-\frac{r}{v}\right)\exp\left\{-\left(\frac{t-r/v}{\tau_e}\right)^2\right\}.\exp(-\mu_{US}.r)\,, \qquad (7.23)$$

where μ_{US} is the ultrasonic attenuation coefficient. This coefficient is slightly dependent on the ultrasound frequency. Here we take it as a constant, in view of the broad frequency bandwidth of the PA-pulse.

This function has been implemented in the program, with C =1. The pressure pulse is calculated as originating from the centre of the source voxel and arriving at the centres of the elements of the detector array. Therefore, the resulting pressure signal has to be multiplied with the area of the detector element, and normalised to the volume of the voxel. However, in reality with elements that are not "small" , due to phase differences upon arrival of the pressure pulse at different positions on a detector element, some destructive interference might be present, which will decrease the multiplication factor. We may correct for this effect in two ways:

- The detector elements are at first chosen very small (*i.e.* much smaller than the wavelength of the sound) and are afterwards grouped to larger detector elements, taking into account the phase differences between the centre points of the constituting elements in the group, for each voxel;
- The contribution from individual PA-sources to individual detector elements is corrected using the Directivity, or the Numerical Aperture function, of the detector element. Normally this is a Gaussian function, centred along the symmetry axis perpendicular to the element, with a certain opening angle given by the dimensions of the element and the characteristics of the laser pulse.

In the program both methods are implemented. For the Directivity a Gaussian, uniform or triangular function can be chosen. The groups are built from rectangles of single elements. See Fig.29.

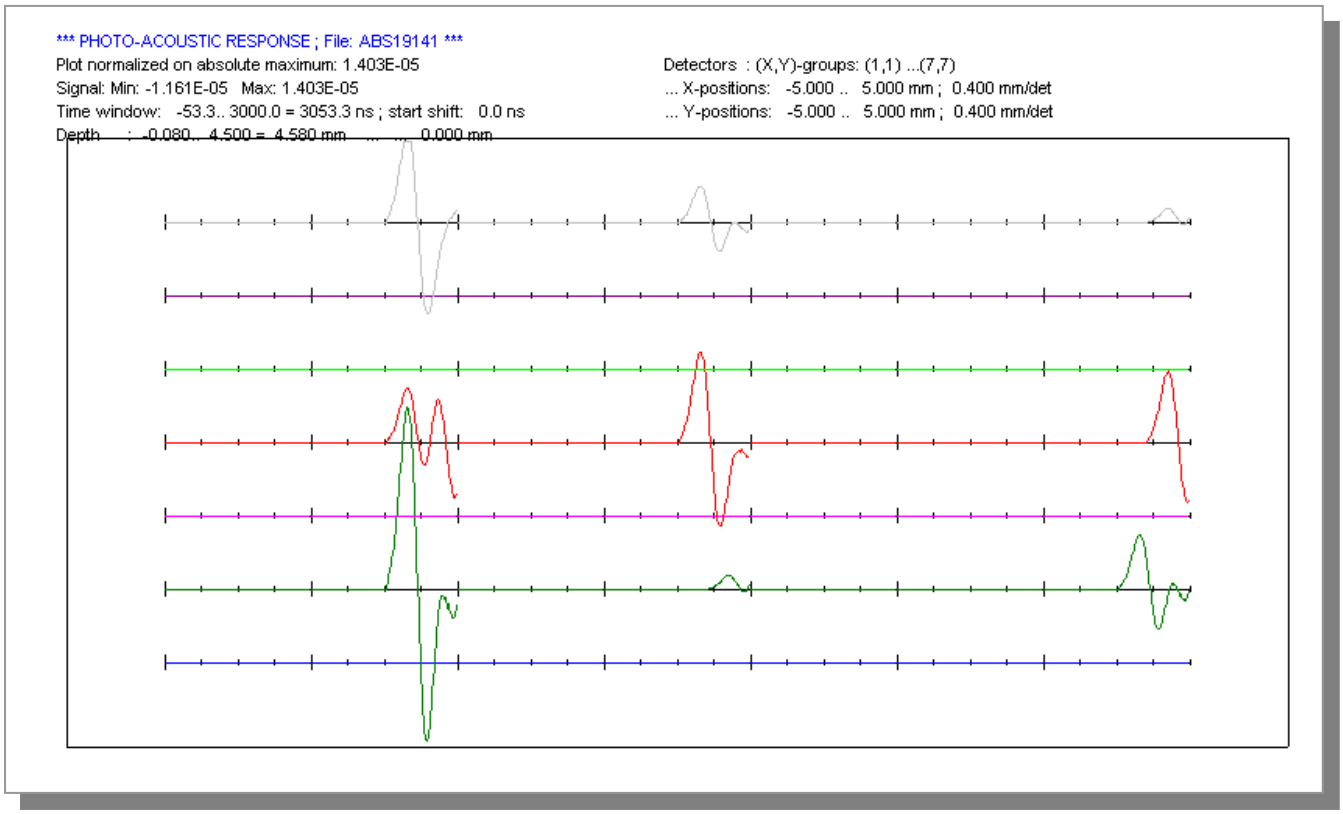

Fig. 29. Photoacoustic response at a 7 x 7 - detector array of a sample consisting of several absorbing objects in a scattering (but not absorbing) medium.

7.3. Time-of-flight Spectroscopy and Frequency Modulation.

A relatively new branch of the art of light scattering in tissue is time-of flight resolved scattering. The general idea is to distinguish between photons on the basis of their paths in tissue. This can be of help to elucidate the distribution of the optical properties, for instance when dealing with samples consisting of various layers.
There are two main methods:

- Time-of-flight spectroscopy, in which the photon paths are registered using time-resolved detection, *e.g.* with ps- or fs-lasers and an ultrafast camera like a streak camera, or by using ultrafast time-windowing using Kerr's cells. A typical time is 3 ps for 1 mm resolution (light velocity = $3x10^8$ m/s).
- Frequency Modulation spectroscopy, where the light source is modulated at very high frequencies, and the phase differences are recorded between photons arriving at the same detection point but after having travelling over different paths. The frequency range in use starts at 100 MHz and stops nowadays at about 1-2 GHz. For 100 MHz a path length difference of 1 mm will result in a phase difference of about 0.1 degree.

The first option of *Time-of-flight spectroscopy* has been taken care of in two ways:

- By implementing the possibility to register the positions of the photons at certain presettable time points during the scattering process;
- Using the option of analysing the registered time-of-flight distributions, that can be calculated form the simulated paths lengths (geometrical or optical) of the detected photons.

The second option of *Frequency Modulation spectroscopy* uses simple Fourier transformation of the path length distribution. For this purpose the path length distribution is translated into a time-of-flight distribution, using the local light velocities. The Fourier transform of this distribution will result in the frequency response. When denoting that Fourier transform with $F_j(\omega)$, we can deduce for the phase delay $\varphi_j(\omega)$ and the AC/DC modulation depth $m_j(\omega)$:

$$\varphi_j(\omega) = \arctan\frac{\mathrm{Im}\,F_j(\omega)}{\mathrm{Re}\,F_j(\omega)} \quad \text{and} \quad m_j(\omega) = \sqrt{\frac{\mathrm{Im}^2 F_j(\omega) + \mathrm{Re}^2 F_j(\omega)}{\mathrm{Re}^2 F_j(0)}} \qquad (7.24).$$

For the actual transform we may use the possibility of enlarging the number of points n in the time-of-flight distribution to an integer power of 2, named N, by filling the new points with zeros. Then Fast-Fourier transform algorithms will become possible. In doing this, the step size in the frequency spectrum will be smaller. When the time step in the time-of-flight distribution is given by Δt, then the maximum frequency is $f_{max} = 1 / (2\Delta t)$ and the frequency step is $\Delta f = f_{max} / (\frac{1}{2}N) = 1 / (N.\Delta t)$. This factor 2 is included due to the aliasing effect of this type of Fourier transform, by which the frequency spectrum ($f = 0..\ f_{max}$) is folded out and copied to $f = f_{max}\ ..2f_{max}$.
The program also offers facilities to calculate frequency modulation spectra using literature models, based on the diffusion approximation of the Radiative Transfer Equation, from Haskell *et al.* [8] for one-layer samples and Kienle *et al.* [9,10] for two-layer samples. Here we only list their results as far as implemented in the program.
We will use the notation (μ_a and μ_t are the absorption and total scattering coefficients: $\mu_t = \mu_a + \mu_s'$, and ω is the frequency):

$$k_R = \mathrm{Re}(k) = K(1) \quad ; \quad k_I = \mathrm{Im}(k) = K(-1),$$
$$K(p) = \sqrt{\tfrac{3}{2}\mu_a\mu_t}\sqrt{\sqrt{1+\omega^2 t^2} + p} \qquad (7.25a)$$

For small frequencies these functions can be approximated by

$$k_R = \sqrt{3\mu_a\mu_t}\left[1+\tfrac{1}{8}\omega^2\tau^2\right] \quad ; \quad k_I = \tfrac{1}{2}\sqrt{3\mu_a\mu_t}\,\omega\tau \quad ; \quad \tau = \frac{1}{\mu_a c/n} \tag{7.25b}$$

Haskell *et al.* calculated five models, (a) through (e), for the one-layer case, and Kienle *et al.* added a general model (f) for the two-layer case. These models are implemented in the program.

(a). Infinite medium.

$$\Delta\varphi = k_I r \quad ; \quad m = \exp\left[-\left(k_R - \sqrt{2}q\right)r\right] \tag{7.26a}$$

where r is the source-detector distance and $q = \sqrt{(3\mu_a\,\mu_t/2)}$.
Using eq.(7.25b) we may see that for small frequencies $\Delta\varphi$ will start linear with ω and m will start as a (slowly decreasing) constant. When ω increases, the slope of $\Delta\varphi$ will decrease gradually and the value of m will decrease as well.

(b). Semi-infinite medium, taking refractive index differences at the interface into account.

$$\Delta\varphi = k_I r - \arctan(I/R) \quad ; \quad m = (1/D).\sqrt{I^2+R^2} \tag{7.26b}$$

with D, I and R complicated functions of r, μ_a , μ_t and of the refractive indices and the refraction angles.

(c). Semi-infinite medium, without interface correction.

$$\Delta\varphi = k_I r - \arctan\frac{k_I}{k_R + 1/r_0} \quad ;$$
$$m = \frac{\sqrt{(k_R+1/r_0)^2 + k_I^{\,2}}}{\sqrt{2}q + 1/r_0}\exp\left[-\left(k_R - \sqrt{2}q\right)r_0\right] \tag{7.26c}$$

with $r_0^2 = r^2 + (1/\mu_t)^2$.

(d). Extrapolated boundary condition, where the interface has been shifted over a distance dependent of the refractive indices at the interface (see Haskell *et al.*[8] for this and following models).
(e). Partial Current and Extrapolated Boundary Unification.
(f).Two-layer model (Kienle *et al.*[9,10]).

8. Output Options.

The program offers several possibilities for output of the data. Apart from various ways to write photon data and corresponding statistics to file, we have several plot options. They will be described below. All plots can be exported in the form of *.BMP-files.

8.1. Parameter plots.

The fastest way of plotting data is using parameter plots of photon distributions, in which the number of photons is plotted as a function of one out of a set of variables. These variables are:

(a) X- , Y-, or R- position at detection or at plane-crossings (see below; R is the radius of the circle around central Z-axis),
(b) (R-position)^2 (as above),
(c) Path length or Time-of-flight distribution, followed by Phase and Modulation depth spectra using Frequency Modulation Spectroscopy,
(d) Polar angle θ or azimuthal angle φ of the photon direction at the detection point,
(e) Z-position: several options (the averaging <..> is performed over all detected photons):
- Depth (in absorption mode or with photons-in-flight at plane-crossing points),
- <Scattering depth> (in reflection or transmission mode),
- Maximum scatter depth,
- <Doppler scattering depth> (Doppler-scattering events only),

(f) Number of scatter events (or number of plane crossing),
(g) Number of Doppler scatter events,
(h) Doppler frequency,
(i) With Internal detection: Polar and azimuthal angles θ and φ,
(j) Paths: crossings with X=c planes
(k) Paths: crossings with Y=c planes
(l) Paths: crossings with Z=c planes
(m) Paths: crossings with R=c (cylindrical) planes.

Intensity plots
Normally we may choose for plotting of photon distributions, as a function of one of the variables. However, in case the variable is R or R^2 we have the option for plotting the intensity instead, thus dividing distribution function by $2\pi R.dR$, with dR as the interval width of the horizontal variable.
We also have the option for comparing simulated intensity plots with theoretical ones. Several models are available for that purpose. See section 8.4 (1) and Fig. 30.

Intensity plots can be on a ***linear*** scale, or ***logarithmic***, or in ***polar*** form.

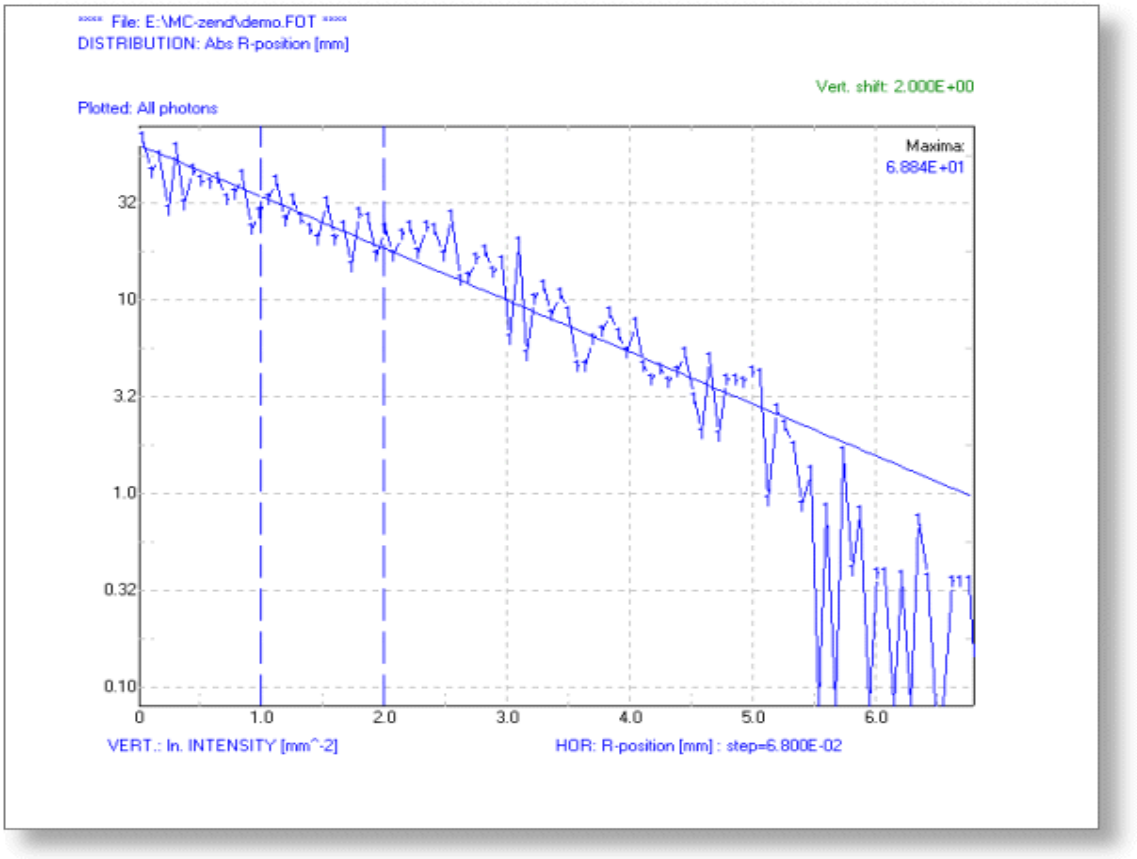

Fig.30. Example of output plots. Here ln (Intensity) vs. R-position from the Z-axis. Also included: a model approximation (solid line).

Parameters.

In addition to their role as horizontal variables in the distribution plots, all variables may also be used as parameters in the plots. For instance, suppose we divide the value region of a parameter into *n* intervals. This will result into *n* lines in the plot.

There are two layers of parameters, the first offers the option of shifting the lines horizontally over a certain value, the second vertically. We also may choose the option “Compare Files”, by which different files (simulations) can be compared directly, as the second parameter.

Plane-crossing intersections.

With the options “path tracking” the intersection points of the photon paths on their travel from source to detection point, with a set of planes perpendicular to the direction of the photons as seen at the surface, are recorded. The average coordinates of those intersections are calculated.

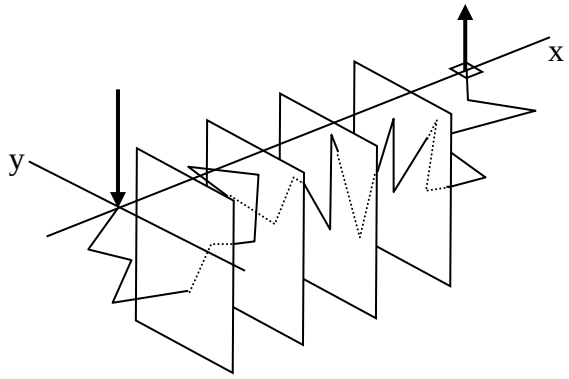

Fig 31. Example of recording of path tracking of the photons, in which the photons are meant to emerge through a small window at the X-axis. The arrows indicate the injection and detection points. For analysis, we define a set of planes perpendicular to the X-axis and record the Y- and Z-coordinates of the intersections. Since photons can take steps in all directions, they might cross some planes more than once.

For instance, when photons are tracked, for which the detection point lies at the surface on the X-axis, the crossing planes are defined parallel to the X-axis, ranging from the injection point to the detection point, and the Y- and Z-coordinates of those intersection points are recorded and (afterwards) averaged. This might be clarified with Fig. 31.
Results are presented in Fig. 32.

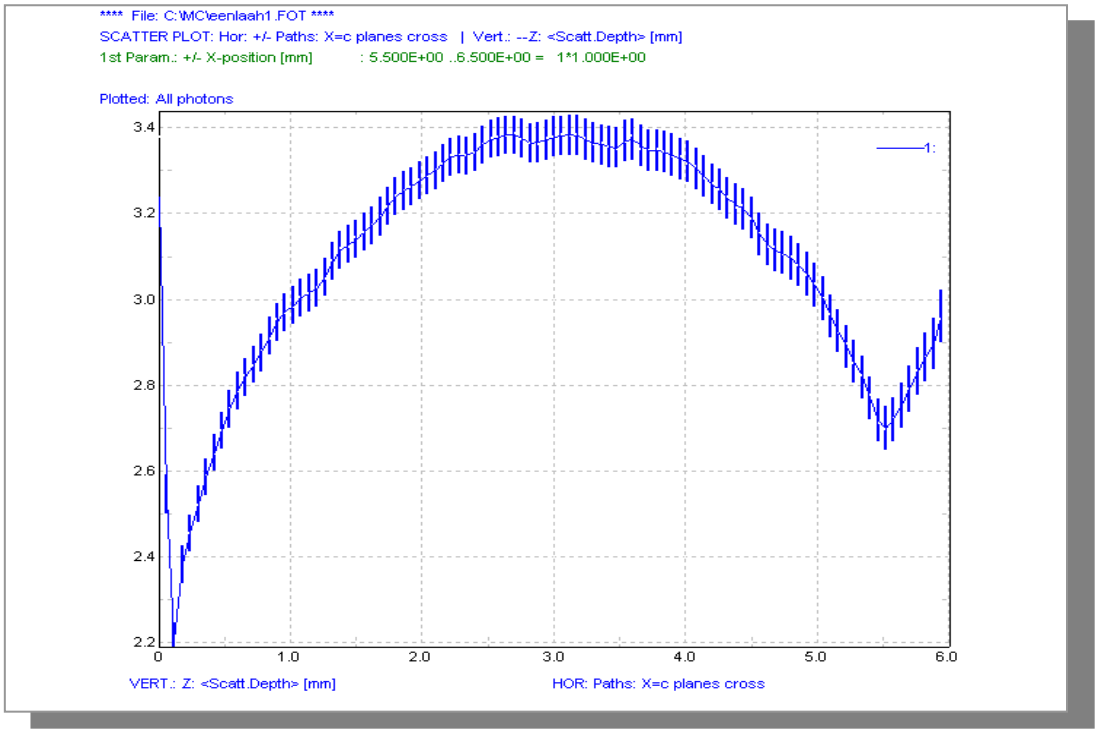

Fig. 32. Paths tracking: Averaged depths of photons, with standard deviation in the average. Settings: see fig. 5. Plot for distance > 5.5 mm is due to spurious photons.

In order to enhance the efficiency of the simulation process, photons emerging at positions with equal radii to the injection point, might be taken together by rotating the whole path until an orientation as if the photon were emerging at that radius on the X-axis. See section 6.4.
The options for crossing planes are: flat planes perpendicular to the X- and Y-axis, and cylindrical planes around the central Z-axis at the injection point.

All plots can be made on a linear or logarithmic scale, and in the form of lines or symbols or both. We may choose for the option of *n*-points quadratic smoothing.

Normalisation.
The plots may be normalised on their own maximum, or on the highest maximum of the set, or on the maximum of the first curve. We also may normalise on the number of detected, or injected or emitted, photons.

Doppler Frequency handling.
The distributions as a function of the Doppler frequency, the "frequency distribution" may be converted into "power spectra" using the formalism described in section 7.1 (2). From those spectra we may have the program calculate the moments of the power spectrum, as discussed in section 7.1 (1).

8.2. Scatter plots.

In addition to the distribution and intensity plots as described above, an option of producing "scatter plots" is present, in which the values of a second variable are on the vertical axis. The individual photons can be plotted as points, or their average values (per X-axis interval) as symbols or lines.

Again we have the opportunity to divide the set of points in subsets corresponding with different values of (two) parameters. The points belonging to different parameters are presented with different colours. We also may choose for horizontal or vertical shifting per parameter value. See fig.33.

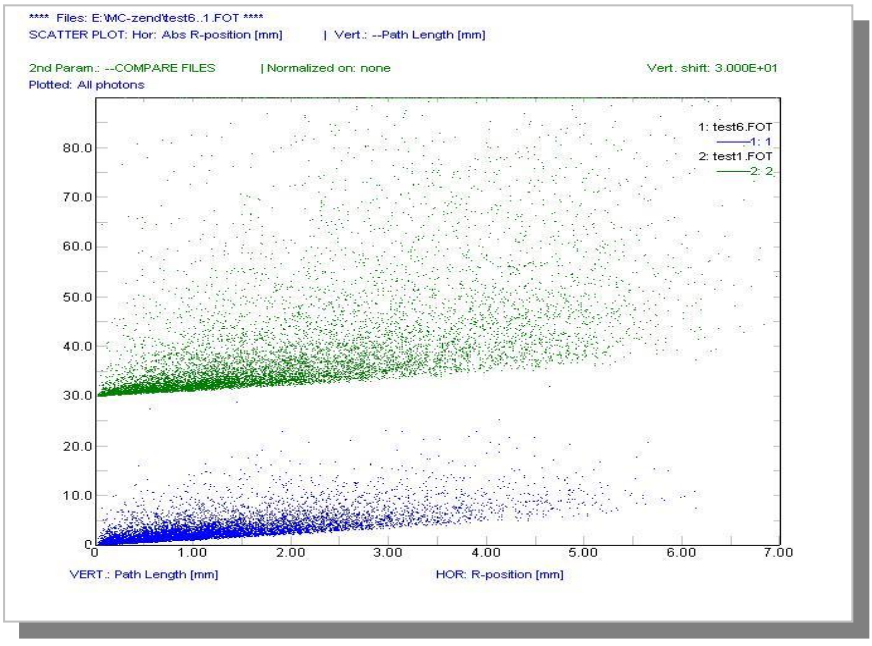

Fig. 33. Scatter plots of two samples, consisting of 1 layer with $\mu_s' = 1$ mm^{-1}; $\mu_a = 0$ (upper) and 0.1 (lower) mm^{-1} respectively. Plotted: Path length vs. detection position. In both cases 10000 photons recorded. Higher absorption results in a broader path length distribution.

8.3. 2D/3D-plots.

Another plot option is to produce 2D- or 3D-plots, based on the border values
See Figs.34 and 35.

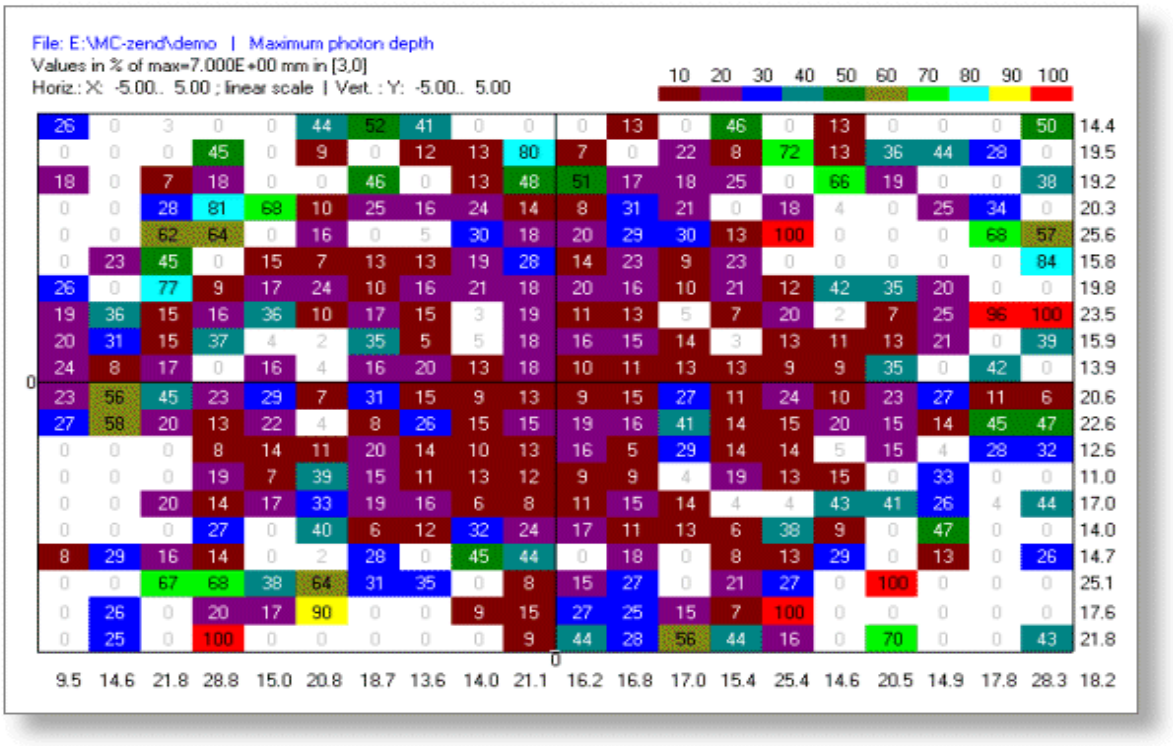

Fig.34. Example of 2D-plot: Here the maximum photon depth plotted as function of (x,y)-position.

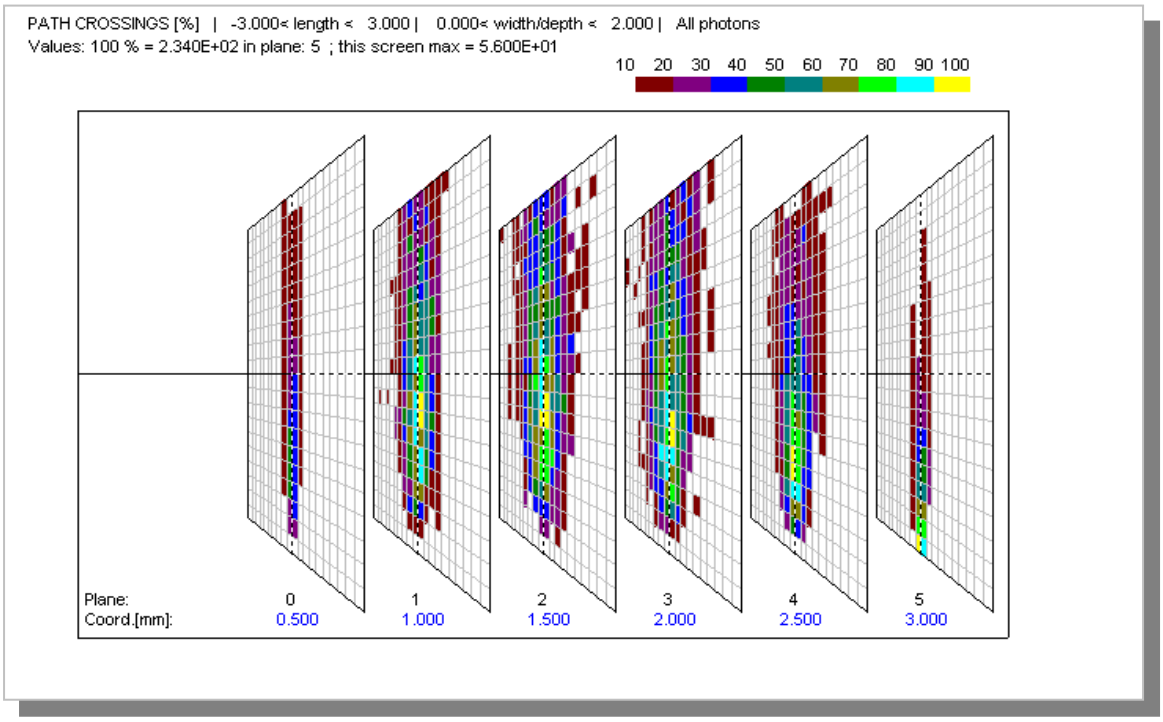

Fig.35. 3D-plot of Path tracking: photon "bananas": average depths of photon paths. Entrance at position 0; photons emerging between positions 5 and 6 mm from entrance. Normalisation per frame.

8.4. Approximations.

As a final step in the simulations one may want to compare the simulated results with theoretical curves. For this purpose we included several options in the program. The first option is to compare intensity data with published results of theoretical models based on the Diffusion Approximation. The second is to fit Doppler power spectra with exponential curves.

(1). <u>Intensity approximations</u>

In literature several approximate curves for the intensity as a function of the source-detector distance were investigated. Most important are those of Groenhuis and Ten Bosch [4], Bonner and Nossal [5], Patterson *et al* [6], and Farrell *et al.* [7]. Here we will deal with those models and give their results.

Ishimaru [2,3] notes for the light output as a function of the source-detector distance r :

$$I(r) = \frac{P\mu_{eff}^{\ 2}}{4\pi\mu_a r^n}\exp(-\mu_{eff}.r) \qquad (8.1)$$

where $I(r)$ is the energy fluence rate (in W/m^2) or the photon fluence rate (in m^{-2}s^{-1}), depending on the definition of P, being the injected power (in W) or the number of injected photons (in s^{-1}) , n is an exponential depending on the underlying physical model, and μ_{eff} is a characteristic "effective" attenuation coefficient, given by

$$\mu_{eff} = \sqrt{3\mu_a(\mu_a + \mu_s')}\,. \qquad (8.2)$$

There is some dispute about the value of the variable n. According to the Diffusion Approximation n should be unity. However, Groenhuis *et al.* [4] arrive at n = ½, on the basis of a simple scattering model consisting of a combination of an isotropic scattering term and a forward scattering term. Bonner *et al.* use a probabilistic lattice model and derive an expression with n = 2. Using an expression for the time-of-flight intensity for homogeneous slab samples, Patterson *et al.* published a model containing effective light sources at depths $z_0 + k.d$ (d = sample thickness; k= 1,2…) together with negatieve image sources at $-(z_0 + k.d)$ to ensure zero light flux at the surface:

$$I(r) = c\left[\sqrt{\frac{\pi}{a_+}}\exp(-2\sqrt{\mu_a a_+}) + \sqrt{\frac{\pi}{a_-}}\exp(-2\sqrt{\mu_a a_-})\right], \qquad (8.3a)$$

where

$$a_\pm = \frac{(z \pm z_0)^2 + r^2}{4D} \quad ; \quad D = \frac{\mu_a}{\mu_{eff}^{\ 2}}, \qquad (8.3b)$$

with D being a diffusion constant, and $z_0 = = 1/\mu_s'$.
However, when integrating this function over volume, two singularities arise, at $z = \pm z_0$. This problem was tackled by Rinzema and Graaff [29] who included non-scattered photons. This leads to a change:

$$I(r) = \frac{P}{4\pi Dr}\exp(-\mu_{eff}.r) \quad \rightarrow \quad \frac{P}{4\pi}\left[\frac{a'}{D_a r}\exp(-\kappa_0 r) + \frac{1}{r^2}\exp(-\mu_t r)\right], \qquad (8.4a)$$

and it is seen that, as in Bonner's model, a term with n =2 is present. In eq.(8.4) $\mu_t = \mu_s + \mu_a$, $a' = \mu_s/\mu_t$ (albedo) and $D_a = \mu_a/\kappa_0$, with κ_0 is the positive root of

$$a'.\arctan(\kappa_0/\mu_t) = \kappa_0/\mu_t\,. \qquad (8.4b)$$

The model of Patterson *et al.* was extended by Farrell *et al* [7] who starting from assuming an effective source at $z=z_0 = 1/(\mu_a + \mu_s')$ (with corresponding negative image source at $-z_0$), calculated the photon current leaving the tissue as the gradient of the fluence rate at the surface times *D*, and arrive at

$$I(r) = \frac{1}{4\pi} \sum_{k=1,2} z_{0k} \left(\mu_{eff} + \frac{1}{r_k} \right) \frac{\exp(-\mu_{eff} r_k)}{r_k^{\,2}} \qquad (8.5a)$$

with

$$r_1 = \left[(z - z_0)^2 + r^2 \right]^{1/2} \quad ; \quad r_2 = \left[(z + z_0 + 2z_b)^2 + r^2 \right]^{1/2}. \qquad (8.5b)$$

The depth correction z_b arises from taking refractive index mismatch at the surface interface into account [30,4]

$$z_b = 2AD \quad ; \quad A = \frac{1 + r_d}{1 - r_d} \qquad (8.5c)$$

and

$$r_d = -1.440\, n_{rel}^{-2} + 0.710\, n_{rel}^{-1} + 0.668 + 0.0636\, n_{rel}. \qquad (8.5d)$$

An example of the Farrell model is given in Fig.36, in which a Monte-Carlo simulation for a typical situation is compared.

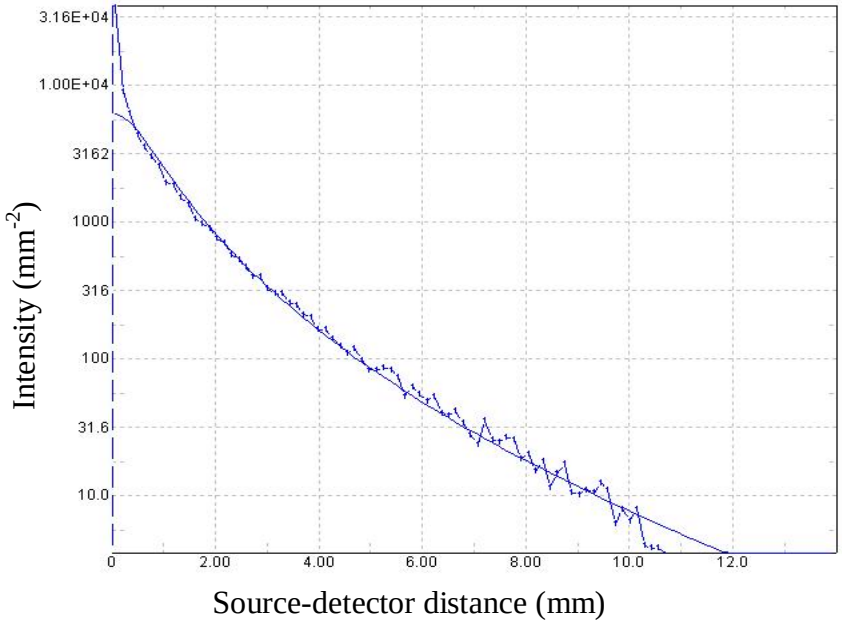

Fig.36. Comparison of the Farrell-model with simulations, for a one-layer semi-infinite sample with μ_s = 1 mm^{-1} and μ_a = 0.01 mm^{-1}. In simulations: Henyey-Greenstein scattering function, g = 0.90. Detected photons: 50000. Detection window radius: 0-12 mm. Ratio of reflected vs. injected photons: in the simulation: 0.748, in the model: 0.749.
At small r-values deviations occur due to the limited applicability of the Diffusion Approximation in that region.

This model is implemented in the program, together with the simple model given in eq. (8.1), for different values for *n*.
Farrell *et al.* also extended the model given above by assuming that the effective source extends along the Z-axis, obeing a Lambert-Beer-like attenuation law with $\mu_a + \mu_s'$ as the attenuation coefficient, but this results in expressions that are not very tractable.

Total reflection.

The approximations given above can be integrated over the surface., using

$$I_{total} = \int_0^{\infty} I(r).2\pi r.dr \tag{8.6}$$

and this will lead to

$$I_{total} = c\left(\pi / \mu_{eff}\right)^{3/2}; \quad = c\, 2\pi / \mu_{eff}; \quad = \infty \quad \text{for } b = \tfrac{1}{2}; 1; 2 \tag{8.7a}$$

and for the Farrell-model

$$I_{total} = \tfrac{1}{2} Pa' \exp(-\mu_{eff} z_0)\left[1 + \exp\left\{-\tfrac{4}{3} A\, \mu_{eff} z_0\right\}\right] \tag{8.7b}$$

with *a'* as the reduced albedo: $a' = \mu_s'/(\mu_a+\mu_s')$. It turns out that the correspondence of the Farrell model with simulated data, for values of the optical constants typical for tissue, is rather satisfactory. This is reflected in Fig. 37, where the ratios of reflected and injected photons in the simulation and in the model are compared.

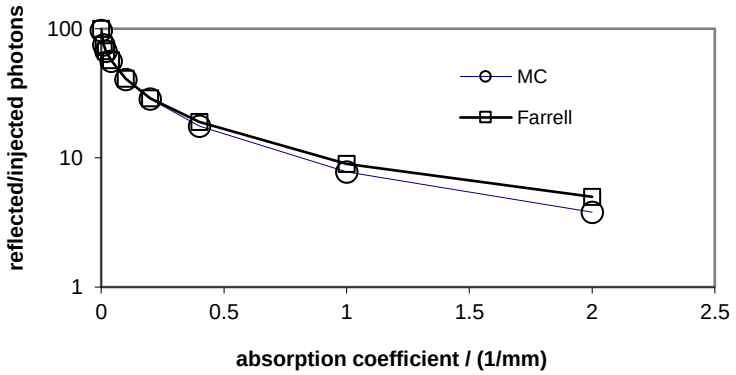

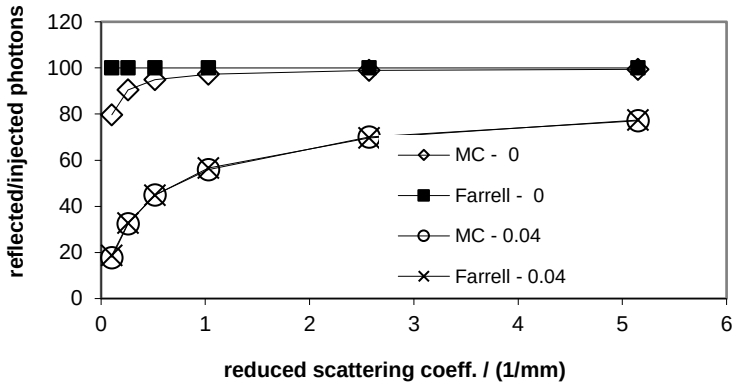

Fig. 37.Comparison of the ratio of reflected vs. injected photon numbers, calculated with the Farrell model and with Monte-Carlo simulations.
Upper panel: varying absorption coefficient μ_a ; μ_s= 10.4 mm^{-1}; g = 0.90; μ_s'=1.04 mm^{-1}.
Lower panel: varying reduced scattering coefficient μ_s' ; g = 0.90; parameter: μ_a [mm^{-1}]. Here the difference for zero absorption and low scattering may be caused by the limited thickness of the sample (65 mm).

(2). <u>Doppler power spectrum approximations.</u>

In section 7.1 the option of including particle velocities, leading to Doppler frequency spectra, was treated. In section 8.1 the possibility for calculating the moments of the Doppler power spectra was mentioned.
The program offers the option of fitting those spectra with pre-defined functions, since Bonner **[ref]** showed that sometimes these spectra might correspond to simple Lorentzian or Gaussian time functions.

For a Gaussian function, suppose the frequency distribution $f(\omega)$ looks like

$$f(\omega) = \exp(-\omega^2 / s^2) \tag{8.8a}$$

as is known with interval $\Delta\omega$, then the homodyne power spectrum (for $\omega \geq 0$ only!) will have the form

$$S(\omega) = \sqrt{\tfrac{1}{2}\pi}.s.\exp(-\omega^2/(2s^2)\,\Delta\omega \tag{8.8b}$$

and so the maximum (at ω=0) and the width of $S(\omega)$ will be $\sqrt{(\pi/2)}.s.\Delta\omega$ and $\sqrt{2}$ (= 1.414) times the maximum and the width of $f(\omega)$, respectively.
The moments are listed below, in Table 1.

For a Lorentzian function, suppose the frequency distribution $f(\omega)$ is given by

$$f(\omega) = \exp(-|\omega|/s) \tag{8.9a}$$

then

$$S(\omega) = (\omega + s)\exp(-\omega/s)\,\Delta\omega, \tag{8.9b}$$

and the maximum and the width of $S(\omega)$ will now be $s.\Delta\omega$ and 1.67835 s respectively, while those of $f(\omega)$ are: 1 and s.ln2 (=0.69315 s) respectively, a broadening with a factor of 2.4213.

Table 1. Moments of Lorentzian and Gaussian Power Spectra. (after integration over ω from 0 to ∞)

model	M_0	M_1	M_2	M_1/M_0	$\sqrt{(M_2/2M_0)}$
Gaussian	$\frac{1}{2}\, s\sqrt{\pi}$	$\frac{1}{2}\, s^2$	$\frac{1}{4}\, s^3\sqrt{\pi}$	$s / \sqrt{\pi}$	$\frac{1}{2}\, s$
Lorentzian	s	s^2	$2\, s^3$	s	s

9. Conclusions.

We have described the physics and mathematics behind the Monte-Carlo light scattering simulation program as developed in our group. It offers a large number of options and extra features. Among the options are: to include various structures, like tubes and spheres, in the layer system, to work with different concentrations of particles with different optical characteristics, to investigate reflection, transmission and absorption, to study path-length and time-of-flight distributions, to include frequency-modulation spectra and ultrafast transillumination phenomena, to handle Doppler frequency shifts upon scattering at moving particles, to calculate photoacoustic response from sources of absorbing particles, to perform Raman- and fluorescence spectroscopy. The light source might be a pencil beam, a broad parallel beam or a divergent beam, from an external or an internal focus, or photons produced at the positions were (in previous simulations) photons were absorbed.
The output options include: distribution plots of a number of variables, like the position of detection, the angles at detection, the number of scattering events, the path length (either optical or geometrical), the Doppler frequency shift. Detection might occur in reflection and transmission, *i.e.* at the surface or at the bottom of the sample, or internally, *e.g.* at the inner surface of an embedded sphere.
In addition to the simulations, a number of approximations is present, namely for the Doppler power spectra, the intensity curves and the frequency-modulation distributions of the phase and the modulation depth.

References.

1. K.M. Case and P.F. Zweifel, “Linear Transport Theory”, Publ. Addison-Wesley, Reading, Ma, USA, 1967.
2. A. Ishimaru, “Diffusion of Light in turbid material”, Appl. Optics, vol. 28, 1989, pp. 2210-2215.
3. A. Ishimaru, “Wave propagation and scattering in random media”, vol. 1 and 2, 1978, Academic Press, San Diego, USA.
4. R.A.J. Groenhuis, H.A. Ferwerda and J.J. ten Bosch, “Scattering and absorption of turbid materials determined from reflection measurements, 1: Theory”, Appl. Optics, vol. 22, 1983, pp. 2456-2462, “id. 2: Measuring method and calibration”, Appl. Optics, vol. 22, 1983, 2463-2467.
5. R.F. Bonner, R. Nossal, S. Havlin, G.H. Weiss, “Model for photon migration in turbid biological media”, J. Opt. Soc. Amer. A. 4, 1987, p 423-432.
6. M.S. Patterson, B. Chance and B.C. Wilson, “Time resolved reflectance and transmittance for the non-invasive measurement of tissue optical properties”, Appl. Optics, vol. 28, 1989, p. 2331-2336.
7. T.J. Farrell, M.S. Patterson, B.C. Wilson, “A diffusion theory model of spatially resolved, steady-state diffuse reflectance for the noninvasive determination of tissue optical properties in vivo”, Med. Phys, 19, 1992, p. 879-888.
8. R.C. Haskell, L.O. Svaasand, T.T. Tsay, T.C. Feng, M.S.McAdams, B.J. Tromberg, “Boundary conditions for the diffusion equation in radiative transfer”, J. Opt. Soc. Amer. A 11, 1994, p. 2727-2741.
9. A. Kienle, M.S. Patterson, N. Dögnitz, R. Bays, G. Wagnières, H. van den Bergh, “Noninvasive determination of the optical properties of two-layered media”, Appl. Optics, vol. 37, 1998, p. 779-791.
10. A. Kienle, T. Glanzmann, “In vivo determination of the optical properties of muscle with time-resolved reflecntance using a layered model”, Phys. Med. Biol., vol. 44, 1999, p. 2689-2702.
11. F.F.M. de Mul, M.H. Koelink, M.L. Kok, P.J. Harmsma, J. Greve, R. Graaff, J.G. Aarnoudse, "Laser Doppler Velocimetry and Monte Carlo Simulations on Models for Blood Perfusion in Tissue", Appl. Optics, vol. 34, 1995, p. 6595-6611.

12. For further information: see http://bmo.tn.utwente.nl/montecarlo or the general site of the University Twente, click to “Faculties” or “Departments”, then to “Applied Physics”, “Research”, “Biophysics”, “Biomedical Optics”, “courses”.
13. L. Wang and S.L. Jacques, “Hybrid model of Monte-Carlo simulation and diffusion theory for light reflectance by turbid media”, J.Opt.Soc.Amer. A10, 1993, p. 1746-1752.
14. V.G.Kolinko, F.F.M. de Mul, J. Greve, A.V. Priezzhev, “On refraction in Monte-Carlo simulations of light transport through biological tissues”, Med.Biol.Eng.Comp. 35, 1997, p. 287-288.
15. H.C. van de Hulst, “Light Scattering by Small Particles”, Dover Publications, New York, USA, 1957,1981, ISBN 0-486-64228-3.
16. G. Yao and L.V. Wang, “Propagation of polarized light in turbbid media: simulated animation sequences”, Optics Express, 7, 2000, p.198-203.
17. M.J. Rakovic and G.W. Kattawar, “Theoretical Analysis of polarization patterns from incoherent backscattering of light”, Appl.Optics, 37, 1998, p. 3333-3338.
18. M.J. Rakovic, G.W. Kattawar, M. Mehrubeoglu, B.D. Cameron, L.V. Wang, S. Rastegar, G.L. Coté, “Light backscattering polarization patterns from turbid media: theory and experiment”, Appl.Optics, 38, 1999, p.3399-3408.
19. W.S. Bickel and W.M. Bailey, “Stokes vectors, Mueller matrices and polarized light”, Am.J. Phys. 53, 1985, p. 468-478.
20. S. Bartel and A.H. Hielscher, “Monte-Carlo simulations of diffuse backscattering Mueller matrix for highly scattering media”, Appl.Optics, 39, 2000, p.1580-1588.
21. X.Wang, G. Yao, L.V.Wang, “Monte Carlo model and single-scattering approximation of the propagation of polarized light in turbid media containing glucose”, Appl.Optics, 41, 2002, p. 792-801.
22. M. Born and E. Wolf, “Principles of Optics”, Cambridge University Press, 6th ed. 1980-1993, ISBN 0-521-63921-2.
23. J.R. Zijp and J.J. ten Bosch, “Pascal program to perform Mie calculations”, Opt. Engin. 32, 1993, p. 1691-1695.
24. L.G. Henyey and J.L. Greenstein, “Diffuse radiation in the galaxy”, Astrophys. J., vol. 93, 1941, p.70-83.
25. C.G.A. Hoelen, F.F.M. de Mul, R. Pongers, A. Dekker, “Three-dimensional photoacoustic imaging of blood vessels in tissue”, Opt.Lett. 23, 1998, p. 648-650.
26. C.G.A. Hoelen, F.F.M. de Mul, “A new theoretical approach to photoacoustic signal generation”, J.Acoust.Soc.Am. 106, 1999, p. 695-706.
27. C.G.A. Hoelen, A. Dekker, F.F.M. de Mul, “Detection of photoacoustic transients originating from microstructures in optically diffuse media such as biological tissue”, IEEE – UFFC, 48, 2001, p.37-47.
28. C.G.A. Hoelen, F.F.M. de Mul, “Image Reconstruction for Photoacoustic Scanning of Tissue Structures”, Appl. Optics, 39, 2000, p.5872-5883.
29. R. Graaff and K. Rinzema, “Practical improvements on photon diffusion theory: application to isotropic scattering”, Phys. Med. Biol., vol 46, 2001, p. 3043-3050.
30. M. Keijser, W.M. Star, P.R.Storchi, “Optical diffusion in layered media”, Appl.Optics 27, 1988, p.1820-1824.
31. Fournier, G. and J.L. Forand, 1994. Analytic phase function for ocean water. In Ocean Optics XII SPIE Vol. 2258, J. S. Jaffe [ed], 194-201.
32. Fournier, G. and M. Jonasz, 1999. Computer based underwater imaging analysis. In Airborne and In-water Underwater Imaging, SPIE Vol. 3761, G. Gilbert [ed], 62-77 (with corrections).